Modeling of offshore wind turbines with braced support structures

Von der Fakultät für Bauingenieurwesen und Geodäsie
der Gottfried Wilhelm Leibniz Universität Hannover
zur Erlangung des Grades

DOKTOR DER INGENIEURWISSENSCHAFTEN
– DR.-ING. –

genehmigte Dissertation

von Dipl.-Ing. Fabian Richard Vorpahl
geboren am 08.11.1979 in Heidelberg

2015

Eigenständigkeitserklärung

Hiermit erkläre ich folgendes:

- Die Regeln der geltenden Promotionsordnung sind mir bekannt und wurden eingehalten. Mit einer Prüfung nach den Bestimmungen der Promotionsordnung bin ich einverstanden.

- Die Dissertation habe ich selbst verfasst (Selbständigkeitserklärung), ich habe keine Textabschnitte von Dritten oder eigener Prüfungsarbeiten ohne Kennzeichnung übernommen und alle benutzten Hilfsmittel und Quellen in meiner Arbeit angegeben.

- Dritten habe ich weder unmittelbar noch mittelbar geldwerte Leistungen für Vermittlungstätigkeiten oder für die inhaltliche Ausarbeitung der Dissertation erbracht. Das heißt; die wissenschaftliche Arbeit ist weder in Teilen noch in Gänze von Dritten gegen Entgelt oder sonstige Gegenleistung erworben oder vermittelt worden.

- Die Dissertation habe ich noch nicht als Prüfungsarbeit für eine staatliche oder andere wissenschaftliche Prüfung eingereicht.

- Ich habe keine gleiche oder eine in wesentlichen Teilen ähnliche Arbeit bei einer anderen Hochschule als Dissertation eingereicht. Weiterhin habe ich keine andere Abhandlung als Dissertation eingereicht.

- Ich bin damit einverstanden, dass die Dissertation zum Zwecke der überprüfung der Einhaltung allgemein geltender wissenschaftlicher Standards genutzt wird. Dies gilt insbesondere auch unter Verwendung elektronischer Datenverarbeitungsprogramme.

Bremerhaven, den 15.01.2014,

Fabian Vorpahl

Executive Summary

Offshore Wind Energy is one of the key technologies in the transition towards a low-carbon economy with an affordable cost of energy. In the last decade, offshore wind turbines (OWTs) grew in size and moved to deeper waters while a wider variety of support structures was developed and realized. Despite the current trend toward larger monopiles, it is expected, that a significant share of the future OWTs, in the respective water depth and turbine size class, will be mounted on multi-member support structures such as jackets. These structures must be cost efficient and reliable.

The design of the structures is based on load effects from simulations with aeroelastic tools. One possibility to unlock cost reduction potentials – while keeping the level of reliability – therefore is to increase the accuracy of these simulations. This, in turn leads to more realistic load effects and to a better understanding of the system's behavior and finally allows for reduced conservatism in the structural design.

The largest inaccuracies in structural simulation of multi-member support structures in aeroelastic tools are due to the simplified modeling of the joints. In this work, joint modeling and simulation is enhanced using a superelement feature in the aeroelastic tool Aeroelastic and Dynamic Computation of Systems (ADCoS)-Offhore. A tripod and a jacket support structure are investigated by means of results comparison for beam models (basic), superelement models (new development) and shell models (reference, used if possible).

Modeling of the jacket and the tripod support structure reveal, that higher order global modes of the support structures – that are usually calculated with aeroelastic tools in which the structures are modeled as beams – should be treated with caution for relatively low frequencies already, because modes occur in more accurate models, that cannot be represented with beams.

After verification of ADCoS-Offhore and the superelement feature in particular, it is found that the modeling of structural mass generally is possible with all types of models used here. Eigenfrequencies in contrast, are lower for the higher fidelity models and for some of the frequencies, large differences are found for both structures, tripod and jacket. The globally more compliant higher fidelity models lead to larger deflections.

The load path through the structures is highly dependent on joint stiffnesses and is therefore not well modeled with the simple beam models. The differences in the results are larger for the tripod than for the jacket, but for the jacket, the values are significant as well. General tendencies toward larger or smaller load effects for one or the other type of model cannot be determined. This is shown in results from static load cases, in terms of member load effects, and in fatigue load case results, mainly in terms of damage equivalent loads (DELs). If eigenfrequency results alone were compared, as it is commonly done early in the design process, large differences in load effects would not be predicted.

Based on the results of this work, the use of superelements for the joint modeling of multi-member support structures in aeroelastic simulation – or at least the use of an-

other approach that includes local joint flexibility (LJF) even if it's not as straightforward, elegant or physically accurate – is recommended.

Keywords: Offshore wind turbine, branched support structures, modeling.

Zusammenfassung

Offshore-Windenergie ist eine der Schlüsseltechnologien auf dem Weg in eine kohlenstoffarme Zukunft mit bezahlbarer Energieversorgung. Im vergangenen Jahrzehnt wuchs die durchschnittliche Größe der Offshore-Windenergieanlagen und zunehmend wurden Standorte mit größeren Wassertiefen erschlossen. In diesem Kontext wurden neue Tragstrukturtypen entwickelt. Trotz des derzeitigen Trends zu immer größeren Monopile-Strukturen ist davon auszugehen, dass ein relevanter Anteil der Anlagen – im entsprechenden Größen- und Wassertiefenbereich – auf verzweigten Strukturen wie Jackets errichtet werden wird. Diese Strukturen müssen dabei sowohl kosteneffizient als auch betriebssicher sein.

Die Auslegung dieser Strukturen erfolgt auf Basis von Schnittgrößen, die mit Hilfe gekoppelter Simulationswerkzeuge (*aeroelastic tools*) berechnet werden. Eine weitere Optimierung und damit eine Kostenreduktion kann durch eine Erhöhung der Simulationsgenauigkeit ermöglicht werden, wobei das Zuverlässigkeitsniveau erhalten bleibt. Die Erhöhung der Simulationsgenauigkeit führt zu einem besseren Systemverständnis und zu realistischeren Lasten, was schlussendlich weniger konservative Entwürfe ermöglicht.

Der größte Fehler bezüglich der Abbildung der Struktur in der gekoppelten Simulation resultiert aus der vereinfachten Modellierung der Rohrknoten verzweigter Tragstrukturen. Daher wird in dieser Arbeit eine – mit Hilfe eines Substrukturierungs-Ansatzes (Superelemente) – verbesserte Abbildung der Rohrknoten in der Simulationssoftware ADCoS-Offshore genutzt. Am Beispiel einer Tripod- und einer Jacket-Struktur werden Berechnungen auf Basis des bisherigen Ansatzes (Balkenmodelle), auf Basis der verbesserten Modelle (Superelemente) und mit Hilfe von Referenzmodellen (finite element (FE)-Shell-Modelle) durchgeführt. Die Ergebnisse werden verglichen und interpretiert.

Die Verwendung höherer globaler Eigenformen der Strukturen, die mit Balkenmodellen berechnet wurden – was einem verbreiteten Vorgehen entspricht – ist kritisch zu betrachten. Die untersuchten Strukturen zeigen schon bei relativ niedrigen Frequenzen Eigenformen, die mit Balkenmodellen nicht darstellbar sind.

ADCoS-Offshore wird mit einem Fokus auf dem neu integrierten Superelement verifiziert. Die folgenden Berechnungen zeigen, dass die genaue Modellierung des Eigengewichts der Strukturen in keinem der Modelle eine Herausforderung darstellt. Die Eigenfrequenzen unterscheiden sich dagegen: Diese sind grundsätzlich niedriger für die höherwertigen Modelle und für einige der Frequenzen sind die Unterschiede sehr deutlich. Dies gilt sowohl für die Tripod- als auch für die Jacket-Struktur. Die weicheren höherwertigen Modelle der Strukturen führen wie erwartet zu größeren Verformungen.

Der Lastabtrag in den verzweigten Strukturen hängt stark von der Modellierung der Steifigkeit der Rohrknoten ab und kann aus diesem Grund nicht hinreichend genau mithilfe der einfachen Balkenmodelle abgebildet werden. Die berechneten Unter-

schiede sind für die Tripod-Struktur zwar größer, sie sind jedoch auch für die Jacket-Struktur relevant. Eine allgemeine Tendenz hin zu größeren oder kleineren Lasten ist für keinen der betrachteten Modelltypen feststellbar. Dies wird sowohl durch Schnittgrößen in statischen Lastfällen als auch durch Ergebnisse von dynamischen Ermüdungslast-Berechnungen (primär mithilfe schädigungsäquivalenter Einstufen-Kollektive) gezeigt. Wie oben beschrieben lassen sich die großen Unterschiede in den Schnittlasten nicht aus den Ergebnissen von Modalanalysen ableiten – obwohl es sich bei einer dahingehenden Interpretation von Eigenfrequenzen und -formen um ein verbreitetes Vorgehen in der frühen Phase eines Entwurfsprozesses handelt.

Auf Basis der Ergebnisse der vorliegenden Arbeit wird die Verwendung von Superelementen in der aeroelastischen Modellierung von Offshore-Windenergieanlagen mit verzweigten Tragstrukturen empfohlen. Auch vereinfachte Ansätze zur Beschreibung der lokalen Knotennachgiebigkeiten sind möglich. Die Verwendung dieser alternativer Ansätze ist jedoch weniger geradlinig, weniger elegant und physikalisch weniger korrekt.

Schlagworte: Offshore-Windenergieanlage, verzweigte Tragstrukturen, Modellierung.

Acknowledgments

Claudio Hillmann, Dipl.-Math. Isabel Koprek, Wojciech Popko (M.Sc.) and my former dual leadership partner Dr. rer. nat. Bernhard Stoevesandt for the working atmosphere and the team spirit and last but not least for the fun we had working together.

Contents

CONTENTS   **xiii**

List of Figures

List of Tables

Acronyms

ADC	Aero Dynamik Consult Ingenieurgesellschaft mbH.	39, 79
ADCoS	Aeroelastic and Dynamic Computation of Systems.	v, vii, 2, 3, 25, 28, 33, 34, 39, 40, 45–47, 49, 53, 79–81, 87, 95, 103, 109, 112
AF	apparent fixity length.	35, 36, 40
BEM	Blade Element Momentum Theory.	27, 31, 33–35, 38, 40
CFD	computational fluid dynamics.	6, 26, 38
CS	coupled springs.	35, 36, 40
CS	coordinate system.	50, 57, 81, 95, 129, 131, 135, 139
DEL	damage equivalent load.	v, 54, 70, 95–98, 106–108, 110
DLC	design load case.	50, 53, 54, 95, 103, 112
DLL	dynamic link library.	30, 33–35, 38, 40
DOF	degree of freedom.	26, 30, 35, 40, 43, 44, 46, 50–52, 59, 60, 66, 67, 72, 76, 77, 79, 80, 101, 102, 106, 107, 110
DS	distributed springs.	35, 36
EB	Euler-Bernoulli.	39, 40, 70, 98, 110
FE	finite element.	vii, 2, 3, 26, 29, 30, 39, 42–46, 58, 79, 81, 111, 112
FEM	finite element method.	30, 33–35
GDW	Generalized Dynamic Wake Theory.	31, 33–35, 38
GL	Germanischer Lloyd.	54, 55
IEA	International Energy Agency.	25, 113
IEC	International Electrotechnical Commission.	37, 53, 139
IWES	Fraunhofer Institute for Wind Energy and Energy System Technology IWES.	27, 29, 32, 34, 36–38, 110
JONSWAP	wave spectrum developed during the Joint North Sea Wave Project.	14, 15
LCoE	levelized cost of energy.	2, 109
LJF	local joint flexibility.	vi, 3, 41, 42, 109, 111, 112
MBS	multibody simulation.	29, 30, 33–35, 38, 39
MSL	mean sea level.	18, 56–58, 71, 81, 133, 139
NREL	National Renewable Energy Laboratory.	22, 24, 33, 34, 36, 55, 79
OC3	Offshore Code Comparison Collaboration.	25, 33, 36, 55, 59, 60, 64–66, 79, 80, 110
OC4	Offshore Code Comparison Collaboration Continuation.	25, 36, 37, 68, 70–72, 74, 76, 113

OC5	Offshore Code Comparison Collaboration Continuation with Correlation. 113
OWT	offshore wind turbine. v, 1–3, 5–8, 11, 13, 14, 17–26, 28, 29, 31, 33, 35–40, 42–44, 47, 52–55, 60, 70, 76, 79–81, 91, 109–113, 139
PM	Pierson-Moskowitz Spectrum. 14, 15, 54
RAVE	Research at Alpha Ventus. 37, 113
RNA	rotor nacelle assembly. 3, 28, 29, 35, 39, 49, 55, 59, 64, 68, 74, 76
TP	transition piece. 18, 21, 68, 72, 101, 110
WT	wind turbine. 1, 6, 9, 11, 14, 20, 22, 23, 25–28, 30–33, 35, 37–40, 57, 59, 109, 112

List of Symbols

Greek letters

α	°	angle between wave direction and global x-axis. 54
α_{br}	—	brace length to diameter ratio. 71
α_{ch}	—	chord length to diameter ratio. 71
β	°	angle between wind direction and global x-axis. 54, 105
β_b	—	diameter relation in Buitrago's approach. 41, 42
γ	—	chord diameter related to doubled thickness in Buitrago's approach. 41, 42
γ_j	—	peak shape parameter (JONSWAP spectrum). 15, 16
$\Delta\varphi$	%	rotational displacement difference. 95
Δb	$\mathrm{m/s}$	wind speed bin size. 8, 9, 54
Δf	%	frequency difference. 60, 62, 66, 70, 72, 74, 76, 87, 91, 100, 110
ΔF	%	force difference. 81, 107, 108
Δm	%|tons	mass difference. 60, 62, 70, 73, 89, 90, 99
Δu	%	translational displacement difference. 95, 101, 102, 105, 107, 110
ζ	—	gap between braces related to chord diameter in Buitrago's approach. 41, 42
θ	°	brace angle in Buitrago's approach. 41, 42
λ	m	wave length. 11–13
μ	—	Wöhler Material Exponent. 50, 127
ν	—	Poisson's ratio. 50, 127
$\rho_{\mathrm{fl.}}$	$\mathrm{kg/m^3}$	flange density. 60, 73, 129
ρ_{grow}	$\mathrm{kg/m^3}$	marine growth density. 69, 137
ρ_s	$\mathrm{kg/m^3}$	steel density. 50, 127
ρ_{w}	$\mathrm{kg/m^3}$	water density. 32
σ	$\mathrm{m/s}$	standard deviation. 9, 15
σ_j	—	spectral width parameter in JONSWAP spectrum. 15
τ	—	wall thickness relation in Buitrago's approach. 41, 42
φ	°	rotational displacement. 93, 96
$\underline{\varphi}$	—	eigenvector. 51
$\underline{\underline{\Phi}}$	—	modal matrix. 51
ω	$\mathrm{rad/s}$	angular frequency. 12, 50

Roman letters

a	m	wave amplitude. 12
A_γ	—	normalizing factor of the JONSWAP spectrum. 15
Av	%	turbine availability. 22, 54
c	$\mathrm{N/m}$	damping constant. 50
C_a	—	water added mass coefficient. 32
C_d	—	drag coefficient. 32, 37
$\underline{\underline{C}}$	—	damping matrix. 44, 51, 53
$\underline{\underline{C}}_c$	—	structural damping matrix. 53

n_shell	—	number of DOFs for shell model. 66, 76
n_shj	—	number of DOFs for shell-joint model. 66, 77
n_super	—	number of DOFs for superelement model. 67, 77, 110
N_ref	—	reference number of cycles. 55
N_{20}	—	number of cycles over 20 years. 22
O_year	—	occurrence per year. 54
q_d	$\mathrm{N/m}$	drag force per length. 32
q_m	$\mathrm{N/m}$	inertia force per length. 32
q_wave	$\mathrm{N/m}$	wave force per length. 32
$\underline{\underline{R}}$	—	reaction force matrix. 48
$\overline{S_j(f)}$	$\mathrm{m^2s}$	JONSWAP Spectrum. 15
$S_k(f)$	$\mathrm{m^2/s}$	Kaimal Spectrum. 9
$S_\mathrm{pm}(f)$	$\mathrm{m^2s}$	Pierson-Moskowitz Spectrum. 15
t	m	wall thickness. 56, 67, 69, 133, 137
t	s	time. 12, 50
T	s	wave period. 13
t_grow	m	marine growth thickness. 6, 69, 137
t_j	m	brace wall thickness in Buitrago's approach. 42
T_i	%	turbulence intensity. 9, 10, 54
T_j	m	chord wall thickness in Buitrago's approach. 42
T_p	s	spectral peak period. 15, 35, 54
T_sea	s	averaging time (sea state). 15
T_sf	s	period of stream-function wave. 57, 81
T_tot	years	total turbine lifetime. 22
T_wind	s	averaging time (wind field). 8, 15
T_z	s	zero (up-) crossing period of irregular wave. 14–16
$\underline{\underline{T}}$	—	transformation matrix in static condensation. 44
u	m	displacement. 50, 92, 93, 96, 101, 107
$\dot{u}$	$\mathrm{m/s}$	velocity. 32, 50
$\ddot{u}$	$\mathrm{m/s^2}$	acceleration. 32, 50
$\dot{u}_w$	$\mathrm{m/s}$	horizontal water particle velocity component. 12, 32
$\ddot{u}_w$	$\mathrm{m/s^2}$	horizontal water particle acceleration component. 12, 32
$\underline{u}$	—	displacement vector. 43, 44, 51, 53
$\underline{\dot{u}}$	—	velocity vector. 44, 53
$\underline{\ddot{u}}$	—	acceleration vector. 44, 53
$\underline{u}_a$	—	displacement vector in static condensation (master nodes). 43, 44
$\underline{u}_c$	—	displacement vector in static condensation (slave nodes). 43
V	—	dynamic amplification factor. 50
V_w	$\mathrm{m/s}$	average wind speed. 8–10, 15, 35, 54, 105
$\dot{w}_w$	$\mathrm{m/s}$	vertical water particle velocity component. 12
$\ddot{w}_w$	$\mathrm{m/s^2}$	vertical water particle acceleration component. 12
$\underline{y}$	—	vector of generalized nodal coordinates. 51, 52
$\underline{\dot{y}}$	—	vector of generalized nodal velocities. 51
$\underline{\ddot{y}}$	—	vector of generalized nodal accelerations. 51, 52

Indices and modifications

$\square_i$	general running index.
$\square_x$	x direction.
$\square_y$	y direction.
$\square_z$	z direction.
$\square_\mathrm{beam}$	concerning the beam model.
$\square_\mathrm{super}$	concerning the superelement model.
$\square_\mathrm{shell}$	concerning the shell model.

$\square_{\mathrm{shj}}$	concerning the shell-joint model.
$\square_{\mathrm{min}}$	minimum value.
$\square_{\mathrm{max}}$	maximum value.
$\dot{\square}$	first time derivative.
$\ddot{\square}$	second time derivative.
$\underline{\square}$	vector.
$\underline{\underline{\square}}$	matrix.
$\overline{\square}'$	modal.

Chapter 1

Introduction

1.1 Background and motivation

On July 11, 1991, the Vindeby Offshore Wind Farm, the first Offshore Wind Farm in the world started feeding electricity to the grid (Figure 1.1 shows the installation of one of the eleven 450 kW units). Since then, Offshore Wind Energy developed from this early experiment to a multibillion dollar market and an important pillar of the worldwide renewable energy production. Unit sizes grew from 450 kW at Vindeby to the 7.5 MW-class OWTs currently (by August 2014) in the prototyping phase. With increasing turbine sizes and greater water depths at projected sites, multi-member support structures such as jackets and tripods became technically and economically feasible. Since the first erection of a wind turbine (WT) on a jacket structure in Beatrice Field in Scottish territorial waters in 2006, branched structures are being installed and planned in increasing number. These are mainly jackets and tripods (and triples) and, even with the current development towards very large monopiles, it is still expected that especially jackets will have their share of future projects depending on turbine size, water depth, wave climate and soil conditions.

Offshore wind energy is a young industry and serial production of support structures just kicked off, it is certainly immature compared to other industries producing large quantities of one type of machine, e.g., the automotive industry. Larger series production and local and system-wide optimizations will improve the design, manufacturing and eco-

Figure 1.1: Turbine installation at Vindeby Offshore Wind Farm[1].

nomics of OWTs. However, as long as site-specific design is required, the economies of scale cannot be applied, at least not to the structure as a whole. Production costs combined with the financial and technical risks in the offshore wind sector (compared to onshore wind) must be considered. So even for production runs with only a few structures, this justifies higher engineering effort that results in lower safety factors and, therefore, more optimized products.

The support structure leads to a significant share of the capital expenditure (capex) of an OWT and further optimization of the structures - with the turbine atop in a system approach – can support levelized cost of energy (LCoE)[2] reduction that finally leads to a subsidy-independent offshore wind energy future. Design and certification of these structures is based on load assumptions gained from extensive simulations. Loads simulation is a complex task, however, the effort is necessary as high availability and cost effectiveness is only achievable when (1) all significant load effects[3] are predicted accurate enough to guarantee a reliable design, and (2) the load effects are not massively overestimated leading to high reserve which indicates a design that is not cost effective[4]. Therefore, a deep understanding of system behavior and a detailed knowledge of load effects is vital for the use of this optimization potential, which is where this work comes into play. Herein, the loads simulation tool ADCoS in its offshore version (ADCoS-Offshore) including a new superelement feature is used to perform investigations on an OWT with a jacket and a tripod structure. The more accurate simulation leads to a better understanding of the system OWT with jacket or tripod support structures with a focus on the support structure itself.

1.2   Objectives and methodology

OWT system development has been realized in recent years in parallel with the development of the respective aeroelastic tools[5] that are used for calculating load effects of these systems. Currently, the use of beam models or modal reduced beam-like models is common to represent the support structures within these tools. This is the case even with the inaccuracy of beam models – when modeling joints of branched steel structures of the respective type – that is known from the offshore oil and gas industry. On top of that, the joints are often the critical fatigue driven parts of multi-member support structures. The use of parametric formulae – that were developed in the early nineties and found their way to the respective guidelines and standards – is a reasonable approach to deal with this issue even with these formulae being developed for parameter ranges of oil and gas jackets (e.g. diameter relations between brace and chord members). To deal with other simulation tasks and / or in other industries, the use of superelement or substructuring approaches – that were developed in the mid sixties – in FE analyses is very common. The parametric formulae that are widely used, as well as the superelements that are used herein are both based on more detailed FE shell models[6], but the deriva-

---

[1]http://www.ewea.org/fileadmin/apps/30years/; August 5, 2014.

[2]LCoE is used herein even if it is more reasonable to use the up-to-date definition of Society's Cost of Electricity (SCoE), (http://www.gwec.net/wp-content/uploads/2014/04/GWEC-Global-Wind-Report_9-April-2014.pdf; September 26, 2014) in discussions on cost of energy.

[3]In this work, the IEC definition for load effects is used: "load effect: effect of a single load or combination of loads on a structural component or system, for example internal force, stress, strain, motion, etc." (IEC 61400-3 (2009), Section 3.19, p.11). This is equivalent to the system's reaction to external loading.

[4]In general, uncertainties lead to higher safety factors and these in turn lead to higher cost.

[5]The labels aeroelastic tool, aero-hydro-servo-elastic tool, wind turbine simulation tool, wind turbine global dynamics tool and wind turbine design tool are often used synonymously – even if the commonly used term design tool is not precise because the tools are rather simulation tools than design tools.

[6]The suitability of shell elements is generally not put in question – as long as the modeling is realized carefully - for (1) the structures investigated herein at (2) the structural model fidelity that is of interest for this work. Section 2.3.4 provides a description how the probability of modeling errors is minimized based on experience

tion of the superelements is more straightforward and leads to more accurate representations. The stiffness relations between the connecting points of the residual structure are the same when a shell joint is replaced by a superelement – for any parameter range.

In this work, a superelement feature in the aeroelastic tool ADCoS-Offshore is developed, verified and used for simulation of an OWT model with a jacket- and with a tripod support structure. Conclusions on the structural behavior are drawn. Modeling for loads simulation is brought to a new level by providing the possibility to use a well proven FE procedure in a new context. The detailed shell models – that are used in detailed design of the investigated structures and that were even the base for the development of the commonly used parametric formulae – are used as a reference in the model development and in preliminary numerical comparisons.

1.3   Structure of the thesis

This thesis deals with the development of a superelement feature to include LJF in the loads simulation tool ADCoS-Ofshore for OWTs with branched support structures, and the respective simulation results. After this introduction, it continues with a chapter on dynamics of OWTs (**Chapter 2**) that describes aspects of the offshore environment, the properties of OWTs and the state of the art in loads simulation. The onshore version of ADCoS and the state of the art concerning joint modeling of offshore structures are presented subsequently. In **Chapter 3**, the development of ADCoS-Offshore is described. The focus is on the application of wave loading to the already validated ADCoS for onshore use and on the joint modeling using superelements. **Chapter 4** describes load cases and the rotor nacelle assembly (RNA) model used in the thesis. Furthermore, it depicts the development of a set of structural models of a generic tripod- and jacket support structure. Some of these models are used in **Chapter 5** for the verification of the newly developed superelement feature in ADCoS-Offshore, but the main purpose of the modeling effort is the comparison of the calculated results for both support structure types in **Chapter 6**. The contribution to the state of the art is summarized, recommendations for possible application of the results presented herein are given, and future research work is presented in **Chapter 7**.

---

and Chapter 4 explains the application of the findings in this work.

Chapter 2

State of the art of offshore wind turbine dynamics

This chapter gives the background on dynamics of OWTs from the turbine designer's or from a loads simulation point of view. It is subdivided in Section 2.1 for a description of the environment and the resulting loads, Section 2.2 to provide background on the system OWT itself and finally, in Section 2.3, an overview on the state of the art in simulation of this system in the marine environment is presented.

A distinction of descriptions of the physical system on the one hand, and the modeling of this system on the other hand, is not realized in a strict sense in this chapter, because a formally correct approach in this context would not lead to a readable document. That means, that Section 2.1 and Section 2.2 already cross the borderline between system description and modeling. Nevertheless, Section 2.3 gives a general introduction to modeling.

Apart from the above mentioned, an attempt is made to split up the following when it comes to the rotor and the support structure: The *physical description* of the structure as well as loads and loads effects (Section 2.2.1 for the support structure and Section 2.2.2 for the rotor), the approaches to *model* the physics (Section 2.3.2) and the *implementation* in the respective tools (Section 2.3.3).

The basics chapters of Van der Tempel (2006) are recommended for an introduction in OWT technology and environment. A more comprehensive overview is provided for example by Burton et al. (2011).

2.1   Environment and resulting loads

In this section, the marine environment is described with respect to the engineering requirements for OWT simulation that needs to cover the damaging influences during erection and operation of the turbines. Most of those environmental influences were well known either from the onshore wind energy or from the offshore oil and gas sector even before large scale offshore wind developments.

- Corrosion. Compared to onshore wind energy special measures are required to protect the turbine in the more corrosive marine environment. One possibility to protect the sensitive parts of the machine inside tower and nacelle is to use air intake filters combined with an over pressure in nacelle and tower to assure that only

desalinated air is in contact with those parts. This is the case for Areva machines for example[1]. To protect the support structure, active as well as passive corrosion protection is used as described in standards for comparable offshore structures (see NORSOK M-501 (2012), NORSOK M-503 (2007)).

- Lightning. Lightning protection systems are installed on the nacelle and in the blades of OWTs just as in the onshore wind application (see IEC 61400-1 (2005)).

- Ship collision. Especially for wind parks near much frequented sea lanes there is a considerable danger of collisions. In those cases, the probability of a collision as well as the severity of the results in case of a collision have to be investigated (see Christensen et al. (2009), Randrup-Thomsen et al. (2009), Biehl (2004)).

- Earthquake. In areas with high seismic activity, loads resulting from earthquakes are taken into account. For OWTs the calculation of loads from earthquakes is described in IEC 61400-1 (2005). A guideline for a conservative design with respect to earthquakes is given in the same standard.

- Ice loads. Ice accretion on blades leads to mass imbalances and reduced aerodynamic performance. Respective knowledge has historically been developed in the aerospace industry and ice accretion simulation tools were designed for aircraft purposes (see Kind (2001)). Basically, the physical phenomena in aircraft and wind turbine airfoil icing are comparable. Purely wind energy specific ice accretion simulation tools are narrowed down to the following stand-alone tools: Lewice[2], canice (Paraschivoiu and Saeed (2001)), the respective version of fensap-ice[3] and turbice (Makkonen and Laakso (2001)). One hybrid solution, i.e. combination of tools, is available: Lewice combined with computational fluid dynamics (CFD).

  Icing of the support structure reduces the accessibility of an OWT and locally increases the mass of the structure. This leads to modified natural frequencies. Furthermore, the structural diameter and therefore wave loads are increased. Dynamic loads from drifting or breaking ice may be taken into account in the early design phase and lead to the construction of ice-breaking cones. Even if the sea is ice-free, icing of the support structure can occur in the splash zone. Ice loads on WT structures in danish waters are investigated in Barker et al. (2005a,b). The respective standards like IEC 61400-3 (2009) give instruction in terms of sea ice loading. In Laakso et al. (2010), wind energy in cold climate is addressed more in a more general way.

- Marine growth. Marine growth or fouling on support structures of OWTs leads to increased masses and therefore reduced natural frequencies as well as to a larger diameter and higher surface roughness and therefore increased wave loads. Hard and soft fouling are distinguished. Hard fouling, a cover of sea shells for example, can have an approximate thickness of up to $t_{\mathrm{grow}} = 200\,\mathrm{mm}$ whereas soft fouling, as seaweed for example can have a thickness, or length, of up to some meters.

- The soil properties. These properties differ in many respects from onshore conditions. One example is the occurrence of scour holes: Waves and currents wash away the soil around offshore foundations. Especially for sandy soils, the resulting scour holes lead to reduced embedded length of the piles under mudline. This leads to reduced bearing capacity of the piles in combination with lower natural frequencies. Designing piled offshore support structures following the specifications in GL Offshore (2012), a scour depth of up to 2.5 pile diameters must be considered. However, this value might differ depending on the standard or guideline

---

[1]http://www.areva-wind.com/fileadmin/infomaterial/AREVAwind_M5000_uk.pdf; October 2, 2014.
[2]http://icebox.grc.nasa.gov/design/lewice.html; October 2, 2014.
[3]http://newmerical.com/fensap-ice/; October 2, 2014.
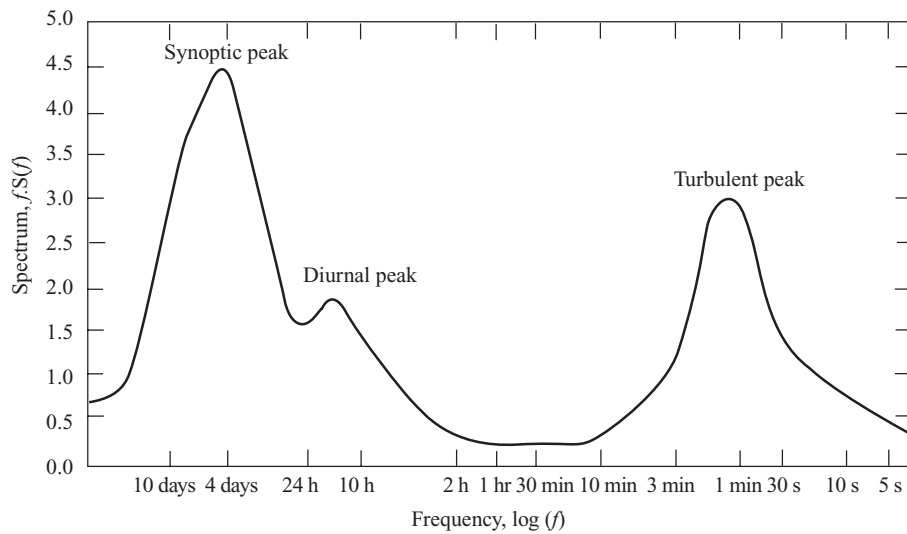
Figure 2.1: Wind speed fluctuation spectrum from days to seconds modified from Burton et al. (2011) originally published in Van der Hoven (1957).

that is used. As scour protection rock layers or layers of geotextile containers may be used as described in Grüne and Oumeraci (2007).

- Currents. Tidal, storm surge or atmospheric pressure variation induced sub-surface currents, wind generated near surface currents and near shore wave induced currents are distinguished. In IEC 61400-3 (2009) it is stated, that currents may be irrelevant for fatigue assessment, but extreme hydrodynamic loads may differ significantly especially for large volume structures such as gravity bases if a sea current is superimposed. This is due to the fact that currents may not increase amplitudes of fluctuating loads but shift the average values only.

- Water level. Water level differences are taken into account in loads simulation. In IEC 61400-3 (2009) for example minimum and maximum water levels due to astronomical tides, storm surges and wave heights are described to be applied in loads simulation and for definition of areas with different corrosion regimes.

The main mechanical loads on OWTs result from wind loads on the rotor and wave loads on the support structure, therefore those load sources are described in more detail in Section 2.1.1 (wind) and Section 2.1.2 (waves).

2.1.1 Wind

Wind speeds and directions are fluctuating on different scales in time and space by nature. The spatial scales vary from the global wind systems mainly affected by temperature differences due to differing solar radiation in polar and equatorial regions down to small scaled fluctuations in the range of centimeters. Concerning the changes over time, periodic phenomena with periods of several years can be observed as well as high frequent oscillations up to a scale of seconds. The very low frequencies are relevant for energy yield predictions, but not for loads simulations. The range that is of interest for loads simulation falls between several days and a few seconds and is shown in Figure 2.1.
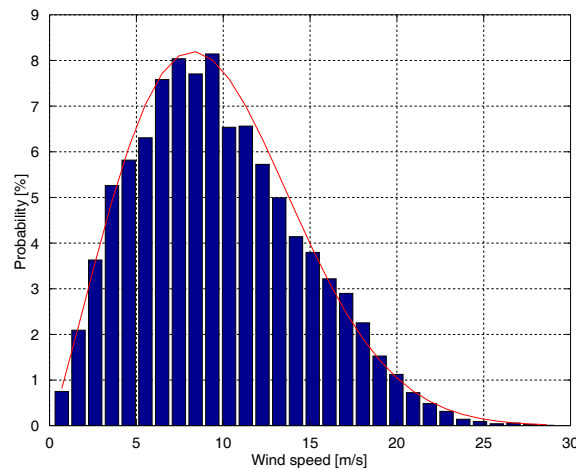
Figure 2.2: Bar chart of average wind speeds (10-min. average) and Weibull fit.

The spectral gap[4] between the high frequency oscillations on the right-hand side of the spectrum and the low frequency oscillations at the left-hand side, showing the low energy content in this range of frequencies, is directly visible. The synoptic peak results from changes due to crossing weather phenomena. The diurnal peak represents night and day changes and the turbulent peak represents high frequency fluctuations. To describe the random nature of the wind, time series with a given average wind speed V_w and a length of $10\,\mathrm{min} \leq T_{\mathrm{wind}} \leq 1\,\mathrm{hour}$ are mainly used, because this length range lies in the spectral gap[5]. Due to that, the error, when assuming a stationary stochastic process is minimized and the wind may be described separately for the lower frequency range and for the higher frequency range as described in the following.

Long term wind statistics

In the lower frequency range it was found, based on measurements, that a Weibull function fits the distribution of the average wind speeds relatively well at most sites. Figure 2.2 shows a bar chart giving the average wind speed probabilities and the respective Weibull fit. Site-specific measurement data or the Weibull distribution are, therefore, used to describe the distribution of the average wind speeds for loads simulation.

With each of the bars shown in Figure 2.2, a directional distribution is associated that can be visualized in a wind rose. In Figure 2.3, each of the wind roses that are shown represents a wind speed range (bin) of Δb. The values in the figure next to the respective wind rose give the median of the bin. This is a commonly used bin size, a useful compromise between accuracy and effort. However, the bin size may be halved in special cases.

Short term and small scale wind speed fluctuations

Looking into smaller sizes in space, the wind speeds at heights that encompass the turbine rotor are relevant for loads simulation. These wind speeds increase with height due

---

[4]The significance and even the existence of this gap is widely discussed (e.g. Panofsky and Dutton (1984)), but it is commonly used in engineering applications as described in the following.

[5]This is common in the offshore wind industry, even if the use of three-hour events is a standard in the oil and gas industry. Floating OWTs are an exception. Here, the necessity of longer time series is accepted even if the low rigid body motion eigenfrequencies are seen as the main reason and not the environmental conditions.
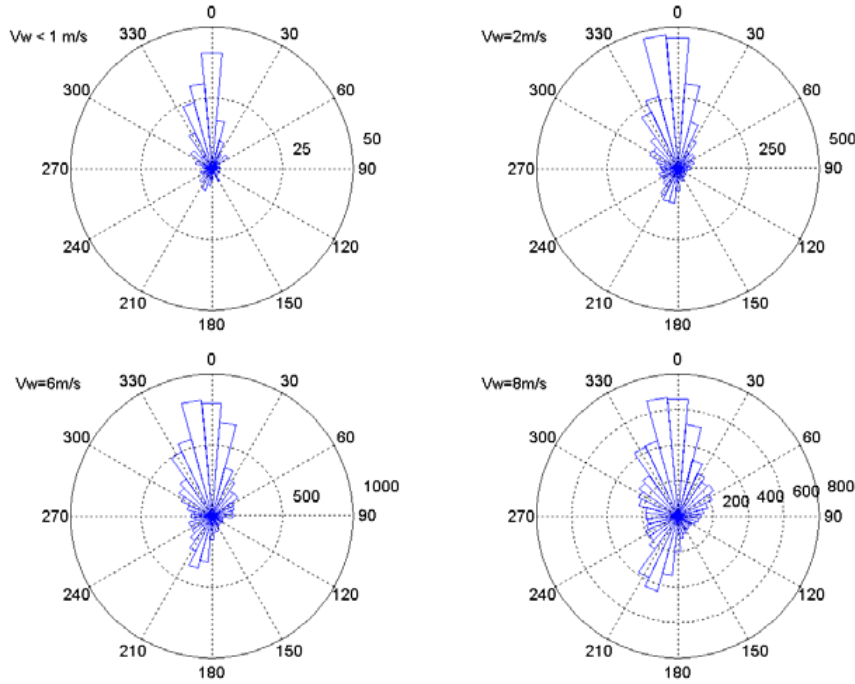
Figure 2.3: Wind roses for exemplary wind speed ranges (bins) of a size of $\Delta b = 2\,\mathrm{m/s}$ at a Dutch North Sea site (modified from Fischer et al. (2010)).

to the atmospheric boundary layer (wind shear). The shape of the wind shear profile is highly dependent on the surface, characterized by its roughness, and the temperature distribution. For loads simulation, the profiles are approximated with logarithmic or power law functions as shown in Figure 2.4. The figure gives four wind shear profiles: Two profiles with a typical surface roughness for an onshore site with flat terrain (red: power law; black: logarithmic) and two profiles with a typical surface roughness for an offshore site (blue: power law; green: logarithmic). The respective equations are given e.g. in Section 3.65 of IEC 61400-3 (2009)).

Based on measurements with high resolution in time and space, the random small-scale variations of wind speed and direction (or wind velocity as a three dimensional vector) were analyzed extensively in the past. Such time series may basically be described in the frequency range based on a spectrum giving the frequency dependent energy content of the fluctuations (as already shown in Figure 2.1). In WT loads simulation, different spectra are commonly used with the basic input parameters V_w as described above, and a standard deviation σ or turbulence intensity

$$T_i = \sigma/V_w. \tag{2.1}$$

Generally, σ increases, and T_i decreases with increasing V_w. Equation 2.2 gives a Spectrum as defined by Kaimal et al. (1972):

$$\frac{fS_k(f)}{\sigma^2} = \frac{4fL_k/V_w}{(1 + 6fL_k/V_w)^{5/3}}. \tag{2.2}$$

The frequency f, the frequency dependent velocity spectrum $S_k(f)$, a length scale L_k and the wind speed V_w are used in this equation. Commonly used spectra are defined, and a larger set of spectra used in current standards is compared by Burton et al. (2011).
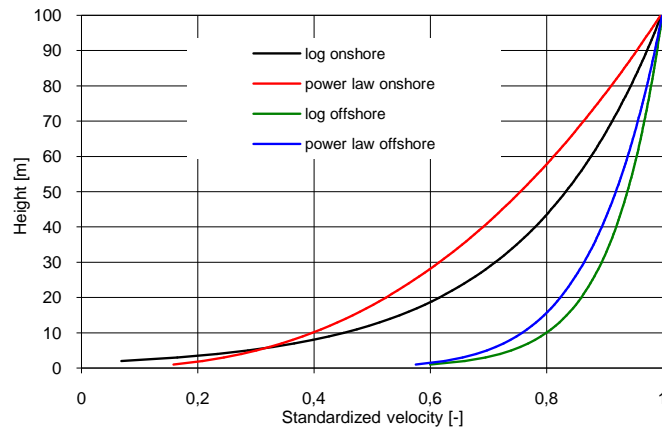
Figure 2.4: Logarithmic and power law wind shear profiles for an onshore site and for an offshore site.
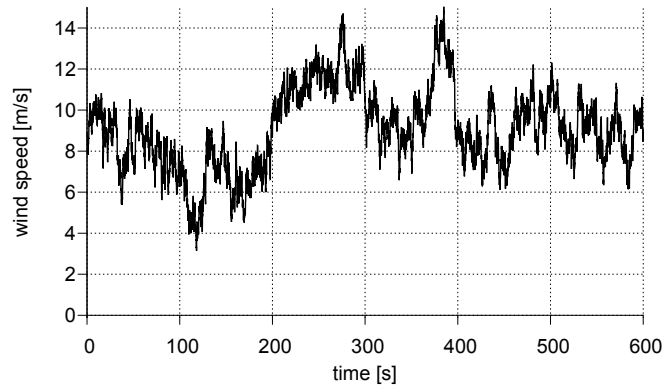
Figure 2.5: Generic wind time series for $V_w = 9\,\mathrm{m/s}$ and $T_i = 20\,\%$ (modified from Xiros (2015)).

When detailed measurements are not available, the spectra are used to generate generic time series. As an example, Figure 2.5 shows a time series generated with a Kaimal Spectrum for an average wind speed of $V_w = 9\,\mathrm{m/s}$ and a turbulence intensity of $T_i = 20\,\%$. The Mann model (cf. Mann (1998)), that is used to generate three dimensional and fully correlated wind fields becomes more and more common in loads simulation.

Above, single-point time history data or spectra are described, however, variation of this speed across the rotor disk is important for turbine loading. So, a grid of points over the rotor disc is typically applied. Because the described air flow is a fluid flow, the wind speed at a given time at each point is correlated to the wind speeds at the other points in the described area. The correlation decreases with increasing distance between the considered points and with increasing frequency. The mathematical formulations of the coherence functions (i.e. the correlation between two points on such a grid) are commonly given in the appendices of the standards.

The current approaches lead to acceptable results; however, in complex terrain, such as hilly forests and in wakes of other turbines, the methods have important limitations. In the respective standards, approaches are described to account for wake effects. In large wind farms, relatively simple models are used to calculate increased turbulence intensities and decreased average wind speeds to simulate wake effects. See Section 2.3

as well for more information on wind field simulation and ongoing research on wake effects.

Extreme wind speeds and gusts lead to extreme loads on WTs. These events are treated separately because of their importance in WT design. This is particularly true for extreme load calculation of gusts, that typically have durations of a few seconds to minutes, and are not covered very well in the aforementioned approach. Those incidents occur randomly and can be described with so-called n-year wind speeds, which give the maximum average wind speed over a given time interval that is statistically exceeded once in n years.

As measured data over the necessarily long time periods are rarely available, extrapolations can be performed using extreme value distributions. In the respective guidelines, sites for WTs are classified and the values, for example 50-year wind speeds, are given for each class (see e.g. GL Offshore (2012).)

Gust wind speeds over time are simplified and described with different approaches. A one-minus-cosine, or a *Mexican-hat-like* gust shape (GL Offshore (2012), Kühn (2001)) are common. Other shapes and combinations with wind direction changes may be found in the respective standards like IEC 61400-3 (2009)[6].

2.1.2   Ocean waves

Apart from tsunamis (seismic sea waves), very small waves (dominated by water surface tension effects) and tidal waves, ocean waves are wind induced (water is deflected due to wind by friction) gravity (restoring force) waves.

With upcoming wind small waves develop, the amplitude and wave length of those waves increases with wind speed and with the distance the wind is acting over the sea, the fetch length. Simultaneously, small waves, interfering with the bigger waves, emerge continuously. A constant wind condition over a sufficient fetch length and over sufficient time leads to a sea state that is related directly to the wind speed. In this case, the sea state would be fully developed and unidirectional (long-crested waves).

Especially for strong winds, the described situations – or conditions close to it – are rare. Wind direction changes, intersecting wave systems, different water depths, different natures of the seabed and the influence of the coastlines lead to an irregular short-crested sea surface in reality.

Herein, the field of water-wave description and resulting loads is strongly compressed while focused on the needs of OWT loads simulation and structural modeling. For details and a wider focus see e.g. Sarpkaya and Isaacson (1981) or Chakrabarti (2005). Breaking waves and higher order effects are not described here. Structures are assumed to be hydrodynamically transparent (small structural diameters D relative to the wave length λ); feedback from (moving) structures to the wave field (reflection, refraction, diffraction) is not taken into account[7]. Based on that, the wave loads topic is divided into the description of the water particle movement (this section) and the calculation of the load on the structure based on these kinematics. This is described in Section 2.3.2 for the OWT loads simulation application. The kinematics calculation is limited to regular, i.e. deterministic (linear and nonlinear) and irregular, i.e. stochastic (linear) waves or sea-states. Nonlinear irregular approaches are not discussed in detail here, the reader is referred to e.g. Mit-

---

[6]Gusts are short term wind speed fluctuations and therefore theoretically covered by the above mentioned spectral approach. But their special importance for OWT makes it reasonable to use supplementary gust descriptions considering parameters like the point in time associated with the fastest change of the wind speed for example. Furthermore, gusts are combined with wind direction changes.

[7]Even if these effects might become important for structural diameters in the range of the tripod central joint, it is uncommon to consider these in loads simulations.

tendorf (2006). Amongst others, Mittendorf compared water particle kinematics of nonlinear irregular waves obtained with two different methods to wave flume measurement results. He concluded that the kinematics predicted by the local Fourier approximation method described by Sobey (1992) showed good agreement with the measured data, so this might be a reasonable approach towards nonlinear irregular wave consideration.

Wave theories

Water waves can simply – and relatively accurate – be approximated with a linear water surface elevation in the case of small amplitude waves in deep water. With increasing wave height and decreasing water depth (or both), the wave shape becomes steeper – it becomes nonlinear – until the wave brakes.

The Airy wave theory[8] based on the work of G.B. Airy (cf. Airy (1845)) is an easily applicable theory to describe wave particle kinematics. Using this theory the fluid is considered as nonviscous, irrotational and incompressible, a potential flow problem. This is further simplified via linearization of the nonlinear boundary conditions. Furthermore, a free surface of infinite horizontal extent and a horizontal see bottom are assumed. The resulting problem is solved analytically and leads – amongst others – to a description of the water particle kinematics for deep water waves (high water depth to wave length ratio d/λ) as shown in Equation 2.3 to Equation 2.6. The velocity field of the two dimensional wave is described in terms of the horizontal velocity $\dot{u}_w(x, z, t)$ and the vertical velocity $\dot{w}_w(x, z, t)$. The horizontal velocity component is

$$\dot{u}_w(x, z, t) = a\omega \frac{\cosh(k_w(d + z))}{\sinh(k_w d)} \sin(\omega t - k_w x) \tag{2.3}$$

and the vertical velocity component $\dot{w}_w$ is

$$\dot{w}_w(x, z, t) = a\omega \frac{\sinh(k_w(d + z))}{\sinh(k_w d)} \cos(\omega t - k_w x). \tag{2.4}$$

The time derivatives of the velocities are the accelerations and written as

$$\frac{\partial \dot{u}_w}{\partial t}(x, z, t) = \ddot{u}_w(x, z, t) = a\omega^2 \frac{\cosh(k_w(d + z))}{\sinh(k_w d)} \cos(\omega t - k_w x) \tag{2.5}$$

for the horizontal acceleration component $\ddot{u}_w$ and as

$$\frac{\partial \dot{w}_w}{\partial t}(x, z, t) = \ddot{w}_w(x, z, t) = -a\omega^2 \frac{\sinh(k_w(d + z))}{\sinh(k_w d)} \sin(\omega t - k_w x) \tag{2.6}$$

for the vertical acceleration component $\ddot{w}_w$. The wave amplitude a, the angular frequency ω, the wave number $k_w = 2\pi/\lambda$, the water depth d and global coordinates are used in Equation 2.3 to Equation 2.6.

This description leads to a sinusoidal surface elevation. The maximum velocities and accelerations are found at the water surface, their magnitudes are decreasing fast with depth following the hyperbolic functions. The basic formulation of Airy wave theory does not provide any kinematics information above the still water line, this is accounted for with stretching methods extrapolating the kinematics to the actual elevation (see Wheeler (1970) for the so-called *Wheeler Stretching*.

For deep water waves, the water particles move in closed circles. Due to the boundary condition at the bottom that sets the vertical motion to zero, the circles become more and more flat ellipsoids towards the bottom in shallow water. Figure 2.6 shows the water particle trajectories for a typical shallow water wave (left) and a deep water wave (right).

---

[8]also linear wave theory or small amplitude wave theory
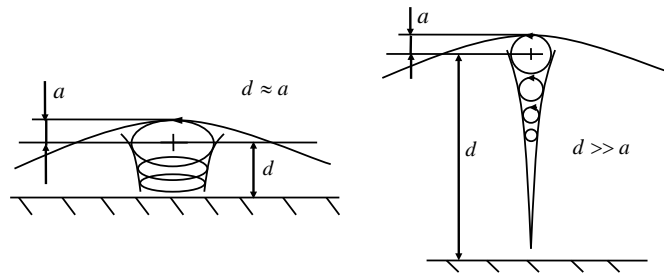
Figure 2.6: Water particle trajectories as described with linear wave theory (modified from Vorpahl (2006)).

Airy wave theory is widely used despite its theoretical limitation to waves with small to moderate wave heights and the missing description of the kinematics above the still water line in its basic formulation. This is mainly due to its simplicity, and the linear formulation that allows for superposition of Airy waves (or wavelets) to irregular sea states. Linear wave theory is described in more detail in Hapel (1990). For a very clear description see also Krogstad and Arntsen (2000).

Stream-function wave theories have been developed for the numerical description of highly nonlinear waves. Refer to Dean (1965) and Chaplin (1980) for the stream-function theory as implemented in the software used in this work. These theories describe the water surface elevation using a linear term and the superimposed harmonics of the fundamental wave frequency. The order of the stream-function wave theory refers to the highest order harmonic used in the calculation. The resulting surface profile is symmetric vertically through the crest, with a higher and steeper crest and a flatter trough than a linear wave. Using high order stream-function wave theories, water waves near the breaking limit can be described. Usually, stream-function waves are calculated for a given wave with increasing order of the theory until the resulting kinematics converge.

The water particles of ocean waves have an average velocity in the direction of wave propagation. That means, that there is a mass transport along this direction which is called Stokes Drift. Consequently the orbital particle paths as described are open. Wave theories like the linear theory, or the stream-function wave theory in the basic formulation do not take this fact into account, but superimposing a slow constant current this limitation may be overcome.

Figure 2.7 shows regions of validity of common wave theories. Description of the Stokes theories mentioned in the figure and explanations on the areas of application of the theories – for example with a focus on analytical theories – can be found in Wilson et al. (2003). These topics are not of primary interest for OWT loads simulation, where mainly Airy- and stream-function wave theories are used.

In this figure the wave height H is shown over the water depth d, whereas both values are made dimensionless with the square of the wave period T^2 and the acceleration due to gravity g. The curve at the left shows the wave breaking limit, and the height H_b is the wave height at this limit. With $H \geq 0.9H_b$ none of the described theories is valid. For shallow water waves, one breaking limit is defined by the ratio of wave height to water depth, its value is approximately $H/d = 0.78$. For deep water waves, the wave global steepness of $H/\lambda = 0.14$ (with the wave length λ) is the theoretical limiting parameter.

Small amplitude waves in deep waters may be described with linear wave theory, but with increasing ratio of wave height to water depth, the more complicated nonlinear theories are applied. Big shallow water waves can only be reasonably described using a higher-order stream-function wave theory as shown in Figure 2.7. See Goda (2010) for
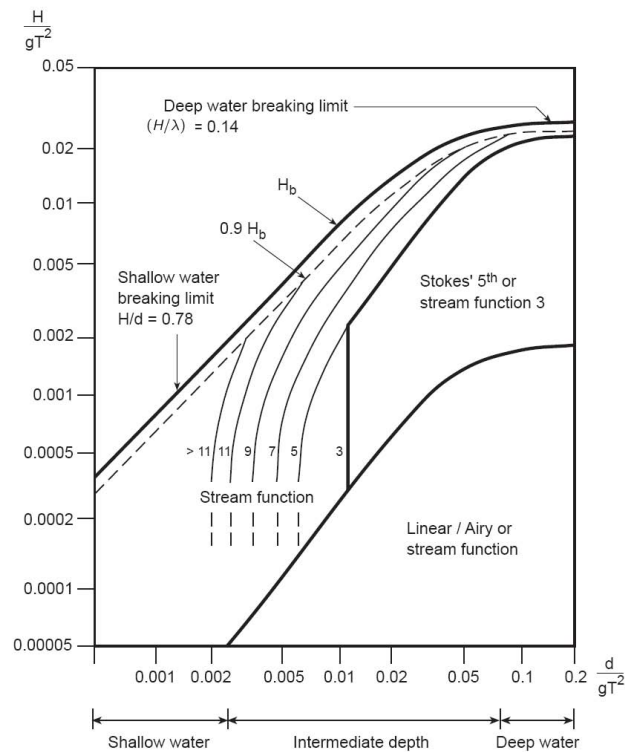
Figure 2.7: Applicability of different wave theories (Figure 4.G.1 of GL Offshore (2012)).

other wave theories.

As WTs are installed in relatively shallow waters, compared to other offshore structures, the areas of applicability that are described here are of particular importance for the offshore wind application.

Short term and long term stochastic sea state description

Measuring water surface elevation at a fixed position leads to a random time series and cannot realistically be described with a single periodic wave. Still the frequency-dependent energy content of such a time series can be described in the frequency domain with a wave spectrum (short-term statistics). This leads to a realistic energy distribution over a range of frequencies, but the sea state is assumed to be uni-directional (long-crested waves, 2-dimensional sea state). In real sea states, waves do not propagate in one direction, the sea state is composed of single waves with distributed directions. The waves are short-crested. This may be accounted for with a wave spreading function, leading, together with the abovementioned energy spectra, to a two dimensional spectrum. Wave spreading is not described in the following, for a basic description it is referred to Annex B5 of IEC 61400-3 (2009).

Two wave spectra that are commonly used in OWT loads simulation, the Pierson-Moskowitz Spectrum (PM) and the wave spectrum developed during the Joint North Sea Wave Project (JONSWAP) spectrum are characterized herein (see Chakrabarti (2005) for others). For both spectra, the significant wave height H_s and a period, e.g. the mean zero-crossing period T_z are used as input parameters. H_s is defined as the mean height of the highest one third of waves in a sea-state (traditionally estimated as mean wave

height in visual observations). It is four times the standard deviation of the wave heights in a narrow-banded sea-state ($H_s = 4\sigma$). T_z is the average period between two zero-crossings with positive slope in an irregular sea-state and can be determined directly from the time series. For a given spectrum and given T_z, the peak period T_p of the spectrum, that is the period associated with the highest energy in the spectrum (the spectral peak) can be derived. T_p and T_z are interchangeable as input parameters, but the calculation of T_p from T_z and vice versa differs for the different spectra.

The PM spectrum was first described by Pierson and Moskowitz (1964) and developed based on measurements in the Atlantic Ocean during stable weather conditions. It is basically a one parameter spectrum with the mean wind speed V_w as input parameter, but it can be modified to allow for use of significant wave height H_s and mean zero crossing period T_z.

The JONSWAP spectrum is described by Hasselmann et al. (1973) and later found its way to the respective standards and guidelines. Measurements in the North Sea, in a region where sea states are usually not fully developed, led to more peaked spectra than those described by Pierson and Moskowitz. For this reason, the PM spectrum was modified with a Peak-Shape Parameter γ_j whereas the global energy content is kept constant. Equation 2.7 to Equation 2.9 give the PM ($S_{\mathrm{pm}}(f)$) and JONSWAP ($S_j(f)$) spectra and the respective parameters as provided e.g. in DNV-RP-C205 (2007).

$$S_j(f) = A_\gamma \underbrace{\frac{5}{32}\pi^{-1}H_s{}^2T_p{}^{-4}f^{-5}\exp\left(-\frac{5}{4}\left(fT_p\right)^{-4}\right)}_{S_{\mathrm{pm}}(f)}\gamma_j{}^{\exp\left(-0.5\left(\frac{f-T_p{}^{-1}}{\sigma_jT_p{}^{-1}}\right)^2\right)} \quad (2.7)$$

with

$$A_\gamma = 1 - 0.287\ln(\gamma_j) \quad (2.8)$$

and σ_j as follows:

$$\sigma_j = \sigma_a \quad \text{for} \quad f < f_p \quad \text{and} \quad \sigma_j = \sigma_b \quad \text{for} \quad f > f_p. \quad (2.9)$$

Figure 2.8 shows JONSWAP spectra for a significant wave height of $H_s = 1\,\mathrm{m}$ and a zero crossing period of $T_z = 3.5\,\mathrm{s}$ with a peak-shape parameter of $\gamma_j = 1$ (which is a PM spectrum) in blue, and a JONSWAP spectrum with $\gamma_j = 3.3$ (which is a standard value for JONSWAP spectra) in red. The same value for the zero crossing period T_z leads to slightly different peak periods T_p (and therefore associated peak frequencies f_p).

Traditionally, averaging times of at least $T_{\mathrm{sea}} = 3\,\mathrm{hrs}$ are common in the offshore oil and gas industry, as this is a good aproximation for a constant significant wave height H_s during a typical storm event. In onshore wind energy, a time series length of $T_{\mathrm{wind}} = 10\,\mathrm{min}$ is common as mentioned above. With these spectral descriptions, generic time series for simulation purposes can be generated.

To simulate the turbine lifetime of usually 20 or 25 years, long term ocean wave statistics are used (comparable to the wind speed distribution shown in Figure 2.2). A common approach to describe these statistics is by the use of wave scatter diagrams giving the probability of pairs of significant wave heights H_s and zero crossing periods T_z in a two dimensional matrix or including a wind speed bin as third dimension. Figure 2.9 shows the format of an excerpt of such a three dimensional scatter diagram as an example.

The numbers on the axes give the median of the range, i.e. a value of 3.5 in the H_s-column describes a range of $3.25\,\mathrm{m} \leq H_s \leq 3.75\,\mathrm{m}$. The last column and the last row give summarized probabilities (prob.). This is the wave data for a wind speed bin $6 \leq V_w \leq 8$ as shown in the top left field.
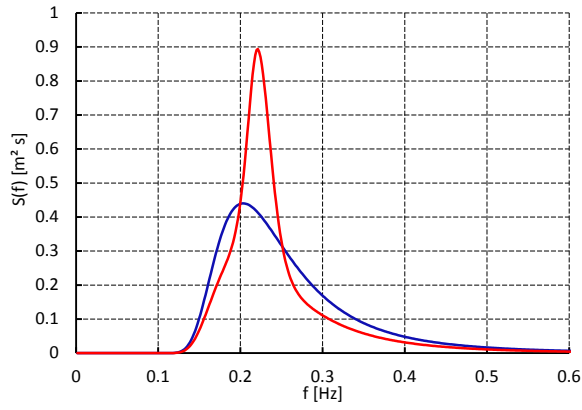
Figure 2.8: JONSWAP spectra for $H_s = 1\,\mathrm{m}$ and $T_z = 3.5\,\mathrm{s}$ for $\gamma_j = 1$ (blue) and $\gamma_j = 3.3$ (red).
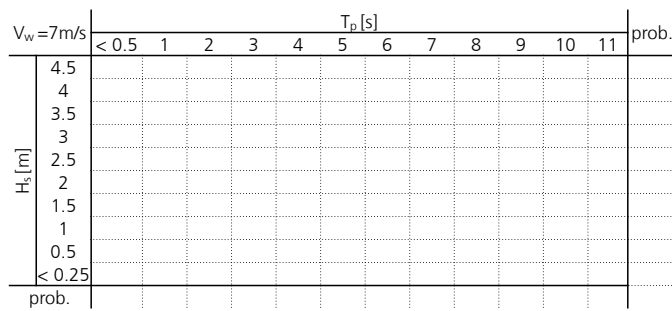
Figure 2.9: Format of an excerpt of a three dimensional wave scatter diagram (modified from Xiros (2015)).
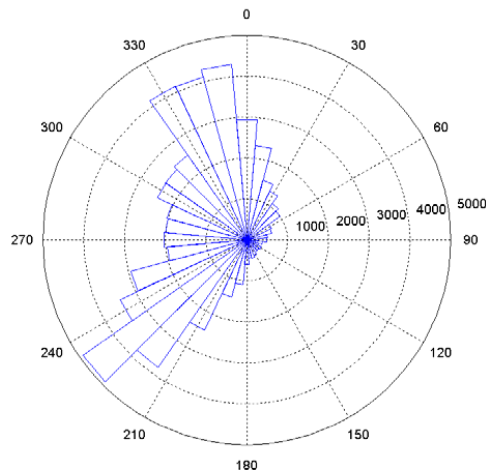
Figure 2.10: Wave rose example for a Dutch North Sea site (Figure 4 from Fischer et al. (2010)).

The long-term wave direction distribution can be visualized in wave roses, that are similar to the wind roses shown in Figure 2.3. Figure 2.10 gives such a wave rose, here with the absolute number of occurrence on the radial axes and over all sea states. It is common to generate such wave roses for all significant wave height bins separately. The long-term statistical oceanographic properties described herein are well documented based on long term measurements for many sea areas[9].

Extreme waves may lead to design-driving ultimate loads and are therefore treated separately (comparable to wind gusts, cf. Section 2.1.1). Usually, a regular 50-year wave is derived based on the respective 3-hour extreme sea-state.

The accuracy of an irregular sea state – which is more realistic than a regular wave as mentioned above – may be combined with the nonlinear nature of large waves during storm events. In this case, a highly nonlinear single wave (based on stream-function wave theory) is embedded in an irregular sea state. This is called constrained wave approach. This was described by Rainey and Camp (2007) and becomes increasingly common even if the spectrum is falsified by the properties of the extreme wave. The problem, that long sea state realizations are necessary in case the designer wants to realize one wave of a given height in a random sea state, is solved with this approach as well.

2.2   System properties of offshore wind turbines and resulting load effects

This section provides system properties of OWTs that are relevant in the loads simulation context for common three-blade, pitch-controlled, upwind turbines with a horizontal axis. For other turbine concepts and more detailed descriptions, refer to standard text books like Burton et al. (2011). A special focus is put on the different offshore support structures.

---

[9]http://www.globalwavestatisticsonline.com/; October 2, 2014.

2.2.1   Support structures and respective properties

Support structures for OWTs as shown in Figure E.1 are subdivided in foundation, substructure and tower; and theoretically all substructure, tower and foundation types might be combined. Furthermore, geometrical delimitation between tower, substructure and foundation is only reasonable to a certain extent and limited for example for full truss towers (transition between sub-structure and tower) or monopile support structures (transition between foundation and sub-structure). Not all possible combinations of tower, substructure and foundation are presented in this work. The description is limited to common and relevant types. For more details on the design of support structure types originating from the oil and gas industry, it is referred to standard textbooks like Chakrabarti (2005). An overview focusing on already realized and on planned OWT support structures including number of items and dependency of support structure type with external parameters – like the water depth for example – is given by Strach and Quiroz (2012).

Gravity bases are heavy structures, usually made of reinforced concrete, that feature hollow sections that can be filled with gravel, sand or water. This implies one of the possible advantages; certain types of gravity bases are floatable and can be towed to the site and be installed by lowering to the ground during filling. Gravity based structures usually require a certain effort when it comes to soil preparation and scour protection. Loads are transferred by pressure and shear stresses on the underlying soil layer. Resistance against horizontal loading can be increased by skirts penetrating the soil when the structure is lowered to the ground. Wave loads on gravity based structures are usually quite significant due to the large surface-piercing structural diameters (see Section 2.1.2 and Section 2.3.2 for the relations between (1) wave loading and (2) diameter and depth level). Gravity bases are widely used since the first OWTs were installed[10].

Monopiles are large steel tubes that are hammered, drilled or vibrated into the seabed. Hammering is most common, drilling is used only when necessary due to soil conditions because it is generally more expensive than hammering. Vibrating is relatively new in the offshore wind foundation context and currently under development. An important advantage of vibrating is a massive reduction of the pile driving noise. The structures are usually cylindrical, but may have conical parts. Commonly, the monopile ends approximately 10-20 m over mean sea level (MSL) where it is connected to the tower; usually by means of a grouted transition piece (TP). Vertical loads are transferred to the seabed by means of pile skin friction and tip bearing. Horizontal loads are counteracted by lateral soil resistance. This usually defines the necessary pile length, because pile tip displacement must be prevented. Figure 2.11 shows the described load bearing behavior for a monopile (left).

Monopiles are – compared to other support structures – simple structures, that can easily be mass produced, stored and transported. The structures have relatively large diameters around MSL and therefore attract relatively large wave loads. For larger monopiles in deeper waters, hydrodynamic loads become increasingly important compared to wind loads, even for large turbines. Seidel (2014a) gives an example of a monopile for 40 m of water and a 6 MW turbine for which the hydrodynamic longitudinal fatigue loading is nearly two times the wind loading. For lateral fatigue, the difference between wind and wave loading is even larger because of the reduced wind loads. In such cases, load mitigation concepts using the turbine controller become important (see Fischer (2012)). Monopiles are by far the most common OWT substructure.

Jacket[11] structures are three dimensional space frames. Most commonly, jacket sub-

---

[10] One early example is the Middelgrunden offshore wind farm in the Øresund near Copenhagen that was commissioned in 2001 (http://www.middelgrunden.dk/; October 27, 2014.).

[11] "To impress offshore people with your knowledge during a night at the bar (…) remember the difference
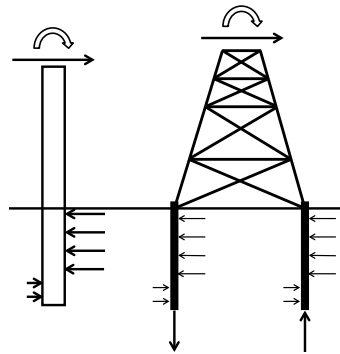
Figure 2.11: Load transfer (shear force and bending moment) to the soil for a monopile and a jacket structure.

structures are designed with four legs (chord members) welded to smaller braces connecting the legs. Mudbraces might connect the legs horizontally close to mudline. Two design solutions are common to anchor jackets to the ground: Jacket stabs or pile sleeves. In the first case, the jacket legs are placed in the pre-installed piles during the installation process. In the second case, pile sleeves, i.e. short vertical tubes, are welded at the lower ends of the jacket legs and the piles are driven through the pile sleeves and grouted. Usually jackets are combined with tubular towers.

In the Beatrice Wind Farm Demonstrator Project project[12] jackets were used for the first time in 2006. The findings that led to the realization of jacket structures in this project are described by Seidel and Gosch (2006). So far, by the end of 2014, more than 100 OWTs on jackets have been installed worldwide, mainly with Senvion turbines atop.

Loading on jackets is mainly transferred to the ground via axial loading in the jacket legs as shown in Figure 2.11 (right). The low mass combined with high stiffness and load bearing capacity of jackets is described by De Vries (2008). Due to the small water-piercing structural diameters, the wave load has a much smaller share of the total load in case of an OWT on a jacket support structure.

Apart from the four-legged jacket combined with a conical tower that became the standard for OWT jackets, full truss towers (see e.g. Muskulus (2012)), the *twisted jacket structure*[13] designed by Keystone Engineering, or three legged concepts[14] might be promising solutions. One prototype jacket with cast joints was erected so far: Senvion's Bremerhaven prototype that is described in Seidel (2007).

Tripods are – like jackets – three dimensional trusses and are basically subdivided in flat face tripods (FFTs) and centre column tripods (CCTs)[15]. Both concepts are briefly described by Seidel and Foss (2006). So far, only CCTs are realized in the offshore wind industry[16], consisting of a central column, that is supported by three inclined legs that are connected to pile sleeves. Lower braces are connecting the pile sleeves to the lower end of the central column and the pile sleeves might be interconnected by horizontal mudbraces. In case of the tripods that were realized so far, the tubular members are intercon-

---

between jackets and towers. The foundation of a tower is connected to the frame at the seafloor, a jacket's foundation is formed by piles that are driven through the legs and connected at the top." (Van der Tempel (2007), p. 39). In the offshore wind community, both possibilities would be called a jacket no matter where the piles are connected and even no matter if piles are used or not.

[12] http://sse.com/whatwedo/ourprojectsandassets/renewables/Beatrice/; October 2, 2014.

[13] http://issuu.com/lahdesigns/docs/ibgs_e-brochure/1; October 24, 2014.

[14] http://www.oceanologyinternational.com/RXUK/RXUK_OceanologyInternational/documents/marine_renewables_installation_d_craft_hochtief.pdf?v=634733678398185262; October 24, 2014.

[15] Other designs are possible and at some point jackets and tripods can no more be clearly distinguished.

[16] FFTs are not further investigated in this work, therefore CCTs are referred to as tripods in the following.

Figure 2.12: Branched support structures for a water depth of approximately 30 m. From left to right: Tripiles at construction site, jacket and tripod installed onshore (pictures: private).

nected by welded joints, which implies a significant welding effort. Like for jackets, shear forces and overturning moments are mainly transferred to the ground in terms of axial loading in the piles (see Figure 2.11). Wave loads on tripod structures are relatively high due to the large diameter central column and the large central joint (connecting the central column to the legs) which is found at the height level of the highest wave loads close to the sea surface. The first OWT on a tripod – an AREVA Wind M 5000[17] – was erected onshore in 2006. Since then, roughly 100 machines were installed offshore on tripods.

Tripiles[18] are structures consisting of three piles, that are usually hammered into the ground, extended by grouted tubular members (the extensions are connected like jacket stabs). These extensions are connected by a cross shaped box girder. The three upper tubes are welded to the cross shaped connecting joint forming a relatively complex structure. The structure combines properties of a jacket and a monopile as shown in Figure 2.11 in terms of the load transfer to the soil. Due to relatively large pile diameters close to the still water line, a tripile attracts significant wave loads. As it is horizontally compliant, this leads to large wave induced fatigue loading (Seidel (2014a)). Since the prototype erection in 2008, 80 turbines developed by BARD Engineering were installed on tripiles. Figure 2.12 shows the three aforementioned support structure types.

For details on floating wind turbine concepts and loads see Jonkman (2007), Jonkman and Cordle (2011), Jonkman and Matha (2011), Breton and Moe (2009) and Henderson and Witcher (2010). This includes spar buoys, barges, tension-leg platforms, semi-submersibles, and solutions combining aspects of these concepts. Stationkeeping of floating WTs is realized using catenary or taut mooring lines.

Many authors give overviews of currently used and planned support structure types (see e.g. De Vries et al. (2011) and Carbon Trust (2008)) and relate the usability of a type of structure to the water depth. Updated with recent developments toward larger monopiles (see e.g. Seidel (2010), Willecke and Fischer (2013) and Seidel (2014a)), this leads to approximations as shown in Table 2.1.

For different reasons, such water depth ranges can only give trends and never give fixed boundaries. There are other parameters that have a strong influence on the selection of

---

[17] http://de.areva.com/scripts/areva-wind/publigen/content/templates/show.asp?P=93&L=DE&SYNC=Y; October, 27, 2014.
[18] http://www.bard-offshore.de/; October, 27, 2014.

Table 2.1: Approximate water depth ranges for different support structure types.

Structure type	Water depth range [m]
Gravity base	0 – 25
Monopile	0 – 40
Tripod, tripile, jacket	25 – 60
Floater	60 – 1000

the substructure such as turbine size, soil conditions and wave climate. And the technical and economical feasibility ranges and the respective trends might change fast. An example is the current development of larger monopiles. During the first decade of this century, it was common to expect a boundary for the use of monopiles at a water depth of approximately 25 m and at turbine sizes of 5 MW. Even if the lack of larger pile driving hammers and the lack of production and handling capabilities for larger monopiles were given as reasons, it was expected that jackets would be economically advantageous compared to monopiles beyond these limits. This trend has changed and monopiles in water depths of 40 m in harsh North Sea Conditions with 6 MW turbines atop are expected to be built[19]. In the Gunfleet Sands 3 Demonstration Offshore Wind Farm Project[20] a 6 MW OWT was installed on a monopile in shallow water. Seidel (2014a) expects monopiles to be used in the future for 6 MW-class turbines in waters deeper than 35 m and Willecke and Fischer (2013) give design examples for turbines up to 7 MW in a water depth range of 30-50 m.

The fact, that the given water depth ranges are approximations only can be found for gravity bases as well. For the Thornton Bank project in Belgian waters for example, gravity based structures were used for 5 MW turbines in water depths of up to 27 m as described by Thomsen et al. (2007). But for the second project phase, the owner switched to jacket structures.

Even with the current trend towards large monopiles, multi-member support structures such as tripods, jackets or tripiles[21] are currently used and will have a market share in the future too. This is especially the case for jackets. The huge potential for offshore wind projects in water depths between 30 m and 60 m, especially in European coastal waters underpins this expectation.

For all types of multi-member support structures, it causes a larger effort to predict the elastic behavior of the joints and the TPs, compared to the relatively simple tubular members. This is especially the case for cast joints. Details on the modeling of joints are given in Section 2.3.7.

Even if the dynamic behavior of an OWT depends strongly on the support structure type, the following can be stated: The structure of an OWT is generally slender – i.e. it has a small structural diameter to length ratio – and heavily loaded on top. Due to the importance of cost efficiency, support structures are relatively light weight and compliant and are, therefore, prone to vibrations from the structural side. The structures are exposed to significant ocean loads from waves and currents (cf. Section 2.1.2). The first eigenfrequency of current support structures is below 0.4 Hz and therefore close to the wave frequency range. The described properties may lead to vibrating structures and couplings between the moving structure and the water-induced load.

---

[19] Monopiles are – especially by financial institutions – seen as proven technology, which is very important to realize a project. This is the case even if technical experts tend to see larger uncertainties for the monopiles due to size effects (especially in terms of hydrodynamics and dynamic soil behavior under dynamic loading).

[20] http://www.lorc.dk/offshore-wind-farms-map/gunfleet-sands-3-demonstration; October 27, 2014.

[21] Tripiles are patented as such and only used by one company (Bard Engineering) by now, therefore the future use of tripiles is closely tied to the development of this company. This makes a forecast even more difficult than for other types of structures.

2.2.2 Load effects on the rotor

For detailed descriptions of rotor aerodynamics and resulting loads it is referred to the respective literature (see e.g Hansen (2007b)). Therein, a narrowly focused overview on the aspects that are relevant in the context of this work is provided.

The rotor is a large and heavy rotating part[22] of the WT meant to produce torque from the wind based on aerodynamic lift. This results in massive aerodynamic loading of the slender and compliant blades, mainly in blade flatwise[23] direction depending on the local wind vector (cf. Section 2.1.1). Mainly due to unsteady inflow, dynamic stall effects, i.e., flow separation and reattachment behavior differing from the quasi-static phenomena, significantly changing blade loads arise. Aerodynamic tower effects, i.e. a local wind velocity dip in front of the tower, produce a dip in aerodynamic loads as a blade passes the tower leading to significant periodic excitations (so-called 3P excitation in the fixed frame). The rotor spinning through a turbulent wind field, where a blade passes a local gust several times (eddy slicing), leads to excitation of the 3P frequency (and higher harmonics) as well. Local aerodynamics in the rotating system are complex and rotational lift enhancement and stall delay can play important roles (see Schreck (2007)).

The machine is excited once per revolution (1P excitation) – for example – due to rotor imbalance (accuracy level in blade manufacture and onsite counterbalancing). Wind shear leads to periodically changing loads once per revolution for each blade, with higher wind speeds experienced when the blade points upward leading to additional loads compared to those experienced by a downward pointing blade. Yaw errors cause a comparable effect as the blade moves into the wind for half a rotation and out of the wind for the second half in these cases. The rotation itself leads to Coriolis loads, centrifugal loads, centrifugal stiffening of the blades, and gyroscopic loads during yaw and pitch movement. Gravity of the blades changes sign once per revolution leading to periodic blade bending-moment changes that are significant in amplitude and number of cycles and increasingly important for larger and heavier blades. The example of the *National Renewable Energy Laboratory (NREL) 5-MW baseline wind turbine* (see Jonkman et al. (2009)) at the *K13 Deep Water Site* (see Fischer et al. (2010)) in the Dutch North Sea with a lifetime of $T_{\mathrm{tot}} = 20\,\mathrm{years}$ and a turbine availability of $Av = 90\,\%$ (realistic values), leads to the following values for the lead-lag blade root bending-moment peak-to peak amplitude ($\Delta M_{\mathrm{root,grav.}}$) and the number of cycles (N_{20}) due to gravity.

$$\Delta M_{\mathrm{root,grav.}} = 3.6\,\mathrm{MNm} \quad N_{20} = 9.4 \cdot 10^7$$

As a comparison, the average of the flatwise blade root bending-moment (the main aerodynamic load due to rotor thrust) is $M_{\mathrm{root,thrust}} \approx 7.5\,\mathrm{MNm}$ for the same turbine at rated wind speed where the thrust is at its maximum value during power production.

2.2.3 Coupled effects, important non-linearities and summarized loads

The system properties of an OWT include the following nonlinear effects:

- Blade-pitch (and therefore aerodynamic load effects) and generator-torque are actively controlled turbine parameters. This means, that e.g. generator-torque can-

---

[22] Some authors emphasize that today's WTs are the largest rotating machinery in the world.

[23] Flatwise bending: Blade bending around the local chordline. Flapwise: Blade bending around the axis in the rotor plane, perpendicular to the undeformed blade axis. Edgewise bending: Blade bending around an axis perpendicular to the local chordline. Lead-lag bending: Blade bending around the axis perpendicular to the rotor plane, perpendicular to the undeformed blade axis (see IEC TS 61400-23 (2005).

not be described as a simple function of an input parameter like instantaneous wind speed.

- Aeroelastic effects on the rotor are of a highly nonlinear nature. During normal operation, for attached flow conditions, an instantaneously increased wind speed leads to an increase of the blade angle of attack. This, in the consequence, leads to an increase of aerodynamic lift and drag loads as long as the lift and drag curves have a positive slope which is the case until stall occurs.

  A blade vibrating in a flapwise bending mode that is moving into the wind experiences a relative wind speed that is the sum of the global wind speed, the blade rigid body movement, due to the rotor rotation, and the velocity due to the elastic deflection (blade and support structure). The instantaneous relative wind speed experienced by the blade is higher than it would be for a rigid blade and the aerodynamic loads increase due to that. An increased aerodynamic load in rotor thrust direction acts against the bending direction and decelerates the blade. When moving back, the blade is decelerated again for the same reason. This aerodynamic damping may lead to an OWT that is switched off experiencing higher support-structure fatigue load effects, than an operating turbine, because in case of the non-operating turbine, wave excitation is not reduced by aerodynamic damping (see Fischer and Kühn (2010)).

  A turbine that is operating at the angle of attack with the maximum aerodynamic lift would experience the opposite effect, a negative damping, i.e. an aerodynamic instability, because in such a case, an increased angle of attack (see above) would lead to a lift decrease and therefore to an increase of the load in the direction of the instantaneous deflection.

  The aerodynamic damping therefore depends on the pitch system (or where exactly the set point for the angle of attack lies) and the airfoils (or on the questions if the lift curves sharply peaked and if does the blade suddenly stall or not). Burton et al. (2011) give an example showing the aerodynamic damping ratio over the wind speed in the partial- and in the full load range for a pitch regulated WT. The damping is positive over the whole wind speed range, generally decreases with wind speed and has a dip at the rated wind speed where the pitch system steps in.

  Torsional flutter, i.e., the effect of periodically changing angles of attack and therefore aerodynamic loads, leads to increased motion in a combined blade mode (bending and torsion) and may lead to a significant nonlinear increase of blade load effects (see Kleinhansl et al. (2004); Hansen (2007a)).

- The dynamic properties of the system depend on the turbine status. Blade bending eigenmodes and frequencies, for example, depend on rotor speed due to effects like the aforementioned centrifugal stiffening. As a result, dynamic amplification factors change and the system's response to excitations with the same amplitude and frequency is different for different rotational speeds (see Bir and Jonkman (2007)).

- OWTs have nonlinear *components*. A grid loss, for example, leads to an abrupt torque loss. In so-called Fault Ride Through situations, turbines run through grid errors without shutting down, even if certain loads increase significantly. Short circuits lead to peaks in generator torque resulting in heavy rotor loads. The soil, in which OWTs with piled support structures are fixed, provides large uncertainties. However, it is commonly accepted that force-displacement relationships for embedded piles are not linear.

- Rotor blades are usually fiber-reinforced composite structures allowing large deflections. For large deflections, 2nd order effects in bending may become signif-
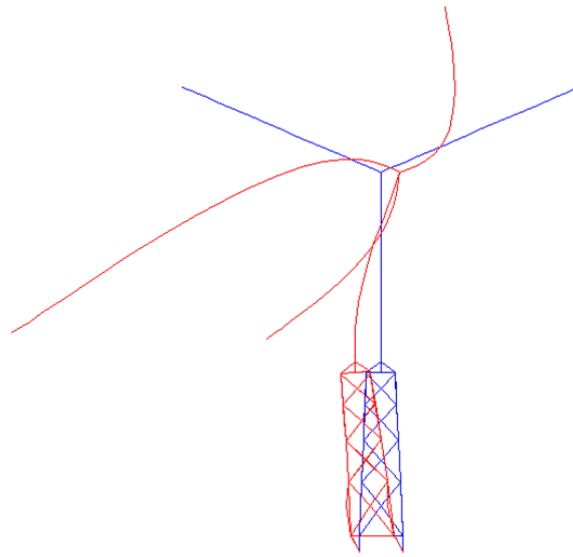
Figure 2.13: Combined vibration mode (strongly exaggerated) including blade bending and support structure modes (global bending and local bending at lowest brace).

icant leading to nonlinear force-displacement relations in blade-bending directions. This is especially relevant for large and compliant blades.

Summing up, OWTs are loaded (1) statically due to mean wind and mean currents (horizontal loads) and gravity on non-rotating components (vertical loads). Furthermore, (2) periodic loads occur due to gravity on rotating components, regular wave components, wind shear, tower disturbances and yaw errors and (3) stochastic loads result from irregular waves and turbulent wind. Finally (4) turbine start-ups and shut-downs, gusts, extreme waves and meandering wakes of neighboring turbines lead to transient loads with significant absolute values and gradients. Combined with compliant structures and the turbine lifetime, this leads, in many cases, to highly dynamic systems with fatigue loads being design driving for several components.

Support structure and blade natural frequencies, as well as the main rotor excitation frequencies, are in a comparable range for current OWTs. The proximity of eigenfrequencies of different components leads to combined structural effects that are visible in combined vibration modes including for example different component modes (shown in Figure 2.13 for the NREL 5 MW design on a jacket support structure taken from Vorpahl et al. (2011)).

Due to the importance of dynamics, the 1st global natural frequency of the system is a key design parameter for the support structure. Based on the value of this frequency and the rotor rotational speeds of the turbine, the support structures are grouped as soft-soft structures (1st natural frequency under 1P excitation), soft-stiff structures (1st natural frequency between 1P and 3P excitation) and stiff-stiff structures (1st natural frequency over 3P excitation). Usually, Campbell diagrams are used for visiualization. These diagrams show frequency over rotational speed, and the structural frequencies as well as the – rotational speed dependent – excitation frequencies are displayed. Figure 2.14 illustrates a soft-stiff design and the possible frequency range for the first systen eigenfrequency in a simplified way. The generic numbers used in the figure are realistic for a variable-speed 5 MW machine in 30 m water depth on a multi-member support structure.

The grey boxes show the 1P and 3P frequency ranges, 10 % safety margins are shown in blue, the orange box gives the possible range for the first global support structure bending frequency and the red line shows this frequency for the selected OWT. Willecke and
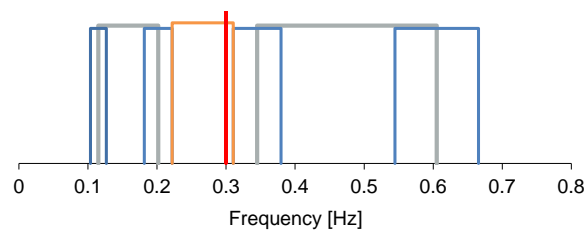
Figure 2.14: Illustration of a soft-stiff design.

Fischer (2013) show that the frequency criterium is even driving the monopile design for generic 5-6 MW OWTs in North Sea conditions (water depth range: 30-50 m).

Wind loading is much more important and complex in OWTs than for oil and gas structures. However, the magnitude of loads resulting from wind, waves and currents is highly dependent on which support structure and turbine type are used (cf. Section 2.2.1) and hydrodynamic loads may contribute 50 % to the total loading for smaller turbines on monopiles or less than 10 % to the total loading for very large turbines mounted on jacket structures. See Seidel and Foss (2006) for details on fractions of the total load resulting from wind and waves for several types of loads and selected structures. Seidel (2014a) gives the fractions of wind and wave loading contribution for different monopile and water depth examples.

2.3   Wind turbine modeling and simulation

In this section, wind turbine modeling and simulation are introduced. Section 2.3.1 firstly deals with systems, models and simulation in general and narrows down to the WT application afterwards. Section 2.3.2 then describes how OWTs are typically modeled in coupled tools. Each tool features (slightly) different levels of detail modeling the different components and a large variety of tools are available. Section 2.3.3 provides an overview on those tools that is not comprehensive. Instead, it is mainly based on experience with commonly used tools and on the international tool benchmark activities within the Wind Implementing Agreement of the International Energy Agency (IEA). These activities were realized in Task 23[24] subtask 2, also called Offshore Code Comparison Collaboration (OC3) and Task 30[25], also called Offshore Code Comparison Collaboration Continuation (OC4). Aeroelastic tools are constantly adapted to meet the rising needs of a developing offshore wind sector. Therefore, verification and validation[26] are continuously needed. Section 2.3.4 gives an overview on the respective research activities with the main example OC3. Extensive efforts are made to develop new features and / or complete tools as described in Section 2.3.5. In section 2.3.6, a description of ADCoS – the aeroelastic tool that is used in this work – in its onshore version is provided and finally, section 2.3.7 gives an overview on the possibilities of joint modeling via parametric formulae and superelements[27].

---

[24]http://www.ieawind.org/task_23.html; September 9, 2014.

[25]http://www.ieawind.org/task_30/task30_Public.html; September 9, 2014.

[26]Verification and validation are used according to the following definition in the context of this work. Validation answers the question: "Are you building the right thing?". Here this assures that the tool gives a valid approximation of the physics in the real world. This refers to comparisons of calculated results to measurement data. Verification answers the question "Are you building it right?", i.e. are the theories or formulae faultlessly implemented as intended. This is realized via code-to-code comparisons usually. This definition, including the above mentioned questions is used in Boehm (1981) for example. It is applicable here even if it is used in a different context (referring to software user needs, not to physical representation of models) in his work.

[27]This is not exactly part of the state of the art of OWT modeling only. Parametric formulae are used in offshore structure modeling in general and the substructuring approach, i.e. the use of superelements is a widely

2.3.1 From system simulation to wind turbine loads models

Systems are parts of the real world. Due to the complexity of the real world and the respective systems, understanding a system and its reactions on external input is a task that can – in many cases – only be realized taking advantage of simplification. That is, developing a model, examining its behavior and drawing conclusions concerning the behavior of the real system based on the model behavior. A model is not necessarily a numerical model, it may be an experimental set-up[28], an analytical equation on a piece of paper, or an idea. But by definition, a model is a *simplified* representation of a part of the real world. A model of a system without simplification would be a copy of the system and it would not lead to the better understanding of the real world that is intended. A model is therefore wrong by definition, but it has to represent the *relevant aspects* of the system sufficiently accurate. A clear summary of system modeling basics is given in Chapter 1 of Cellier (1991).

Technical systems are a subcategory of systems and engineering is usually dealing with technical systems. Technical systems and even the models of these systems may be (1) large, (2) complex and (3) heterogeneous. That means that the model consists of (1) *many* elements that have (2) *many interactions* and that are (3) of *different types*.

Herein, it is dealt with the technical system OWT[29] and numerical modeling and simulation. Numerical simulation in this context is the examination of the model behavior mentioned above. The simplification of the system is realized on many levels[30]. Numerical methods might be based on simplification by representing continuous (structural) systems using discrete (or finite) elements (see also Section 2.3.3). On top of that, models of different fidelity are used when it comes to an OWT design process.

Figure 2.15 shows a wind turbine system model in the center and visualizes more detailed component models – such as the detailed FE soil-pile interaction model shown in the bottom right figure. Every model is accurate enough for the specific task, i.e. represents the relevant aspects – as mentioned above – of the real system. This seems trivial, but the knowledge of the fact that every model is wrong in the strict sense and that it is only reasonable for a specific task should always be present in engineering simulation.

It could be argued if a loads model of a WT is *large*. This strongly depends on the perspective. Engineers that are usually dealing with CFD-meshes for rotor simulation are used to larger systems. From the point of view of engineers using WT control design models, a loads model possibly appears large. The size of the support structure component models used herein is described in terms of number of degrees of freedom (DOFs), that are given for each support structure model described in Chapter 4. An example indicating the *complexity* of the WT is the interaction between structural dynamic behavior and aerodynamic loading (see also Section 2.2.3). Obviously, a WT loads model is *heterogeneous*, e.g. because it contains (strongly simplified) fluid dynamics component models for wind and wave loads and structural models for support structures and blades.

In a design process, WT system models are used to simulate the turbine as a whole in the respective environment to deduce loads and load effects. These are used to design or to redesign components based on more detailed component models. A design modification of a component leads to a modified detailed component model and this in turn

---

used general FE procedure. But in this work, both approaches are investigated and applied in the context of OWT.

[28]Even if it might evoke opposition in the engineering community to follow a definition that makes experimental work a subitem of modeling and simulation.

[29]Even with the natural surrounding being part of it, the system as a whole – OWT in environment – is considered a technical system.

[30]The visual impact of an OWT in a romantic sunset is definitely part of the system, but this specific aspect will hardly be part of an engineering model.
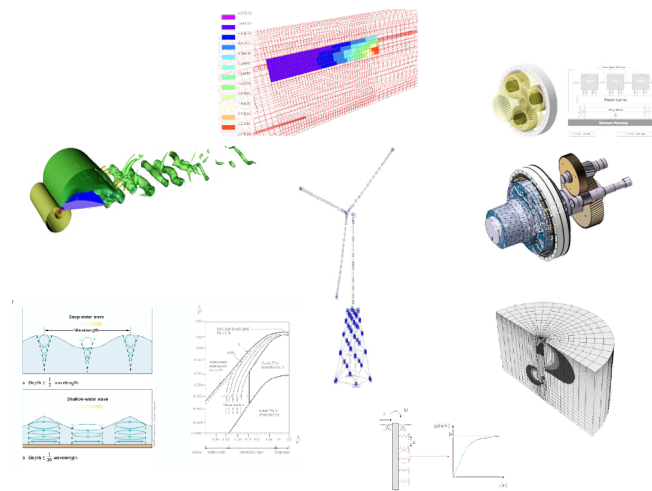
Figure 2.15: System model and component models in OWT design (Figure Source: Fraunhofer Institute for Wind Energy and Energy System Technology IWES.

leads to modifications in the simplified component model that is part of the WT system model. With this update, the simulation is redone, refined loads are deduced and used to check the proper component design.

Today's loads models feature a fidelity that is balanced based on the system's behavior and continuously rebalanced with developing WTs.

On the one hand side, the loads must be accurate enough to enable a reliable and cost effective design. The complexity of the system (cf. above), i.e. the interactions between components, leads to coupled models. The WT is actively controlled (see Section 2.2), has to withstand a stochastic environmental loading (see Section 2.1) and features fatigue driven components. This, in turn leads to a large set of load cases to cover the turbine's lifetime realistically. New features like the branched support structures that are dealt with herein must be modeled properly. Further development of certain components might lead to the necessity of new modeling features. As an example, larger and more compliant rotor blades might call for second order deflection models (see Section 2.2.3). In general, development of data processing capabilities allows for more detailed models.

On the other hand, in an iterative design process, each design loop must be realized as efficient as possible to keep the total effort on an acceptable level [31]. Aspects that are not relevant for the specific modeling purpose should not be accounted for. As an example, a Blade Element Momentum Theory (BEM) model (see Section 2.3.2) is a very simple aerodynamic model but nevertheless it can lead to sufficiently accurate results when looking into important loads simulation outputs like blade root bending moments.

---

[31]To reduce simulation effort, the possible application of simulations in the frequency domain – that is very common in the design of oil and gas structures (See e.g. Faltinsen (1990)) – is enticing. But due to the non-linearities of WT systems (see Section 2.2.3), frequency domain approaches generally cannot replace WT time domain simulation. Therefore it is not elaborated in detail on frequency domain approaches in this work. The interested reader may refer to Kühn (2001), who gives a comparison of frequency and time domain approaches (see especially Table 6.5 of the before mentioned work). Frequency domain simulation can be a reasonable complement to time domain simulation to decrease simulation effort. Savenije and Peeringa (2009) compare results from frequency domain and time domain simulations, point out differences and elaborate for example on the linearization of Morisons equation which is a premise of the applied frequency domain approach. There are differences in the results, but the authors state, that the faster frequency domain approach is valuable for design iteration in an early stage. Seidel (2014b) uses a frequency domain approach to calculate wave induced fatigue loads on a monopile and to perform efficient comparisons between different sites.

In Section 2.3.5, current developments concerning aeroelastic tools are described and for a large subset of these developments the general approach is comparable: The fidelity of one component model is increased while the residual loads model is kept the same. This is straightforward, but it is only reasonable in case (1) the computational and modeling effort is acceptable, (2) the modification has an effect on results that are (3) relevant in the investigated context (cf. above).

It is commonly accepted, that component models with different levels of detail and a loads model including the WT as a whole, i.e. integrating all the (simple) component models, are used in the design process. With the stepwise process as described above, this results in the following use case: After calculating loads with the loads model, the respective component is checked and modified. Based on that, the detailed component model is modified. This modification is then transformed to the component model that is part of the loads model. This transformation – that can for example mean to deduce beam element bending properties from a shell model of a rotor blade is usually realized manually or by means of small custom-made tools. But generally, it is possible to automate this translation at least from the more detailed to the simpler model. This promising field is not elaborated herein, it is referred to the OneWind project, the software OneWind$^{®}$ and the respective literature such as Strach et al. (2012) and Strobel et al. (2012).

Currently mainly two approaches – or hybrid forms of those – for simulation of load effects on OWTs are common in Research and Industry. In the following, these two main approaches are briefly described. It is referred to Böker (2010), Seidel et al. (2004), Seidel et al. (2005) and Kühn (2001) for details on the hybrid forms[32] [33].

Using a sequential approach, the WT is modeled and simulated with a strongly simplified support structure, e.g. clamped with associated rotational and translational stiffnesses at the tower base flange. This is usually realized by a wind turbine manufacturer. Afterwards, the turbine load effects are passed on to an offshore contractor that is responsible for the substructure and foundation design. The offshore contractor then includes the turbine load effects into the substructure and foundation model for the design of those components and hands back adapted substructure properties and loads to be included in the turbine model to the turbine manufacturer after simulation. Several loops may be realized. This approach is historically grown and has the advantage that confident information on the respective components do not need to be exchanged between turbine manufacturer and offshore contractor. However, this may lead to lacking accuracy e.g. depending on the definition of the interface and the different sub-models that are used. But with a certain effort and experience accurate results can be achieved as shown in practical industrial experience.

This work focuses on the coupled, fully-coupled or aero-hydro-servo-elastic approach that includes the OWT as a system in one numerical model. In the wind community, the respective tools are usually called aeroelastic tools. The importance of this approach, that is more straightforward and more accurate compared to those mentioned above, has continuously grown in the recent years and this development is expected to con-

---

[32] Böker describes different approaches as follows: A "superposition method", that is what is called sequential approach in this section. The "semi-integrated approach" using an equivalent monopile model when simulating an OWT on a branched structure combined with a subsequent "retrieval run" to obtain load effects on member level in the support structure. A "sequential approach", which is a further development of the "semi-integrated approach", where a superelement is used instead of the equivalent monopile that replaces the substructure as a whole. The "full coupling", where either RNA or support structure are treated as a superelement that is modified in each time step and where the system including this superelement is solved in one of the software packages involved. The "fully integrated approach" that includes the system as a whole in one tool. This is referred to as coupled approach herein and this is the approach used in ADCoS-Offshore as described in Chapter 3.

[33] Zwick et al. (2015) give a short description of sequential approaches and the respective simulation results compared to a coupled approach.
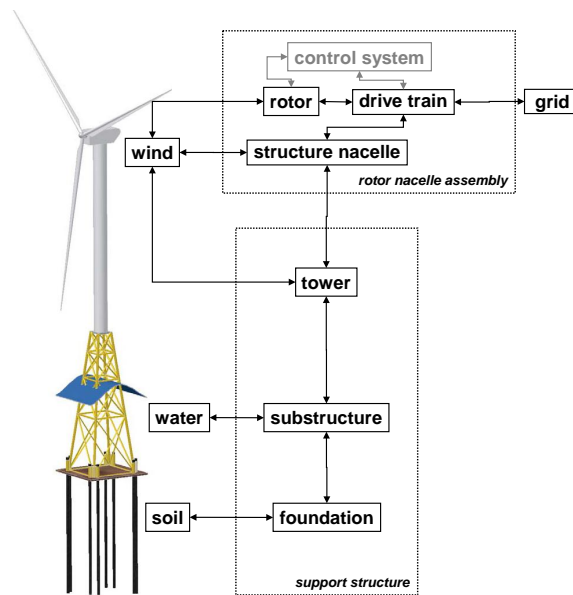
Figure 2.16: OWT model in coupled tool with boxes for components and arrows for interactions (Figure source: IWES).

tinue. Each coupled tool features a slightly different fidelity modeling the different components and a large variety of tools is available.

2.3.2   Coupled simulation using the respective tools

Figure 2.16 shows the system OWT as it is typically modeled in an aeroelastic tool on the example of a turbine on a piled jacket substructure. The modeled subsystems or components of the turbine are shown in boxes, the arrows represent interactions. The subsystems may be structured as external components (wind, water, soil and electrical grid), support structure components (tower, substructure and foundation) and RNA (rotor, drive train, nacelle structure and control system). What is common for all the tools that are used in (industrial) loads simulation is that every component is modeled in a simplified way compared to the detailed models that component designers take advantage of. This is due to the fact that computational efficiency is important, because (1) all components are modeled in one system model and (2) the number of load cases that has to be simulated in a standard loads simulation is large.

For the structural dynamic description in OWT time domain simulations, multibody simulation (MBS)-, FE- or modal-approaches are used. The basis of MBS are interconnected rigid bodies that are restricted with constraint conditions. The links between the bodies may be realized as simple kinematic joints or typically in terms of spring damper systems. Such a dynamic system can be described with a system of ordinary differential equation in time. MBS systems were originally developed for the calculation of rigid body motions and large deflections and are therefore well suited for such problems. An introduction to MBS with a focus on the interconnections between the bodies is given by Woernle (2011). Wittenburg (2008) elaborates on the mathematical background. The level of sophistication and the variety of features of modern general purpose MBS tools can be studied in the respective software documentation[34]. One important feature in the

---

[34]See for example: http://www.mscsoftware.com/product/adams; January 14, 2015.

context of WT simulation is the possibility to include flexible bodies in MBS systems.

Using the finite element method (FEM), the partial differential equations describing a structure's behavior (continuous system) are simplified to difference equations (discrete system) that can be solved numerically. Originally, the FEM was developed for structural problems, but it is based on universal principles and can therefore be applied to a large set of physical problems. Usually the equations are written in matrix form as shown in Chapter 4 with errors depending on the discretization, i.e. the size of the single element in relation to the investigated region. For an introduction including the mathematical background and heat flow examples, as well as structural examples it is referred to Ottosen and Petersson (1992), a more hands-on overview associated with the software Ansys is given by Müller and Groth (2007).

For the structural description in WT simulation, a modal condensation technique (see also Section 4.1.1) may be used to reduce the number of (FE) DOFs to a small set of (modal) DOFs to increase computational efficiency.

Even if mainly combinations of these approaches are used, tools and models may be labeled as MBS-, FE- or modal-tools (or -models) in literature. In such a case, the label reflects the approach that is used predominantly[35] in the respective tool / model. An example involving all three methods would be the use of a FE preprocessor that reduces structural rotor blade elements to modal bodies that are included in a MBS environment for time domain simulation. As shown in Section 2.3.3, different approaches are common in WT simulation but in general, all approaches allow for flexible structures and many tools somehow deal with the problem of large deflections.

Soil and foundation are usually implemented in one module. In the most simple case, the foundation under mudline is assumed to be rigid. More realistically, rotational and translational stiffnesses, i.e. a soil stiffness matrix, are applied at mudline. This stiffness matrix might be derived with a nonlinear p-y method and can be linearized depending on the load level. See e.g. API RP 2A-LRFD (1993) for details on nonlinear force displacement relationships for soil representation called p-y curves[36] that are based on the work by Reese et al. (1974). More detailed models include distributed linear springs for soil representation combined with usually linear elastic piles. From this starting point, including the p-y method directly in the aeroelastic model is the next step towards increasing model fidelity and accuracy.

The control system component usually includes the possibility to set up simple pitch controllers (PI-control) directly. For the use of more sophisticated operation and control routines, interfaces to external tools may be provided. In this context, an interface to a dynamic link library (DLL) of the type that is used in the software Bladed might be seen as a standard by now. For simulation of current WTs, a control system including at least a blade pitch and a generator torque control is common.

The drivetrain may be divided in mechanical and electrical subcomponents. MBS might be used to calculate the behavior of gear box, low speed shaft, high speed shaft and generator whereas modeling obviously highly depends on the drive train type. At least, a drive train rotational stiffness and damping summed-up in one rotational DOF and a (mechanical) generator in terms of a rotational speed-torque-relationship need to be taken into account. Power electronics are usually not defined as a separated component. If an influence from the power electronics to the residual system is intended in the simulation, this may be modeled as part of the generator definition or with a modified generator controller.

Simulation of the electrical grid, or at least of effects resulting from the grid is necessary

---

[35] It may also reflect the approach that is used basically in the opinion of the respective author.
[36] Also called Winkler springs.

in a subset of load cases. Especially grid losses leading to overspeed and a subsequent shut down of the turbine are included.

Rotor and aerodynamic loads calculation

Wind is described in three-dimensional wind vectors at discrete positions at least over the rotor swept area over time stochastically (cf. Section 2.1.1). In today's OWT simulations, Taylor's Hypothesis that relates temporal to spacial fluctuations as described by Taylor (1938) is accepted. This is underpinned by recent measurement campaigns (see Schlipf et al. (2010)). Due to that, the wind field can be described as a three-dimensional grid in space, sliding over the WT. Constant wind speeds or simple functions over time (gusts) and space (wind shear) can be simulated in current tools. The wind speeds at positions (or time steps) between the given points are interpolated. A turbulence generator to set up turbulent wind fields (see Section 2.1.1) is included. A pseudo random number generator, different stochastic seeds and a *sufficient*[37] length of the wind field – that is defined in the respective standards (see e.g. IEC 61400-3 (2009)) – are used. The wind generation may be included directly or an external tool may be coupled to the aeroelastic tool. The wind field may be generated as a whole before starting the simulation.

The rotor is modeled flexible because rotor blades are compliant structures allowing large deflections that need to be taken into account (cf. Section 2.2). Several structural-dynamic approaches are common (cf. above and Section 2.3.3).

For aerodynamic loads calculation two inputs are used: The first are lift and drag coefficients depending on the angle of attack. The lift and drag curves are usually derived from two-dimensional wind tunnel airfoil testing. The parameters are used in combination with a simple aerodynamic theory such as the BEM.

Glauert (1935) developed BEM to describe the aerodynamics of airplane propellers and Schmitz (1955) applied it to WT rotors. It became a standard in engineering aerodynamic calculation and it is described in many definitive books on WTs (see e.g. Burton et al. (2011)). The theory combines the blade-element and the momentum theory. In blade-element theory, it is assumed that the blade aerodynamics can be described with two dimensional airfoils (blade-elements) that are independent of the neighboring elements for calculation of aerodynamic forces based on local flow conditions. These forces are then integrated over the blade length. The momentum theory assumes that the loss of momentum through the rotor area is the work that is done by the air flow on the rotor. Based on this, the local flow conditions can be calculated that are the input for the loads calculation with blade-element theory. Combining both, a simple static theory to iterate the aerodynamic forces is described. To overcome its basic restrictions, BEM is extended with modifications to account for hub- and tip losses. A correction for yaw errors and the so-called turbulent wake state are included (originally described in Glauert (1935) and Glauert (1926)). During fast changes in inflow conditions, dynamic stall occurs. This nonlinear and unsteady separation and reattachment of the flow is usually accounted for by using semi-empirical corrections (see Leishman and Beddoes (1989)).

A more general theory for the description of the pressure distribution over a rotor is the potential-flow-based Generalized Dynamic Wake Theory (GDW) as described in Peters and He (1991). It includes three-dimensional and unsteady effects and the respective equations can be solved directly (non-iterative). Aerodynamics of WTs are described in more detail in Hansen (2007b) and summarized in the context of WT tool development in Moriarty and Hansen (2005). Hansen and Madsen (2011) give a detailed overview on WT aerodynamics. With the relative velocities at the rotor, aeroelastic effects (cf. Section 2.2) are included in the simulation.

---

[37]See also Section 2.3.4 for loads differences resulting from different stochastic realizations.

Support structure and hydrodynamic loads calculation

Substructure and tower are modeled flexible and several structural dynamics approaches are common (cf. above and Section 2.3.3). The models include the possibility for loads calculation on the submerged members based on Morison's representation (see Morison et al. (1950)) and a simple drag force calculation to account for wind on the structural parts above the waterline. Buoyancy loads and load effects that result from marine growth need to be taken into account. In the case of floating WTs, at least a simple mooring line model needs to be included.

Regular (cf. Section 2.1.2) and irregular (cf. Section 2.1.2) water wave kinematics are used as input in Morison's semi-empiric representation. Herein, the total load per length q_{wave}, which is in the basic formulation perpendicular to the considered cylinder, is a superposition of an inertia component q_m and a drag component q_d (here for relative kinematics between structure and fluid, horizontal water particle kinematics and a vertical tubular structure):

$$q_{\text{wave}} = \underbrace{\rho_{\text{w}}\frac{\pi}{4}D^2\ddot{u}_w + C_a\rho_{\text{w}}\frac{\pi}{4}D^2(\ddot{u}_w - \ddot{u})}_{q_m} + \underbrace{\frac{1}{2}C_d\rho_{\text{w}}D|\dot{u}_w - \dot{u}|(\dot{u}_w - \dot{u})}_{q_d} \quad (2.10)$$

The inertia term is derived assuming a potential flow problem (nonviscous, incompressible and irrotational fluid) around a cylindrical tube. It consists of two terms. The first term (Froude-Krylov Force) depends on the absolute acceleration of the fluid $\ddot{u}_w$ and the displaced water (here $\rho_{\text{w}}\frac{\pi}{4}D^2 = \rho_{\text{w}}A$, as q_{wave} is the force *per length*). Surface effects are not taken into account, there is no damping due to wave radiation for example. The second term depends on the relative acceleration between fluid and structure $\ddot{u}_w - \ddot{u}$ and the hydrodynamic added mass $C_a\rho_{\text{w}}\frac{\pi}{4}D^2$ that may be interpreted as the water mass moving with the structure through the water. The added mass coefficient C_a depends on the cross sectional shape and the local flow conditions.

Viscous drag is neglected assuming a potential flow problem but it was found to have a significant influence on the loads. Therefore, the empirical term q_d – depending on the water density ρ_{w}, the diameter of the structure perpendicular to the fluid velocity D, the square of the relative velocity $|\dot{u}_w - \dot{u}|(\dot{u}_w - \dot{u})$ and the empirical drag coefficient C_d – is included. Morison's representation leads to an inertia component with a phase shift of $90\,^\circ$ and a drag component in phase with the water surface elevation.

Morison's basic formulation is extended e.g. with terms for tangential drag along a member or using a modified inertia term to account for larger diameter members (see Mac-Camy and Fuchs (1954)). However, it is still an approach with strong restrictions and empirical coefficients that have to be derived from e.g. tank testing. See Sarpkaya (2010) for a comprehensive critique of Morison's representation that is widely used primarily due to its simplicity.

2.3.3 Capabilities of currently available aeroelastic tools in detail

Developers[38] and modeling capabilities of tools are shown in Table 2.2. The table is focused on tools for bottom mounted support structures, a comparable overview is given

---

[38]Code developers: NREL, MSC.Software (MSC), Ansys Inc. (Ansys), Texas A&M University (TAMU), American Bureau of Shipping (ABS), McDermott International Inc. (McDermott) from the USA; Endowed Chair for Wind Energy at the Institute for Aircraft Design at the Universität Stuttgart (SWE), IWES, Leibniz Universität Hannover (LUH), Institute of Mechatronics at Chemnitz University of Technology (IFM), REpower Systems SE now Senvion SE (Senvion), Aero Dynamik Consult Ingenieurgesellschaft mbH (ADC), SIMPACK AG (SIMPACK), Siemens PLM Software (PLM) from Germany; Risø National Laboratory for Sustainable Energy and Technical University of Danmark (Risø DTU), Siemens AG - Wind Power (Siemens) from Denmark; Germanischer Lloyd

in Table 6 of Robertson et al. (2014) with a focus on floating OWTs.

Aerodynamic calculations are based on BEM and GDW (cf. Section 2.3.2) including dynamic stall corrections in most of the tools[39]. A particle method – that is computationally more costly – is only implemented in GAST.

Hydrodynamic loads are calculated basically with Airy wave theory, stream-function wave theories or user defined kinematics combined with Morison's equation. Other wave theories are not detailed here and the constrained wave approach (cf. Section 2.1.2) is not included in the table. Methods based on potential flow are implemented in a few tools. Most of the tools provide interfaces to include controller-DLLs and simple algorithms are usually directly implemented. Alaska/Wind, FAST, HAWC2 and and MicroSAS-OWT provide interfaces to Matlab for controls development. Structural modeling is usually based on Multibody formulations (MBS), modal reduced systems, the FEM or combinations of those. The (catenary) mooring system of a floating WT may be simulated in some of the tools using user-defined force-displacement relationships or quasi-static catenary equations. For further information on the tools, refer to the publicly available manuals (e.g. HAWC2, Bladed, FAST), the web pages of the software developers (e.g. Ansys, Adams, SIMPACK) and publications presenting the tool development to the scientific community (e.g. Seidel et al. (2005) for Flex5-ASASNL, Böker (2010) for Flex5-Poseidon). ADCoS-Offshore is described in more detail in Chapter 3.

2.3.4 Tool verification and validation

Code-to-code verifications allow for simplification of load cases and models and, therefore, make it possible to trace back differences to the underlying sources. A code-to-code comparison may get close to a validation for newly developed codes if those are tested against tools that are widely used and were extensively validated in advance.

In contrast, during a validation process, load cases – which means in this case the influence from the physical environment – can not be simplified or partially *switched off*, even if *simple* external conditions may be selected from long term measurements for certain comparisons. Kaufer and Cheng (2014) elaborate accurately on the challenges and limitations during a validation process. Furthermore, it can hardly be analyzed to which extent a difference found between simulated and measured data is due to modeling errors, measurement errors or limitations of implemented theories. In practice, it is often a challenge to get detailed design data of a given turbine and structure due to confidentiality reasons from the manufacturer's side[40]. And especially offshore, a measurement campaign is a complex and costly task.

Summing up, verification is a reasonable first step during code development, it has technical advantages – not advantages in terms of effort only – compared to direct validation and it might even replace validation to a certain extent depending on the confidence towards the other tools in the comparison[41].

In the OC3 project, NREL's generic 5 MW WT (see Section 4.2 for a more detailed turbine

---

Garrad Hassan (GH) from the United Kingdom; Institute for Energy Technology and the Norwegian University of Life Sciences (IFE-UMB), Norwegian Marine Technology Research Institute (MARINTEK), Norwegian University of Science and Technology (NTNU), Fedem Technology AS (Fedem), SINTEF, Virtual Prototyping A/S (Virtual Prototyping) from Norway; National Technical University of Athens (NTUA), Aristotle University of Thessaloniki (AUTh) from Greece; Energy Center of the Netherlands (ECN), Knowledge Center Wind Turbine Materials and Constructions (WMC) from the Netherlands.

[39]In some of the tools, a filter causing a time delay in the equilibrium of momentum loss over the rotor and locally calculated aerodynamic loads is implemented to enhance BEM . Such dynamic wake models are also called GDW by some authors. It is not differentiated between both in the table provided here.

[40]In a large research consortium and for a state of the art turbine, this is basically impossible.

[41]It is obvious that common simulation techniques do not need to be validated for every single application.

Table 2.2: Overview of aero-hydro-servo-elastic modeling capabilities. The abbreviations used here are given in Table 2.3.

Code	Developer	Aerodynamics (aero)	Hydrodynamics (hydro)	Control (servo)	Structure (elastic)
ADAMS-Aerodyn	MSC + NREL + LUH + IWES	BEM or GDW + DSI	Airy$^{str.}$ or UD or Stream + ME	DLL or UD	MBS
ADAMS-WaveLoads	MSC + NREL + LUH	BEM or GDW + DSI	Airy$^{str.}$ or UD + ME, Airy + PF + ME	DLL or UD	Turbine: MBS, Moorings: QSCE, UDFD
ADCoS-Offshore	ADC + IWES	BEM + DSI	Airy$^{str.}$ or UD or Stream + ME	DLL or UD	FEM
alaska/Wind	IFM	BEM or GDW + DSI	Airy$^{str.}$ or UD or Stream + ME	DLL or UD or SM	FEM^P + Modal / MBS
ASHES	NTNU	BEM + DSI	Airy$^{str.}$ + ME	UD	FEM
BHawC	Risø DTU + Siemens	BEM or GDW + DSI	Airy$^{str.}$ or UD + ME	DLL or UD	MBS / FEM
Bladed	GLGH (V3.X)	BEM or GDW + DSI	Airy$^{str.}$ or UD or Stream + ME	DLL or UD	Turbine: FEM^P + Modal / MBS, Moorings: UDFD
Bladed Multibody (V4.X)	GLGH	BEM or GDW + DSI	Airy$^{str.}$ or UD or Stream + ME	DLL or UD	MBS
FAST	NREL	BEM or GDW + DSI	Airy$^{str.}$ or UD + ME, Airy + PF + ME	DLL or UD or SM	Turbine: FEM^P + Modal / MBS, Moorings: QSCE
FAST-Ansys	NREL, Ansys, ABS	BEM or GDW + DSI	Airy$^{str.}$ or UD + ME	DLL or UD or SM	FEM^P + Modal / MBS
FAST-CHARM3D	NREL, TAMU, ABS	BEM or GDW + DSI	Airy + PF + ME	DLL or UD or SM	Turbine: FEM^P + Modal / MBS, Moorings: FEM
FEDEM WindPower	Fedem	BEM or GDW + DSI	Airy$^{str.}$ or Stream + ME	DLL or UD	FEM + Modal / MBS
FLEX5	Risø DTU	BEM or GDW + DSI	Airy$^{str.}$ or UD or Stream + ME	DLL or UD	FEM^P + Modal / MBS
FLEX5-AQWA	Risø DTU + Ansys + Senvion	BEM or GDW + DSI	Airy +PF + ME	DLL or UD	Turbine: Modal / MBS, Moorings: FEM
FLEX5-ASAS(NL)	Risø DTU + Ansys + Senvion	BEM or GDW + DSI	Airy$^{str.}$ or UD or Stream + ME	DLL or UD	FEM + Modal / MBS
FLEX5-Poseidon	Risø DTU + SWE + LUH	BEM or GDW + DSI	Airy$^{str.}$ or UD or Stream + ME	DLL or UD	FEM + Modal / MBS
GAST	NTUA	BEM or 3DFW + DSI	Airy$^{str.}$ + PF or Stream + ME	DLL or UD	MBS / FEM
HAWC	Risø DTU	BEM or GDW + DSI	Airy$^{str.}$ or UD + ME	DLL or UD	FEM
HAWC2	Risø DTU	BEM or GDW + DSI	Airy$^{str.}$ or UD or Stream + ME	DLL or UD, SM	Turbine: MBS / FEM, Moorings: FEM, UDFD
MicroSAS-OWT	McDermott + NREL + AUTh	BEM or GDW + DSI	Airy or UD + ME	DLL or UD or SM	FEM^P + Modal / MBS
OneWind	IWES	BEM or GDW + DSI	Airy$^{str.}$ or UD + ME	DLL or UD	Turbine: MBS / FEM, Moorings: QSCE
Phatas-WMCFem	ECN + WMC	BEM + DSI	Airy$^{str.}$ or Stream + ME	DLL or UD	FEM
Samcef Wind Turbines	PLM	BEM + DSI or UD	Airy$^{str.}$ or Stream or UD + ME	DLL or UD	Turbine: FEM / MBS. Moorings: FEM / UDFD
Simo	MARINTEK	BEM	Airy + PF + ME	DLL	Turbine: MBS, Moorings: QSCE, MBS
SIMPACK	SIMPACK	BEM or GDW + DSI	Airy + PF + ME	DLL or UD	MBS
USFOS-vpOne	SINTEF + NTNU + Virtual Prototyping	BEM + DSI	Airy$^{str.}$ or Stream + ME	DLL or UD	FEM
3Dfloat	IFE-UMB	BEM or GDW	Airy$^{str.}$ or UD or Stream + ME	UD	Turbine: FEM, Moorings: FEM, UDFD

Table 2.3: Abbreviations used in Table 2.2.	
BEM:	Blade Element Momentum Theory
GDW:	Generalized Dynamic Wake Theory
3DFW:	Free Wake Vortex Particle Method
DSI:	Dynamic stall implementation
Airy:	Airy wave theory
Airy$^{\text{str.}}$:	Airy wave theory with stretching method(s)
Stream:	Stream-function wave theory
ME:	Morison's equation
PF:	Linear potential flow with radiation and diffraction
DLL:	External dynamic link library (DLL)
SM:	Interface to Simulink with MATLAB
UD:	User-defined subroutine
UDFD:	User-defined force-displacement relationships
QSCE:	Quasi-static catenary equations
FEM:	Finite element method
FEM$^{\text{P}}$:	Finite element method for mode preprocessing only
MBS:	Multibody simulation
Modal:	Modal reduced systems

description) on a monopile with fixed foundation, a monopile with flexible foundation, a tripod and a floating spar buoy was simulated in four subsequent phases.

The foundation model used in Phase II for the monopile is based on the commonly used p-y method (see Section 2.3.2) and three simplified linear models are derived: An apparent fixity length (AF) model (extending the monopile using a cantilever beam with adapted length and stiffness properties below mudline), a coupled springs (CS) model (defining coupled rotational and translational springs i.e., a stiffness matrix at mudline) and a more detailed, distributed springs (DS) model (extending the monopile below mudline and defining a set of linear springs distributed over the depth to represent the soil).

A set of load cases with increasing complexity was defined; load cases and model properties can be separated in the following subsets:

- Eigenanalyses of the stationary but fully flexible turbine in the absence of water in the case of the bottom-mounted structures and in still water in the case of the floating spar buoy are performed.

- All load cases in this set are run with support structure and turbine being rigid.

- The turbine is defined as a flexible onshore WT, i.e. all influences from sea water are neglected.

- A flexible offshore structure with an RNA modeled as a tower top mass or with a rigid nacelle and rotor and with disabled aerodynamic loads is simulated.

- The OWT is fully flexible and all load sources and DOFs are enabled.

In Figure 2.17, results from a load case including the fully flexible OWT on the monopile with flexible foundation under stochastic wind loading ($V_w = 11.4\,\text{m/s}$, Mann model) and irregular wave loading (Irregular Airy waves, $H_s = 6\,\text{m}$, $T_p = 10\,\text{s}$) are shown as an example. The legend on top of the figure shows the partner that submitted the results[42], the software used and the implemented foundation model. The graph shows the

---

[42]Except for the National Renewable Energy Center of Spain (CENER), the contributors are mentioned above.
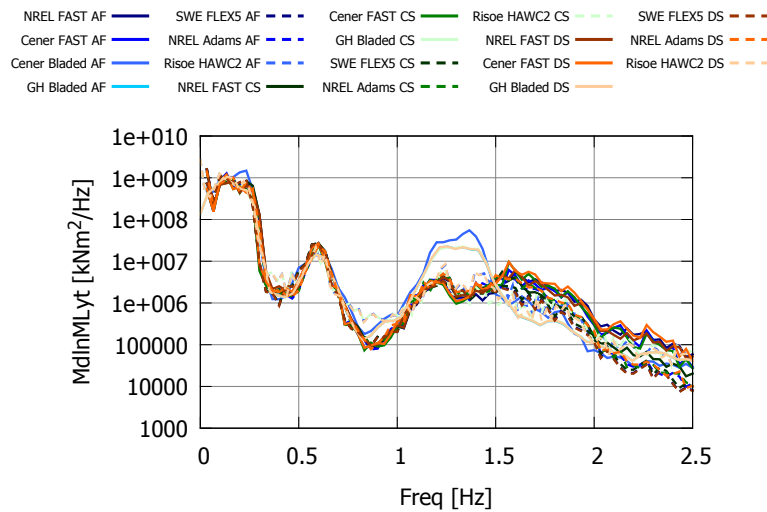
Figure 2.17: Legend for the OC3 Phase II results, Power spectra for fore-aft monopile bending moment at mudline under combined stochastic wind and wave loading. AF, CS and DS foundation models are used.

power spectra for fore-aft monopile bending moment at mudline. The results compare very well among the codes, in general, especially in the frequency range encompassing the 1st natural frequencies of the support structure, drivetrain, and blades (up to about 1.1 Hz). The differences in the higher frequency range are mainly influenced by differences among the codes in their predictions of the higher modes of the coupled system.

The comparisons, in general, agreed quite well in the project (see Vorpahl et al. (2013) for detailed results) and have resulted in a more thorough understanding of the modeling techniques and better knowledge of when various approximations are not valid. Nevertheless, small results differences remain. One finding of the project was, that user error, e.g. modeling errors occur, but that these errors can be sorted out during the comparisons. This is the case because differences in the results can be traced back to the underlying error sources usually. When modeling errors are the only remaining source of otherwise not explainable errors, they can be eliminated.

All model description and simulation results data from the OC3 project is completely available to the public[43] and can be used in the OWT simulation community without any limitations e.g. to benchmark newly developed codes[44].

The work of OC3 was continued in its follow-up project OC4 in which a jacket type support structure and a semi-submersible floater are simulated in combination with the NREL turbine. The jacket structure, that is described in more detail in Section 4.4, was selected as it was found that there were still open questions, especially concerning the simulation of local jacket dynamics. The semi-submersible is mainly of interest due to its challenging hydrodynamics. The project is described in Robertson et al. (2014).

Apart from such large projects, internal code comparisons are realized in many organizations. Examples are the verification of alaska/Wind against Bladed, FAST and FLEX5 at Chemnitz University (see Taubert et al. (2011)), verifying the in-house developed cou-

---

[43]http://oc4.collaborationhost.net/Shared%20Documents/Forms/AllItems.aspx?RootFolder=%2fShared%20Documents%2fTask%2023%20OC3&FolderCTID=&View={DC884BEA-74B2-46A4-818C-9F385564CDF6}; October 2, 2014.

[44]This was realized already by IWES during the development of the software OneWind® (formerly OnWind). Even though OneWind was not tested within OC3 over the course of the project, the software was benchmarked using the OC3 results after the OC3 project has ended.

pling between Poseidon and Flex5 against Bladed as shown in Kaufer et al. (2010) at SWE or the stepwise verification of OneWind at IWES (results not yet published). Zwick et al. (2015) continued the verification of FEDEM-wind power that was realized in OC4 against Bladed results.

Not only the system simulation, but also single aspects of the aeroelastic simulations are verified. Zwick and Muskulus (2014) elaborate on differences that result from the commonly applied stochastic wind and wave realizations. They conclude, that an error of 12-34 % or more should be expected for ultimate loads and an error of 6-12 % should be expected for fatigue loads (power production case, over all wind speeds, 1 % probability).

A detailed description of simulation tool and model validation is not the scope of this work. In this context, it is referred in Söker et al. (2006). There, the validation of design loads for WTs is briefly described and the validation of simulation tools and models is characterized as the first part of this design loads validation process. The paper refers to the respective International Electrotechnical Commission (IEC) standards. IEC 61400-13 (2005) gives detailed information on data acquisition and processing and refers directly to the (simulated) load cases described in IEC 61400-1 (2005) for comparison.

Extensive measurement campaigns were carried out during the Beatrice Wind Farm Demonstrator Project where two REpower[45] 5M WTs were installed in a water depth of 45 m on jacket type support structures. Results are detailed in Seidel and Ostermann (2009) and the challenge to record sufficient wind and wave data for design validation during the campaign is described. Another example is the Research at Alpha Ventus (RAVE) initiative[46], a research framework accompanying the construction and operation of the German Alpha Ventus test site with its six AREVA Multibrid turbines on tripod structures and six Senvion machines on jacket structures. During this effort, extensive measurement data is gathered. Results are presented by Kaufer and Cheng (2014) for example. They conclude, that the validation is successful in general and state that one main challenge in this process is the accurate representation of environmental data. That means, that it is difficult to adjust the simulated wind and wave field to the real environmental situation, because the sensors for the environmental data are limited. This limitation makes it difficult to validate results for single time series in time domain. This is realized only qualitatively. Spectral comparisons in contrast, can be realized more precisely. Component models are validated as well. As an example, in Robertson et al. (2015), wave loads on a simple cylindrical structure are validated. The results in general compare well. But results differences remain. The estimated drag coefficients, C_d for Morison's equation (cf. Section 2.3.2) for example differ between $C_{d,\,min} = 0.2$ and $C_{d,\,max} = 2$ which is obviously a large difference. It must be stated, that in this case, inertia dominated waves are investigated. This reduces the importance of the drag term simultaneously increases the difficulty to properly determine it.

During the HyWind project[47], in which the world's first large OWT on a floating structure was installed, an extensive measurement campaign was carried out.

2.3.5 Current developments of aeroelastic tool capabilities

Research needs are identified in several areas concerning coupled OWT simulation tools or – more general – in the WT design process. The developments are mainly driven by industrial developments.

- More sophisticated hydrodynamics modeling becomes important, especially for

---

[45] Now Senvion.
[46] http://rave.iwes.fraunhofer.de/rave/pages/welcome; September 09, 2014.
[47] http://www.statoil.com/en/TechnologyInnovation/NewEnergy/RenewablePowerProduction/Offshore/Hywind/Pages/HywindPuttingWindPowerToTheTest.aspx; October 2, 2014.

large monopiles and floating platforms. A research project focusing – among others – on the hydrodynamic challenges related to the use of large monopiles is currently developed at IWES[48]. Tools for floating turbines are currently being further developed. Jonkman and Cordle (2011) give an overview on the state of the art and Matha et al. (2011) elaborate on hydrodynamics of non-slender floating platforms. In this context, wave diffraction effects (du to the large structural diameter) as well as wave radiation (due to large platform motions) may become important. A possible next step towards more sophisticated models are tailored panel methods for hydrodynamic loads simulation[49]. Beyer et al. (2013) use a coupling between an aeroelastic tool and CFD for the modeling of an OWT on a spar-buoy type floater.

- Integration of ice loads simulation in coupled tools is currently realized (see e.g. Heinonen et al. (2011) and verification and validation of the respective tool is ongoing. Popko et al. (2012) give a focused summary on consideration of sea ice loading in the current standards and guidelines especially for application in the Baltic Sea and point out the respective limitation and future needs.

- The limitations of BEM are commonly understood (cf. Section 2.3.2), especially for example for load cases including large yaw errors. Several tools already have the GDW implemented, other groups are working on this topic. The next level when increasing the fidelity in WT codes are vortex methods (see e.g. Snell (2003) and Hauptmann et al. (2012)). One main aim in this context is to establish solutions between simple, fast implemented and simulated but less accurate theories like the BEM on the one hand and computational fluid dynamics including fluid-structure interaction approaches, that are very expensive in terms of modeling effort and simulation time, on the other hand. Some sophisticated codes use blade-element theory for the blade loads coupled with CFD and a momentum sink approach for the induced velocities and the wake. Nevertheless efforts are made to develop fluid structure interaction methods (CFD combined with a structural solver) to better understand WT aerodynamics and to run small numbers of critical load cases with high accuracy as well (see Corson et al. (2012) for example).

- Offshore wind parks are built and – to an even larger extent – planned as arrays of many turbines. This is mainly due to economies of scale concerning grid connection, cabling, transformer stations and maintenance. But it leads every turbine being heavily exposed to the wakes of other turbines[50], which in turn leads to a global velocity loss and higher turbulence. The detailed description of the wake, the resulting consequences on load effects (and energy yield) are current research fields, and first results from measurement campaigns imply that the simplified wake models described in standards such as IEC 61400-3 (2009) are not covering the topic sufficiently (see Schmidt et al. (2013) and Barthelmie et al. (2009)). This applies for both, loads and energy yield.

- Especially for large drivetrains, simplified modeling (cf. Section 2.3.2) leads to inaccurate load assumptions. More detailed drivetrain models may be included e.g. using interfaces as realized in Bladed for gear box models through a defined interface to external software compiled as DLLs[51]. Another approach is to extend existing MBS drivetrain libraries for global WT dynamics simulation as described

---

[48]TANDEM, **T**owards an **a**dvanced **de**sign of large **m**onopiles, to be submitted at the German Federal Ministry for Economic Affairs and Energy (BMWi).

[49]As an example, a *GH Bladed Advanced Hydro* version is currently being verified (beta version), as mentioned in Robertson et al. (2014).

[50]"We are always stating the low turbulence levels and higher wind speeds as advantages offshore. This is the case for one turbine, but no one wants to build wind farms of single turbines"; Torben Larsen, Senior Scientist of Risø DTU on wake effects at ISOPE, 2011 Maui HA, USA (orally, not word for word).

[51]http://www.gl-garradhassan.com/en/software/bladed/TurbineDefinition.php; September 27, 2011.

in Hauptmann et al. (2007) using SIMPACK[52]. In Strobel et al. (2011) it is described, that existing drivetrain libraries can be included in OneWind.

- Current research topics are the more detailed modeling of support structures and the respective investigations concerning the structural behavior. One possibility to increase the accuracy is to implement a beam model including shear effects (Timoshenko-Theory or Timoshenko-like theories) instead of a simple Euler-Bernoulli (EB) beam theory. It was shown by Nichols et al. (2009), in Vorpahl et al. (2013) and in Klausmann et al. (2012) that the use of a more sophisticated beam model leads to significant differences for certain load effects in a tripod structure[53]. Another approach is the more sophisticated joint description in coupled modeling. This is what is described in the present work. Significant work was realized by Böker (2010) in this context. Local vibration effects for jacket structures were investigated by Popko et al. (2014) using beam models.

- For design optimization of support structures, design process and tool capabilities are extended to include site- and structure-specific load mitigation systems (i.e. controls). Recent research has shown that by including specific controls into the design process and simulations of offshore support structures, cost-effective solutions can be obtained (Fischer (2012)). Specific load phenomena like extensive sideways structural vibrations as described in Fischer et al. (2012) and Tarp-Johansen et al. (2009), measurement techniques like LIDAR (Schlipf et al. (2010), Carcangiu et al. (2011)) or structural dampers (Rodríguez et al. (2011)) are in the focus.

This list is not comprehensive. Aeroelastic simulation is a task that integrates a large set of relatively different disciplines – which becomes obvious when considering the loads models including every component of a turbine in a simplified manner. Research and development needs – or potentials – arise at almost every interface between the respective component model in loads simulation and the specialist discipline dealing with this component in detail.

2.3.6 The onshore version of the aeroelastic tool ADCoS

This section briefly describes the aeroelastic tool ADCoS[54], developed by Aero Dynamik Consult Ingenieurgesellschaft mbH (ADC) in its onshore version.

The tool was developed for coupled onshore WT simulation. The structural calculation is based on a nonlinear FE approach, i.e. each time step is iterated until a convergence criterion for the dynamic force and moment equilibrium conditions is reached. Loads on the deflected structure are included. A direct time integration method is used to solve the equations of motion. Basically, a two noded standard EB beam element in 3-D space is used for the structural description of both, RNA and support structure. Bend-twist or bend-bend coupling terms are not taken into account for the support structure description. Nonlinear effects on the blades, like 2nd order pitch moments resulting from large blade deflections or torsional stiffening of the blades due to different rotational speeds are directly included in the time domain simulations. Local dynamic effects concerning

---

[52]One of the general trends in aeroelastic tool development is the extension of existing MBS tools to the needs of OWT simulation. These tools usually feature possibilities for detailed drivetrain modeling. Examples are SIMPACK (http://www.simpack.com/industrial_sectors_wind.html; February 4, 2015.) or Samcef Wind Turbines (http://www.plm.automation.siemens.com/en_us/products/lms/samtech/samcef-wind-turbines.shtml; February 4, 2015.).

[53]The use of Timoshenko-Theory in ADCoS-Offshore is mentioned in Section 2.3.6 as well.

[54]http://www.aero-dynamik.de/Home_17.html; October 31, 2014.

single members of a branched support structure are described because these members are modeled with beam elements.

A simple PI controller for the pitch system and a torque-speed look-up table for the generator may be defined in the ADCoS Graphical User Interface (GUI) directly. An interface to external controller DLLs is available to include more sophisticated pitch and or generator torque controllers. The electrical grid is not included in ADCoS models in detail, but transient effects like grid losses may be included via external DLL. The drivetrain is basically modeled as an oscillator with a torsional DOF (including torsional stiffness and damping), a gearbox ratio, two masses and time-dependent moments at both sides of the shaft, i.e. at the generator rotor and the WT rotor.

Wind is simulated as described in Section 2.3.2 in ADCoS. A turbulence generator sets up wind fields based on the Kaimal model and a rectangular grid is used. Aerodynamic loads are calculated based on look-up tables for drag, lift and moment coefficients and BEM (cf. Section 2.3.2). Hub and tip losses and a dynamic stall model as described by Leishman and Beddoes (1989) are included.

The soil structure interaction is not modeled in detail in ADCoS. Models may be clamped at mudline in manually selected DOFs, an AF model or a CS model (see Section 2.3.4 for a brief description of the models) may be used. ADCoS – in its basic onshore version – is described in more detail in Kleinhansl et al. (2004). A recent development in ADCoS is the possibility to use beams allowing for shear deflection (Timoshenko-like beam elements) instead of the basic EB beams, this is described in detail in Klausmann et al. (2012).

2.3.7 Joint modeling with parametric formulae and superelements

In this section, reasons for enhancing joint models are given and two possibilities to model joints of braced offshore structures are outlined.

In case of slender tubular members, beam elements (that are used in the basic version of ADCoS) usually lead to sufficient accuracy combined with relatively low computational effort. In a beam model the single elements are clamped at the position of the joints. Theoretically, this can lead either to an over- or to an underestimation of the stiffness of the joints and the surrounding structural elements: The effect that decreases the stiffness of a real joint – like a welded connection between a chord member with a larger diameter and a brace member with a smaller diameter – compared to what is calculated in such a simplified model, is a supplementary local flexibility. This flexibility results from the fact that the bended brace causes a local indentation in the chord. On the other hand, the representation of a welded tube to tube connection as a simple beam model leads to the use of beam elements that are longer than the real steel tubes. This is due to the fact that the beam elements in the model are connected to each other at the intersection of the centerlines of the tubes, whereas in reality, one tube is welded to the other at the radius of the tube. Longer beams with the same bending stiffness lead to larger displacements for the same loads and therefore the model becomes more flexible than the real joint. For the offshore wind application an underestimation of stiffness is usually expected in the models, therefore supplementary flexibility should be included.

The joint flexibility obviously has an influence on the eigenstates of offshore support structures and on internal forces and moments[55]. As described in De Vries (2008), the joints of OWT structures are often design drivers because of their sensitivity to fatigue loads. This means that the joint modeling in beam models of OWT support structures

---

[55]For a twelve-legged jacket structure carrying wellhead facilities exposed to wave loading, it is described in HSE OTR (2002) that a simulation model including local joint flexibility leads to a massively increased fatigue life estimation for certain structural components.
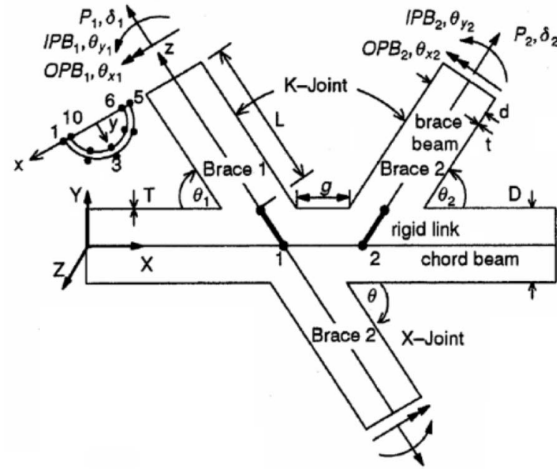
Figure 2.18: Joint geometry, loads and DOFs as given by Buitrago (Figure 1 of Buitrago and Healy (1993)).

is erroneous and the joints are critical structural elements. It is therefore a reasonable approach to enhance joint models.

Parametric formulae

On the basis of a model including clamped beams at joints there are several possibilities to enhance joint modeling. The approaches described in Fessler et al. (1986a,b) and Efthymiou (1985) are common. Romeijn et al. (1991) refer to Fessler and Efthymiou and investigated a multiplanar girder structure with different configurations of K-joints. They developed stiffness coefficients for the modeling of the joints including LJF based on joint models with clamped and free brace ends and came to the conclusion that models in which all ends are clamped except the loaded one lead to more accurate results than models with free ends.

Parametric equations were developed by Buitrago and Healy (1993) to describe LJF as follows: The total displacements are described in two portions. The first portion is the global displacement that results from the bending deformation of the joint modeled as a simple beam. The second portion results from the local effect described above and is called LJF. The LJF depends on the load direction, its value and the joint configuration. It is defined for the different joints – gapped K-joints, overlapped K-joints, Y-joints and X-joints were investigated – and for each relevant load direction separately and related to the load. The LJFs are made nondimensional with the member diameter and the modulus of elasticity.

Figure 2.18 shows Buitrago's definitions to characterize a joint. As an examples for the calculation of the LJFs, Equation 2.11 and Equation 2.12 give the influence factors from which the LJFs are calculated following Buitrago for two cases. Equation 2.11 gives the influence factor $f_{\mathrm{ax1,k}}^{\delta 1}$ for an axial load on brace one in case of a K-Joint that is loaded on both braces:

$$f_{\mathrm{ax1,k}}^{\delta 1} = 5.90\tau^{-0.114}\exp(-2.163\beta_b)\gamma^{1.869}\zeta^{0.009}\sin^{1.869}\theta_1\sin^{-0.089}\theta_2. \qquad (2.11)$$

In case of a Y-joint, that is axially loaded on its brace, the influence factor $f_{\mathrm{ax,y}}$ is

$$f_{\mathrm{ax,y}} = 5.69\tau^{-0.111}\exp(-2.251\beta_b)\gamma^{1.898}\sin^{1.769}\theta. \qquad (2.12)$$
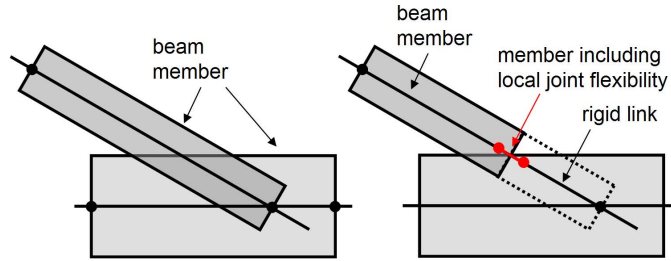
Figure 2.19: Basic FE beam model of joint (left) and modified model including local joint flexibility as described in Buitrago and Healy (1993) (right).

In the equations, the definitions based on the geometric properties given in figure 2.18

$$\tau = \frac{t_j}{T_j}, \quad \beta_b = \frac{d_j}{D_j}, \quad \gamma = \frac{D_j}{2T_j}, \quad \zeta = \frac{g_b}{D_j} \tag{2.13}$$

and the brace angles θ_i are used.

The calculation of the LJFs is performed using detailed FE analyses with shell models of the joints. Many of those analyses were carried out with different joint configurations in which the geometrical parameters given in equation 2.13 and the angles θ_i were varied systematically. With the results and the necessary interpolations, parametric formulae are derived that describe the stiffness characteristics of a wide range of joints of offshore structures in a relatively simple way.

Simulating offshore structures as beam models, those factors can be included as described in Schaumann and Böker (2008) using short flexible beam elements with the properties derived from the parametric formulae. Those flexible elements are connected at the radius and not at member centerlines using supplementary rigid links[56]. This is reasonable as the deformation occurs at the radius, where the tubes are connected physically and overcomes the problem of the beam members being longer than in reality that is described above. Figure 2.19 shows an exemplary joint as basic beam model (left) and including a flexible element and a rigid link to account for the joint flexibility (right).

Buitrago's approach can obviously be used in a simulation system that allows for the use of beam elements only and it does not increase the computational effort considerably. But it has disadvantages: The factors to include the joint flexibilities were deduced for planar joints with geometric parameters common in the oil and gas industry. Therefore those factors are – in the strict sense – only valid for those special types of joints. The factors depend on the loading conditions and the joint geometry. That means, that a K-joint for example that is loaded on one of the braces only has to be considered as a Y-joint for the LJF calculation. In a time domain simulation, the same joint may be loaded on both braces in another time step and this leads to the use of different influence factors as illustrated with Equation 2.11 and Equation 2.12. The result are different LJFs. This is impractical for many types of simulations and therefore further simplifications might be necessary. The formulae describing the joint flexibility are based on the characteristics of welded joints and therefore not suitable for other solutions, like cast joints for example.

Buitrago set up the parametric formulae based on FE calculations with shell elements in the early nineties, because it was not possible to solve the whole FE system for each single task. Increased computer performance may nowadays overcome this restriction and the FE systems might be computed directly. Buitrago's approach is included in the Det Norske Veritas (DNV) Offshore Standard on OWT support structure design (see DNV-OS-J101 (2014)).

---

[56]Buitrago and Healy (1993) and Romeijn et al. (1991) already used short rigid members too.

Superelements

A more accurate approach, which is also applicable independent of joint type, dimensions and loading, is the so-called superelement or substructuring approach that is not only used in the offshore oil and gas industry, but in several other industrial sectors like the automotive or aeronautic industry as well, and implemented in commercially available general purpose FE tools such as Ansys or Nastran[57].

The general approach is to implement detailed FE models of the respective substructures[58] of the investigated system. So-called master nodes are defined connecting the detailed model to the residual structure. In a reduction procedure the system matrices of the substructure are condensed to reduced superelement matrices with the DOFs of the master nodes. The stiffness matrix reduction – or condensation – is called static reduction and described in definitive books like Stelzmann et al. (2006) or Bathe (2001). The condensed nodes are called slave nodes or internal nodes. Two methods are common to reduce the mass matrix that are both based on static reduction. The Guyan reduction procedure (Guyan (1965)) uses the same transformation for reduction of the mass matrix as applied to the stiffness matrix. For the stiffness matrix reduction Guyan refers to Turner et al. (1956). In contrast, the component mode synthesis or Craig-Bampton method (Craig and Bampton (1968)) uses a user defined set of eigenvalues of the unreduced system to define the transformation of the mass matrix.

The combination of static reduction and Guyan's method is clearly described in Böker (2010) and summarized as follows. The static reduction starts with the matrix equation

$$\underline{\underline{K}}\,\underline{u} = \underline{F} \tag{2.14}$$

that gives the equilibrium between the external load vector $\underline{F}$ with the stiffness matrix $\underline{\underline{K}}$ times the displacement vector $\underline{u}$ (static problem). It is reorganized as

$$\begin{bmatrix} \underline{\underline{K}}_{aa} & \underline{\underline{K}}_{ac} \\ \underline{\underline{K}}_{ca} & \underline{\underline{K}}_{cc} \end{bmatrix} \cdot \begin{bmatrix} \underline{u}_a \\ \underline{u}_c \end{bmatrix} = \begin{bmatrix} \underline{F}_a \\ \underline{F}_c \end{bmatrix} \tag{2.15}$$

with the indices $\square_a$ referring to master DOFs and $\square_c$ referring to slave DOFs respectively. The objective is to eliminate the slave DOFs and to get the formulation

$$\underline{\underline{K}}_{red.}\,\underline{u}_a = \underline{F}_s \tag{2.16}$$

with the stiffness matrix $\underline{\underline{K}}_{red.}$ of the superelement[59], the respective superelement displacement vector $\underline{u}_a$ and the generalized load vector $\underline{F}_s$.

Equation 2.15 leads to

$$\underline{u}_c = \underline{\underline{K}}_{cc}^{-1} \left(\underline{F}_c - \underline{\underline{K}}_{ca}\,\underline{u}_a \right). \tag{2.17}$$

This equation is used to eliminate $\underline{u}_c$ from Equation 2.15, what results in

$$\left(\underline{\underline{K}}_{aa} - \underline{\underline{K}}_{ac}\,\underline{\underline{K}}_{cc}^{-1}\,\underline{\underline{K}}_{ca} \right) \underline{u}_a = \underline{F}_a - \underline{\underline{K}}_{ac}\,\underline{\underline{K}}_{cc}^{-1}\,\underline{F}_c. \tag{2.18}$$

With

$$\underline{\underline{K}}_{red.} = \underline{\underline{K}}_{aa} - \underline{\underline{K}}_{ac}\,\underline{\underline{K}}_{cc}^{-1}\,\underline{\underline{K}}_{ca} \tag{2.19}$$

---

[57]http://www.mscsoftware.com/; June 4, 2012.

[58]The *substructure* is the part of a structure, that is modeled in detail and then replaced by a superelement. The substructure being a part of an OWT support structure is not meant when substructures are mentioned in this Section.

[59]The denominations *reduced* stiffness matrix or *condensed* stiffness matrix may also be used.

and

$$\underline{F}_s = \underline{F}_a - \underline{\underline{K}}_{ac} \, \underline{\underline{K}}_{cc}^{-1} \, \underline{F}_c \tag{2.20}$$

This is the form of eqation 2.16.

With the transformation matrix $\underline{\underline{T}}$ defined as

$$\underline{\underline{T}} = \begin{bmatrix} \underline{\underline{I}} \\ -\underline{\underline{K}}_{cc}^{-1} \, \underline{\underline{K}}_{ca} \end{bmatrix} \tag{2.21}$$

(Including the identity matrix $\underline{\underline{I}}$ with its dimension that results from the number of DOFs of $\underline{u}_a$), $\underline{\underline{K}}_{red.}$ and $\underline{F}_s$ can in general be formulated as

$$\underline{\underline{K}}_{red.} = \underline{\underline{T}}^T \, \underline{\underline{K}} \, \underline{\underline{T}} \tag{2.22}$$

and

$$\underline{F}_s = \underline{\underline{T}}^T \, \underline{F}. \tag{2.23}$$

As described above, Guyan used the static reduction and extended it to the more general dynamic problem described with the equation of motion

$$\underline{\underline{M}} \, \ddot{\underline{u}} + \underline{\underline{C}} \, \dot{\underline{u}} + \underline{\underline{K}} \, \underline{u} = \underline{F}. \tag{2.24}$$

He proposed to use the transformation matrix $\underline{\underline{T}}$ – that is defined in Equation 2.21 for the stiffness matrix – for the mass matrix $\underline{\underline{M}}$ and the damping matrix $\underline{\underline{C}}$ also. This leads to the superelement mass matrix

$$\underline{\underline{M}}_{red.} = \underline{\underline{T}}^T \, \underline{\underline{M}} \, \underline{\underline{T}} \tag{2.25}$$

and damping matrix

$$\underline{\underline{C}}_{red.} = \underline{\underline{T}}^T \, \underline{\underline{C}} \, \underline{\underline{T}}. \tag{2.26}$$

For both reduction methods the transformation of the stiffness matrix is not an approximation, which means that the stiffness properties between the master nodes are the same for both models, the detailed FE model and the superelement.

Obviously, the reduction of the mass matrix is an approximation, because it is not possible to reduce the number of DOFs of a dynamic system and to conserve the level of accuracy at the same time. But this is not considered to be important for time domain simulation of OWTs with branched support structures because the internal mass distribution in the superelements – here the joints – has no significant influence on the overall dynamic behavior of the OWT. It is expected that in the described cases investigated in this work, even a lumped mass for a whole joint would not lead to significant errors[60].

A general problem applying a superelement approach to tubular structures when using connections between superelements and beam elements is that the master nodes are connected to the tube's walls via rigid links. The cross sections at the respective positions are stiffened and ovalization is avoided. The real deformation of a loaded joint includes an ovalization of the tubular members near the connection. This must be taken into account when deciding on the position of the master nodes, which means that the distance between master node and the position where the tubes actually intersect must have a certain length (see Dubois et al. (2013)).

The computational effort for time domain simulations is not increasing with the described method compared to simulations with the basic beam model, as the number of DOFs is approximately the same.

---

[60] Internal modes of single joints are associated with a much higher fidelity in the modeling than what is reasonable in the context of this work. This is the main reason to use the simpler Guyan reduction and not the Craig-Bampton method. (Even if the Craig-Bampton method is accepted to be more sophisticated, and to be state of the art for other modeling tasks.)

Chapter 3

Development of ADCoS-Offshore

This chapter describes the development of ADCoS-Offshore, the aeroelastic tool that is already mentioned in Table 2.2 in Section 2.3.3. ADCoS-Offshore is based on ADCoS, that is described in section 2.3.6 but includes wave loads from Ansys-ASAS[1]. Furthermore, the version of ADCoS-Offshore developed in the context of this work offers the interface to include superelement matrices in the output format of condensed matrices in Ansys. Section 3.1 describes the calculation of wave loads and the application of the superelement approach is described in Section 3.2.

In Section 2.3.3 a set of aeroelastic tools is presented. The advantage of ADCoS for the purpose of this work is, that it uses FE beams to model the support structure in its basic version. However, using the superelement feature is the salient point herein and a superelement feature could theoretically be integrated in other tools too.

3.1 ADCoS including wave loads

Loads resulting from ocean waves are calculated quasi-statically with a rigid structure in the commercially available structural FE system Ansys-ASAS, a tool widely used in the offshore oil and gas industry to simulate offshore structures. In Ansys-ASAS, hydrodynamic loads based on all common wave theories (regular linear, regular nonlinear and irregular linear waves / sea states, cf. Figure 2.7) and Morison's equation (see Section 2.3.2) as well as hydrostatic loads can be calculated. Buoyancy may be included in relation to the time-dependent water surface based on displaced water mass or based on integration of hydrostatic pressure around the submerged members. The loads calculated in Ansys-ASAS are transferred to ADCoS as nodal loads by reading a text file in the respective syntax.

Calculation of wave loads and the overall time domain simulation are separated in this simulation procedure. Therefore effects resulting from relative kinematics due to superimposed wave and structural motion cannot be described, i.e. the structural movement of the structure does not influence the wave load[2]. However, the wave loads are applied on the dynamic system what means that effects like wave loads leading to local resonances are included.

---

[1]http://www.ansys.com/; October 31, 2014.

[2]The influence of the resulting error is expected to be relatively small due to small structural displacements and velocities. Furthermore, in this study, models are compared and the inaccuracy is the same for all the models and does therefore not influence the differences in the calculated results.

3.2   Superelement approach in ADCoS-Offshore

An analysis using substructuring in ADCoS-Offshore is generally performed as described
in the following. To facilitate comprehension, different examples are shown.

- Detailed joint modeling in a general purpose FE tool like Ansys.

- Condensation of the detailed joints using e.g. Guyan reduction.

- Superelement inclusion in ADCoS-Offshore.

- Redistribution of wave loads on the superelement.

- Time domain simulation in ADCoS-Offshore.

As an example, the central joint of a tripod is modeled with shell elements in Ansys as
shown in Figure 3.1. The same figure shows the tripod as a whole (small figure on the top
left). The model consists of the shell structure (blue), the master nodes that are defined
to connect the joint to the residual tripod (black dots) and the radially arranged rigid
connections between the master nodes and the substructure (magenta colored lines be-
tween master nodes and shell structure). The master nodes are located in the centerline
of the outgoing tubular members[3].
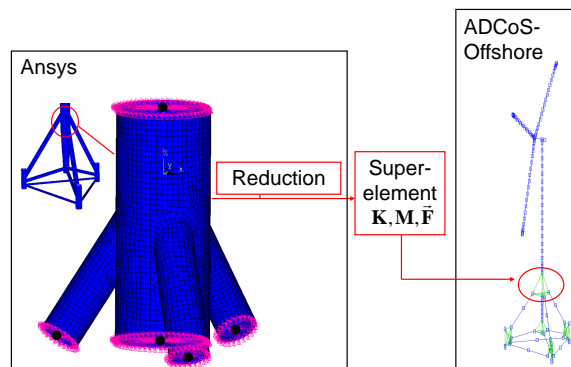
Figure 3.1: Superelement approach in ADCoS-Offshore. The central joint of a tripod is
condensed and the superelement is included in the loads model for time domain simu-
lation.

In the next step, a Guyan reduction procedure is used and the model is reduced to the
number of DOFs of the five master nodes. Six DOFs at each of the five master nodes lead
to a superelement with 30 DOFs. The superelement, in detail a stiffness matrix, a mass
matrix and a load vector for the master DOFs are included in ADCoS-Offshore in the next
step[4].

The mass matrix has the same number of DOFs as the stiffness matrix and contains the
mass of the joint, that is distributed to the master's DOFs. Those mass properties are
included in the overall system later on to describe the dynamic behavior of the system
forming the inertia term of the equation of motion in ADCoS-Offshore. The accuracy of

---

[3]A support structure model including one or more joints set up with shell elements, and beam elements
defining the residual structure is called a shell-joint model in this work.

[4]A support structure model including one or more joints set up with superelements, and beam elements
defining the residual structure is called a superelement model in this work.
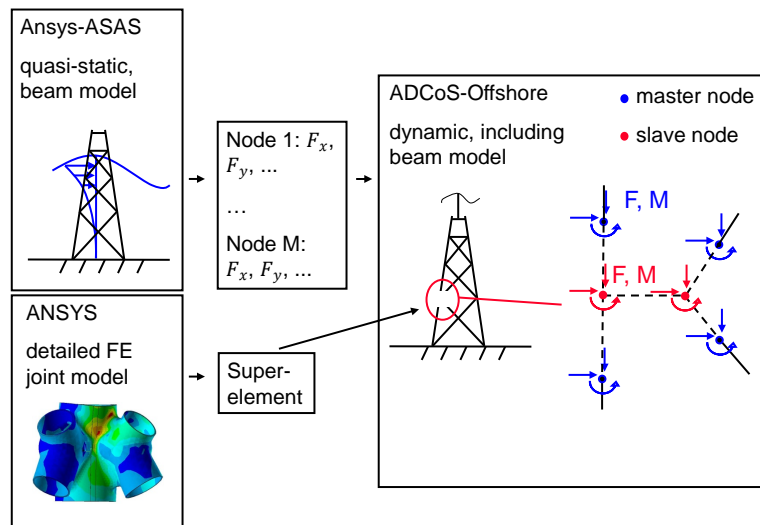
Figure 3.2: Schematic of the application of wave loads on superelements. Compared to the former model in ADCoS-Offshore, the slave nodes of the superelement – that should be loaded with forces and moments resulting from waves – are condensed (red).

the described mass representation is comparable to the one of the basic beam model that has been used before the implementation of the superelement feature.

The static load vector, that is part of the superelement, comprises the forces and moments on the master nodes resulting from the dead weight of the joint. The superelement load vector is added to the system load vector in ADCoS-Offshore. The loads resulting from dead weight at the master nodes are obviously the same as for the detailed model.

Wave loads can not be applied directly to the superelements in ADCoS-Offshore. As mentioned in Section 3.1, wave loads on the members of OWT support structures are calculated in Ansys-ASAS quasi-statically with given geometry and Morison's equation. These distributed loads are then transformed to equivalent nodal loads and included in the dynamic model afterwards.

This general approach is used with the newly developed superelement feature as well, but some modifications must be realized: In Ansys-ASAS, the outer diameter or the hydrodynamic coefficients of the beam models representing the joints, may be adapted to account for the real joint geometry, which is more complicated in the case of a cast joint for example. The result of this calculation step is a file containing the wave loads on each node for each time step to be included in the dynamic simulation. When superelements are used, this file contains loads on nodes that have been condensed and that are therefore no longer available in the dynamic model in ADCoS-Offshore. The described problem is shown in Figure 3.2 and solved via distribution of the loads on the slave nodes to the neighboring master nodes as follows:

1. The loads on the slave nodes are read from the nodal load file that has been described above, written to a slave load vector $\underline{F}_{sl}$ and deleted in the file.

2. In the model in Ansys-ASAS, all nodes at master node positions are clamped and all slave nodes are loaded statically with unit loads consecutively. This results in a total number of supplementary virtual static load cases of n times six (with n being the number of slave nodes), each with a unit load in one direction at one slave node. For each of those load cases, the reaction forces, which are not equal

    to zero only at the neighboring masters that are clamped, are written to an output file.

3. The reaction forces and moments are read from the output file from step 2 and written to a reaction force matrix $\underline{\underline{R}}$.

4. A supplementary load vector for the master nodes $\underline{F}_{ma.}$ is calculated with the reaction force matrix $\underline{\underline{R}}$ from step 3 and the slave load vector $\underline{F}_{sl.}$ that was defined in step 1. This vector $\underline{F}_{ma.}$ is written to the nodal load file. With this approach, all wave loads on the slaves are distributed to the neighboring masters by means of the reaction force matrix as a load distribution key.

5. Steps 1 and 4 are repeated for each time step. This results in a modified nodal load file for the dynamic time domain simulation.

With this approach, the global values of the wave loads remain the same as for an unmodified model. Only a distribution to other nodes has been performed. The modifications described above are verified as shown in Chapter 5.

Chapter 4

Structures, models, load cases and model tests

This chapter provides the basis for the investigations in Chapter 5 and Chapter 6. In Section 4.1, the model tests and load cases that are used in the context of this work are defined. Section 4.2 presents the RNA model[1]. Section 4.3 deals with the Tripod support structure, Section 4.4 with the Jacket. In Section 4.3 and Section 4.4, the structures are defined first in terms of physical properties and in the following the *models* of the structures are given. The sequence of the models follows the following approach: The starting point are beam models[2] as formerly used in ADCoS-Offshore simulations. In the next step, shell models[3] are developed, that serve as a reference and as the basis to develop the shell-joint models. The shell-joint models are then the basis for the superelement model[4] development.

Model development is a complex task and parts of the investigations are not shown with the same level of detail for both structures but only once. The results are then transferred. This is the case for the study on the necessity of flanges in the model that is conducted for the tripod structure for example. The jacket and tripod model development is similar and small redundancies may remain in the text to enhance readability.

Modeling errors have to be avoided. This is especially the case for the shell models, because (1) a comparison to measured data is not performed and (2) the shell models serve as a reference for verification of the other models. Based on this, discretization studies are realized carefully, further crosschecks with publicly available simulation results are conducted and all simulation results are checked for plausibility – and consistency between the models – in detail. With this approach – and with the experience that shows that modeling errors are leading to inconsistent results – it is expected, that all significant modeling errors are eliminated.

All eigenfrequency analyses presented in this chapter exclude damping and dead weight

---

[1]Usually, *physical* structures and *numerical* models are distinguished. However, this is not always consistently realized in the following, because the physical structures might not exist. The NREL turbine is not a turbine, but a loads model in the strict sense. It is often referred to as a generic turbine.

[2]A standard Euler-Bernoulli beam element is used herein. Implementation of a Timoshenko-like beam element – that takes shear deflection into account – and respective investigations on the calculated results is a separate research topic and not the scope of this work.

[3]In this work, a standard four-noded shell element, well suited for the modeling of warped shell structures with moderate thickness and six DOFs per node – such as element type Shell181 (see Ansys® Academic Research, Release 12.01, Help System, Mechanical APDL, Theory Reference, 14.181, Ansys Inc.) is used.

[4]Matrix50 elements (see Ansys® Academic Research, Release 12.01, Help System, Mechanical APDL, Theory Reference, 14.50, Ansys Inc.) are used to include the condensed matrices in the respective models.

effects. Appendix E gives the coordinate system (CS) definitions; the material properties of steel (ρ_s, E, ν, μ) are applied in all models as defined in Table A.1.

4.1   Development of model tests and load cases

In this section, the development of model tests and load cases is described. These are mass, frequency and mode shape checks, static load cases and a set of dynamic time domain load cases based on respective standards that is evaluated in terms of fatigue and extreme output parameters. This approach is selected to provide an insight in the structural behavior – depending on the respective models[5]. Dedicated extreme load cases[6] in the sense of design load cases (DLCs) as defined in standards and guidelines such as extreme waves or gusts or combinations of such environmental extremes combined with turbine faults, are not investigated. These load cases are important to evaluate extreme load levels, which is not the scope of this work. It is not expected that extreme load cases would provide a closer insight to the behavior of the models used herein compared to what can be derived from the combination of the above mentioned checks and simulations.

In model tests, the properties (system properties) of the different models are investigated. These are dead weights, natural frequencies and mode shapes. In load cases, the system's response on external loads – or load effects – are analyzed. Herein, this means static analyses and dynamic or quasi-static time domain analyses. Model tests are used during model development (Section 4.3 and Section 4.4), tool verification (Chapter 5) and results comparison (Chapter 6). Load cases are used for results comparison (Chapter 6) mainly, but for tool verification as well (Chapter 5).

4.1.1   Mass verification and eigenanalyses

The dead weight of a model gives a first idea of its plausibility and checking the dead weight is very simple. Furthermore, dead weight is an important design parameter in conceptual design [7] and even used for rough cost estimates [8].

Eigenfrequencies are simple system parameters resulting from mass and stiffness properties that determine the dynamic behavior of a system and give an idea about the plausibility of a model as well.

For a simple linear single DOF oscillator, that is described in standard textbooks such as Petersen (2010), the system is described with

$$ku + c\dot{u} + m\ddot{u} = F. \tag{4.1}$$

For an undamped system, the damping term $c\dot{u}$ becomes zero, the equation can be solved with $u = e^{i\omega t}$ and the eigenfrequency is

$$f_0 = 1/2\pi\sqrt{k/m}. \tag{4.2}$$

The response of such a system to a harmonic excitation can be described with the dynamic amplification factor V that relates the actual amplitude of the vibration to the

---

[5]Natural frequencies and mode shapes allow for a view on the dynamic behavior of a structure in a simple and fast manner, the static load case provides insight in the load transfer pattern through the branched structures and the fatigue results put a spotlight on vibration phenomena.

[6]or ultimate load cases

[7]Conceptual design is used herein as the first step in a design process consisting of conceptual design, preliminary design, optionally advanced design and final design.

[8]In this context, cost per ton of processed steel is used for support structures for example.
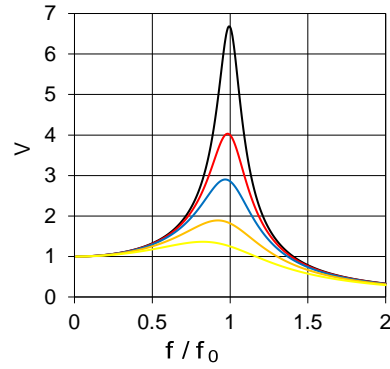
Figure 4.1: Dynamic amplification over frequency ratio for single DOF oscillator.

static deflection over the frequency ratio (f/f_0) as shown in Figure 4.1. Amplifications are shown in different colors for different damping ratios.

The one DOF oscillator is a very simple system, but it allows for direct estimates of the characteristics of more complex structural dynamic systems because certain properties are transferable. Equation 4.1 gives the basic terms in the description of dynamic systems, a stiffness term that is deflection dependent, the velocity dependent damping and acceleration dependent mass effects. The increase of natural frequencies with increasing stiffness and with decreasing masses that is expressed in Equation 4.2 is a general feature of structural dynamic systems. From Figure 4.1 it becomes directly obvious, that an excitation with a frequency in proximity to the natural frequency – or one of the natural frequencies in case of a system with many DOF – can lead to excessive vibrations depending on the system inherent damping.

Physical structural dynamics systems are in general continuous and therefore have an infinite number of DOF. For technical descriptions these systems are usually discretized and read as described in Equation 2.24. As a first step in a modal transformation, modal coordinates are defined as

$$\underline{u} = \underline{\underline{\Phi}}\, \underline{y}. \tag{4.3}$$

Herein, the deflection vector $\underline{u}$ is used and the modal matrix $\underline{\underline{\Phi}}$ that contains the eigenvectors ($\underline{\underline{\Phi}} = [\underline{\varphi}_1, \underline{\varphi}_1, \ldots \underline{\varphi}_n]$) and the vector of generalized modal coordinates $\underline{y}$ are introduced. With this approach, Equation 2.24 can be written in modal coordinates as

$$\underline{\underline{\Phi}}^T \, \underline{\underline{M}} \, \underline{\underline{\Phi}}\, \ddot{\underline{y}} + \underline{\underline{\Phi}}^T \, \underline{\underline{C}} \, \underline{\underline{\Phi}}\, \dot{\underline{y}} + \underline{\underline{\Phi}}^T \, \underline{\underline{K}} \, \underline{\underline{\Phi}}\, \underline{y} = \underline{\underline{\Phi}}^T \, \underline{F} \tag{4.4}$$

and can be simplified with the modal mass $\underline{\underline{M}}'$, the modal damping $\underline{\underline{C}}'$ and the modal stiffness $\underline{\underline{K}}'$ to

$$\underline{\underline{M}}' \, \ddot{\underline{y}} + \underline{\underline{C}}' \, \dot{\underline{y}} + \underline{\underline{K}}' \, \underline{y} = \underline{\underline{\Phi}}^T \, \underline{F}. \tag{4.5}$$

The modal matrices $\underline{\underline{K}}'$ and $\underline{\underline{M}}'$ are diagonal matrices because of the M-orthogonality of the eigenvectors. The modal matrix $\underline{\underline{C}}'$ can be approximated as a diagonal matrix. The equations are then decoupled. Finally this allows for a description of the deflections as a superposition of eigenvectors with the respective nodal coordinates:

$$\underline{u} = \sum_{i=1}^{k} \underline{\varphi}_i \, y_i. \tag{4.6}$$

Basically, the modal transformation is a coordinate transformation and a decoupling of the dynamic equations. It can be interpreted as a reformulation of a system with n DOFs

to n systems with one DOF each. It is not a reduction, because the number of DOFs and the respective accuracy are kept constant when k in Equation 4.6 is equal to the number of DOFs in the original system (Equation 2.24). The significant advantage of this approach is that even a very limited number of eigenmodes in Equation 4.6 already leads to relatively accurate results for the system's response. Usually, higher modes are damped to a larger extent (velocity dependent damping) and the excitation spectra tend to be in a lower frequency range. The lowest eigenvalues therefore already contain the largest part of the energy of the response spectrum.

In the modal analyses used here, Equation 4.5 is solved in a simplified way neglecting external loading and damping:

$$\underline{\underline{M}}' \, \ddot{y} + \underline{\underline{K}}' \, y = 0. \tag{4.7}$$

The comparison of mode shapes of different models assures that the relation between mass and stiffness is correct (in terms of distribution over the structure). When combining checks of global mass, natural frequencies and mode shapes, the correctness of mass and stiffness distribution is therefore assured.

When comparing results obtained with numerical models it is especially important to consider the respective capabilities of the models (see tower shell deformation as described in Section 4.3.3 as an example).

In the design process, eigenfrequencies of the OWT system are very important design parameters because of the dynamic properties of OWTs in general[9] and the multiple dynamic excitations that an OWT is subject to (cf. Section 2.2).

Based on the above mentioned, masses and a number of natural frequencies for a given frequency range that depends on the system are used for comparisons in the course of this work.

4.1.2 Static load case

A static load case allows for an investigation of the load bearing behavior of a structure, i.e. the load path through the structure. Generally spoken, this is also possible through an investigation of OWT time series simulations. However, in such cases, the static loads are superimposed by dynamic load effects. To get a clearer insight, it is reasonable to look at the effect of a simple static load, i.e. to solve Equation 2.14 for the respective case, before investigating more complicated load cases. To find a reasonable external load vector, normal operation of the turbine (see Section 4.2 for the turbine description) is simulated with constant wind at rated wind speed. Wind shear is not included. At rated wind speed, the rotor thrust is at its maximum within the normal operation range of the turbine. The cyclic loads at the tower top position directly under the nacelle are averaged to get the static loading. Table 4.1 shows the resulting loads in six DOFs to be applied at the tower top node in global coordinates.

4.1.3 Time domain load case set

Mainly due to the characteristics of the environmental loading (cf. Section 2.1) and the system properties (cf. Section 2.2), fatigue load effects play an important role in certi-

---

[9]The importance of the eigenfrequencies – especially the frequencies associated with the first global bending modes of the structure – could be raised as subject of a separate debate: On the one hand, frequency differences of less than 1 % can lead to a completely new loads simulation in a certification process (personal experience). On the other hand, it takes many revisions in code comparison projects with experienced scientists and state of the art tools involved to end up with frequency differences of a few percent even with simplified boundary conditions (cf. Vorpahl et al. (2013)).

Table 4.1: Static loads at tower top position.

Component	Value [kN] [kNm]
F_x	740
F_y	-1.5
F_z	-3500
M_x	4220
M_y	185
M_z	-43

fication and design of OWTs. Both are based on extensive loads simulations in the time domain. Respective standards, like the widely used IEC-61400-3 (see IEC 61400-3 (2009)), contain load case tables featuring a set of DLCs.

The dynamic equation that is to be solved is given with Equation 2.24. Herein, the displacement dependent stiffness term (stiffness matrix $\underline{\underline{K}}$ times displacement vector $\underline{u}$), the velocity dependent damping term (damping matrix $\underline{\underline{C}}$ times the velocity vector $\underline{\dot{u}}$) and the acceleration dependent inertia term (mass matrix $\underline{\underline{M}}$ times acceleration vector $\underline{\ddot{u}}$) are balanced with the external load vector $\underline{F}$. Equation 2.24 can be formulated in a way that clarifies the components of the matrices that are included in the calculation in ADCoS (cf. Section 2.3.6)[10].

$$\underbrace{\left(\underline{\underline{K}}_k + \underline{\underline{K}}_z + \underline{\underline{K}}_h\right)}_{\underline{\underline{K}}} \underline{u} + \underbrace{\left(\underline{\underline{C}}_c + \underline{\underline{C}}_g\right)}_{\underline{\underline{C}}} \underline{\dot{u}} + \underline{\underline{M}}\,\underline{\ddot{u}} = \underline{F}. \tag{4.8}$$

In this equation, the stiffness matrix is expressed as the sum of a centrifugal stiffness matrix $\underline{\underline{K}}_z$ that accounts for the centrifugal stiffening of the blades of the rotating rotor, an acceleration stiffness matrix $\underline{\underline{K}}_h$, that becomes zero for constant rotational speed and a structural stiffness matrix that comprises the structural stiffness terms. The damping matrix $\underline{\underline{C}}$ is split up in a matrix accounting for virtual gyroscopic damping terms ($\underline{\underline{C}}_g$) and a structural damping matrix $\underline{\underline{C}}_c$.

Following the example of IEC-61400-3, 34 DLCs are defined to allow for simulation of the turbine's lifetime. These DLCs are further divided in single load cases (resulting in single time domain simulations, see also the beginning of this chapter for the definition of load case in the context of this work). This usually results in few thousands of load cases covering the whole lifetime of the turbine for a given site to accurately describe fatigue and ultimate limit states. For example, the distribution of wind speeds and turbulence (cf. Section 2.1.1), probabilities of sea states and their directional distribution (cf. Section 2.1.2), operational events like start and stop procedures, errors like grid losses or pitch system failures and different stochastic realizations are accounted for. For detailed descriptions of load case sets it is referred to the respective standards.

Herein, a load case set is defined as follows. The IEC load case definitions are used as a starting point. Furthermore, the publicly available design basis defined in work package 4: Offshore foundations and support structures of the Upwind project[11] funded under the European Unions Sixth Framework Programme (cf. Fischer et al. (2010)), is used for the necessary site description. This document provides realistic data for a northern European offshore site.

Only DLC 1.2 (normal operation of the turbine) is selected. This DLC covers a large share of the turbine's lifetime. It does not cover the time when the turbine is deactivated, i.e. idling in the operational wind speed range due to errors; these cases are relatively rare.

---

[10]Kleinhansl et al. (2004) use this formulation that is given in Argyris and Mlejnek (1997).
[11]http://www.upwind.eu/default.aspx; March 18, 2014.

Availabilities around Av=90-95 % are realistic. Furthermore it does not cover the situation of an idling or parked turbine which is relatively rare as well because of the small probabilities of very low and very high wind speeds.

For further simplification, wind speed bins with higher wind speeds (10 min average) than $V_w = 24\,\text{m/s}$ are not taken into account. The probability of occurrence per year for these wind speeds is only $O_{\text{year}} = 73\,\text{hrs.}/\text{year}$, therefore the respective situations are neglected even if the cut-out wind speed of a typical OWT is higher. Using a standard bin size of $\Delta b= 2\,\text{m/s}$, this leads to eleven wind speed bins. Table 4.2 provides the average wind speed V_w, the turbulence intensity T_i, the significant wave height H_s, the peak period of the PM spectrum T_p and the summed occurrence of this wind and wave combination O_{year}. This diagram is a modified fragment of the lumped scatter diagram developed in the Upwind Project given by Fischer et al. (2010).

Table 4.2: Modified lumped scatter diagram (see Fischer et al. (2010)).

V_w [m/s]	T_i [%]	H_s [m]	T_p [s]	O_{year} [h]
4	0.2042	1.10	5.88	780.6
6	0.175	1.18	5.76	1230.6
8	0.1604	1.31	5.67	1219.7
10	0.1517	1.48	5.74	1264.9
12	0.1458	1.70	5.88	1121.8
14	0.1417	1.91	6.07	881.3
16	0.1385	2.19	6.37	661.7
18	0.1361	2.47	6.71	427.3
20	0.1342	2.76	6.99	276.1
22	0.1326	3.09	7.40	168.6
24	0.1313	3.42	7.80	85.6

Further reduction of the number of load cases is realized by reducing the directional wind and wave distribution and only taking one wave direction into account instead of the respective wave roses. The wave direction is along the mean wind direction ($\alpha = 0°$). Yaw errors are accounted for in a simplified manner making use of the angle β between wind direction and horizontal rotor axis direction and three different wind and wave seeds, i.e. statistical realizations, are used in each wind speed bin. The simulation time ($600\,\text{s}$) is a standard value. In Table 4.3 the described simulation settings are shown.

Table 4.3: Simulations settings for each wind speed bin. Angles of zero degrees describe the mean wind and wave direction.

Subcase no. [-]	Wind dir. β [°]	Wind seed [-]	Wave dir. α [°]	Wave seed [-]	Sim. time [s]
1	-8	1	0	1	600
2	0	2	0	2	600
3	8	3	0	3	600

In all wind definitions, a Kaimal wind spectrum and a logarithmic wind shear profile (cf. Section 2.1.1) are used. Irregular sea states are simulated with superimposed Airy wavelets (cf. Section 2.1.2).

The load cases are evaluated in terms of extreme- and fatigue output parameters, which is a common approach. In the current Germanischer Lloyd (GL) guideline for example, DLC 1.1 (the equivalent to the normal operation DLC described herein) is defined as a fatigue and ultimate load case (see GL Offshore (2012), Table 4.4.1). The extreme values are extracted from the results without applying safety factors. For fatigue analyses, mainly DELs are used. The DEL are calculated with a reference number of cycles of

$N_{\mathrm{ref}} = 2 \cdot 10^8$. All loads are extrapolated to one year of operation with the occurrences given in Table 4.2.

The approach used herein leads to a set of 33 load cases and is a good compromise between effort (load case definitions, simulation set-up, computational time) and a *realistic* load case set, i.e. a load case set that is close to what is used in standard OWT loads simulation. See also Vorpahl and Reuter (2011) for the definition of the load case set which is used for all time domain simulations in this work. In all time domain results comparisons, the same stochastic realizations of wind and waves are used.

4.2 Rotor nacelle assembly

The NREL 5 MW turbine that was developed for the purpose of code verification is a representative model of a three-bladed variable-speed 5 MW upwind turbine with collective pitch control. The design is based on available information from turbine manufacturers with an emphasis on the REpower[12] 5M machine. Detailed data is provided by research projects – with a focus on the Dutch Offshore Wind Energy Converter (DOWEC) project – where design data is not available due to confidentiality reasons. During the turbine model development, the best available and the most representative data was combined. The turbine definition includes aerodynamic and structural data as well as the definition of a control-system. Table 4.4 gives basic properties of the turbine.

Table 4.4: Basic parameters of the generic NREL 5 MW turbine as defined by Jonkman et al. (2009).

Number of blades:	3
Orientation:	Upwind
Control:	Pitch, variable speed
Rated power:	5 MW
Rotor diameter:	126 m
Mass RNA:	350 t
Rated rotor speed:	12.1 rpm
Rated wind speed:	11.4 m/s
Gearbox ratio:	97:1

This turbine model is widely used in the scientific community which underlines its suitability for the type of study realized herein. An example is the use as a basis for the reference turbine in the Upwind project. Furthermore, several modifications of the baseline model - like a downscaled turbine (Tarp-Johansen et al. (2009)), a two-bladed version (Larsen et al. (2007)) or a turbine with modified controller (Jonkman and Matha (2009)) – are defined for different purposes in different organisations. The model is described in detail in Jonkman et al. (2009).

4.3 Tripod support structure

The tripod support structure models that are used in this study are based on the definition – consisting of tripod substructure and tubular tower – by GL Garrad Hassan for OC3. See also Vorpahl et al. (2010) and Vorpahl and Reuter (2011) for tripod modeling. Section 4.3.1 gives the structural properties, i.e. the physical properties of the tripod

---

[12]Now Senvion
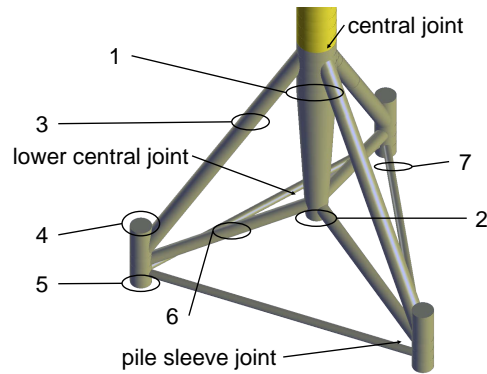
Figure 4.2: Tripod substructure and positions where cross sectional properties are provided (cf. Table 4.5).

that have to be implemented in the numerical models. The following sections describe the models that are used in this study: Section 4.3.2 introduces the development of the beam model. Subsequently, the support structure is entirely built with shell elements, as shown in Section 4.3.3 to provide a reference model. Based on this, a shell-joint model is deduced (Section 4.3.4), which is the basis for the superelement model described in Section 4.3.5.

4.3.1   Structural properties and general modeling assumptions

The tripod substructure is designed for a water depth of 45 m and it is extended by a tower featuring a decreasing diameter D and wall thickness t with increasing height. The elevation of the tower top from the seabed is 132.6 m, leading to a realistic hub height for a turbine of this size.

The tripod substructure is shown in Figure 4.2. Cross sectional properties for the positions shown in this figure and described in the following are given in Table 4.5. Position

Table 4.5: Cross sectional properties D and t for positions shown in Figure 4.2.

Position	D [m]	t [mm]	Comment
1	5.7	50	Central column upper part
2	3.142	50	Central column lowest end
3	2.475	35	Leg
4	3.15	45	Pile sleeve upper part
5	3.15	35	Pile sleeve lower part
6	1.875	25	Brace
7	1.2	25	Mudbrace

one (under the central joint) lies 10 m under MSL, i.e. 35 m over mudline. From this position, the tripod central column continues up to 10 m over MSL with constant diameter D and wall thickness t. The central column is conical between position one and two, its lower end (and the lower end of the lower central joint). All remaining parts have constant diameters. The legs (position three) are attached to the central column composing the central joint and to the pile sleeves (position four and five), forming the pile sleeve joints. Braces (position six) connect the pile sleeves and the central column, and mudbraces (position seven) connect each pile sleeve with the two remaining pile sleeves. These have a constant outer diameter D but a stepped thickness t, the lower parts - from
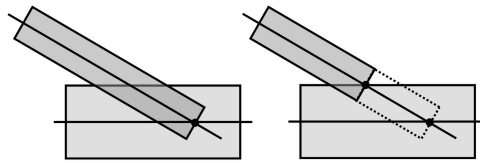
Figure 4.3: Simplified joint model with a supplementary element (dotted line) excluded from the wave, buoyancy and dead weight calculation (right) compared to a basic model (left).

mudline up to the intersection with the mudbraces - are weaker than the residual parts of the pile sleeves. The piles are not defined because the tripod is supposed to be cantilevered at each pile sleeve at mudline in all models. Based on the global CS, the legs are numbered for the use in this work. The first leg is pointing in negative direction along the x-axis (upwind leg). Leg two is the downwind leg on the left when looking downwind ($y > 0$), the remaining leg three consequently lies downwind right. The central column and the pile sleeves of the tripod are free flooded, legs and braces are not. It is neither accounted for marine growth nor for any appurtenances (secondary steel). Appendix C gives nodes (see Table C.1) and node connectivities (see Table C.2) of the tripod. Furthermore, the tower is defined in terms of cross sectional properties in this appendix (see Table C.3).

4.3.2 Beam model

The beam model described in this section is used for later comparison with higher fidelity models pointing out the restrictions of beam models for tripod modeling in general. Therefore, effort during modeling must be made to make sure that the model is suitable and all restrictions are due to the type of model (beams) and not the modeling itself (e.g. insufficient discretization).

Basically, at positions where more than two beam elements are jointed, the connecting node lies at the intersection point of the centerlines of the elements. Figure 4.3 shows the described simplification.

To quantify the resulting error, results from a basic model (see Figure 4.3 left) are compared to those of a modified model in which all joints are modeled as shown in Figure 4.3 on the right. The following Figure (Figure 4.4) shows the global force in wave direction on the tripod structure for a basic wave load case over one wave period as an example. In this case, the WT is modeled as a rigid structure, wind loads are disabled and a streamfunction wave (cf. Section 2.1.2 and Dean (1965)) with a wave height of $H_{\mathrm{sf}} = 8\,\mathrm{m}$ and a period of $T_{\mathrm{sf}} = 10\,\mathrm{s}$ is applied.

The difference of the extremal values in this Figure is 9 % based on the value resulting from the modified model. The static buoyancy force related to MSL between the basic model and the modified model can easily be calculated analytically. The difference is 7 % based on the value resulting from the modified model. Doubling of masses is avoided as the mass of the small supplementary members as shown in Figure 4.3 (dotted line) is set close to zero (reduced density). The resulting difference is not quantified herein.

Based on the above mentioned results, the model including small elements to avoid doubled parts is selected for all further comparisons. It is obvious that the importance of the described effects directly depends on the type of structure. For buoyancy it depends namely on the doubled submerged volumes relative to the total submerged volume. For wave load calculation, the error is a function of the doubled outer area and of the vertical position of this area. As the wave loads are most important near the water surface, a big
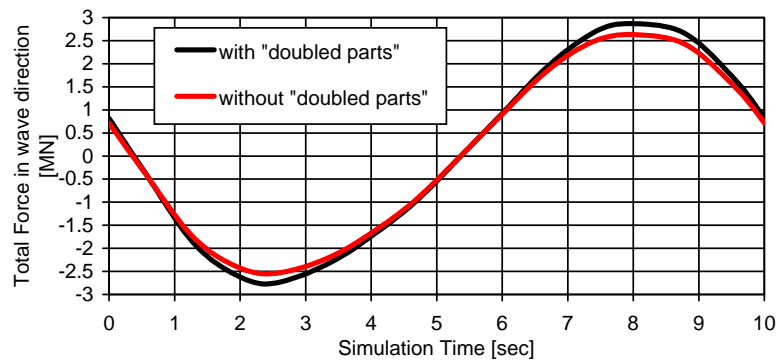
Figure 4.4: Global wave force on tripod structure in wave direction.
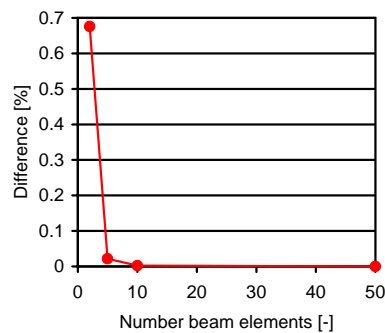
Figure 4.5: 1st structural eigenfrequency of tripod mudbrace for different discretizations with respect to a model with 100 elements.

submerged joint near the water surface causes the largest error. This is a simplified approach as the real doubled volume (buoyancy), surface (wave load calculation) and steel mass (dead weight and dynamics) are still estimated, however, the model is significantly improved by using the supplementary members.

As this study intends to take a closer look at the local dynamic behavior of the structure, an influence of the discretisation of the tripod tubes has to be avoided. In a first step toward finer discretisation of the model, the representation of the mudbraces would be refined because the mudbrace models have the highest length to diameter ratio for one single FE beam element.

The eigenfrequency associated with the first bending mode of the mudbrace is calculated for different models. Figure 4.5 shows the differences of those eigenfrequencies for models with a number of single elements between two and 50 for the mudbrace. The results are related to a model with 100 elements.

As expected, the differences decrease with increasing number of elements. However, even for the simplest model the difference to the most detailed model – which can serve as a reference due to the clear convergence – is clearly under 1 %. As the computational effort for the time domain simulations should be kept in a reasonable scale, such small errors are accepted and the model is not refined.

The model discretization for wave load calculation near the water surface is investigated briefly. For a structural element near MSL for example, a wave load is applied when the wave crest passes and no load – as there is no water – is applied when the wave trough passes the structure. The highest wave loads are applied near the water surface. There

are different possibilities how to treat this in a numerical tool. For reasons of simplicity, several WT design tools consider the members to be either fully loaded or not loaded at all. With such an approach, a wave leads to a stepped load for a coarsely divided structure which is not a realistic result. This problem, that is described in more detail by Nichols et al. (2009) can be resolved with a finer discretization of the model.

In contrast to this, the wave loads are calculated at several positions along one structural element and interpolated to a load per unit length in this work. This is the approach implemented in ASAS WAVE and described in detail in the respective software documentation (ASAS User Manual (2006)). Afterwards, the loads are applied in terms of equivalent nodal loads to the structural model. Therefore, the wave load calculation is independent of the structural discretization. The correct application was verified via comparison of results obtained with models with a coarse discretization and models with a very fine discretization. These models lead to identical results for the wave loads as expected.

With this approach wave loads can be simulated in as much detail as necessary whereas the structural discretization is not more detailed than necessary for simulation of the structural response to the loads. This leads to a reduced calculation effort for time domain simulations with accurate wave load prediction.

The number of DOFs of the resulting beam model is n_{beam}=630 DOFs. It is as realistic as achievable with standard beam elements and reasonable effort. Therefore, it is suitable to investigate the differences between beam models and more sophisticated structural models.

4.3.3 Shell model

A shell model is defined as a reference model. The first five eigenfrequencies and modes of the structure are shown in table 4.6 for a basic shell model.

Table 4.6: First five eigenfrequencies and mode shape descriptions for the tripod shell model.

Frequency [Hz]	Description
0.622	1st global bending
0.623	1st global bending
2.135	1st global torsion
2.263	Mainly tower shell deformation
2.263	Mainly tower shell deformation

Two views (side view and inclined bottom view) of the 4th mode shape described in Table 4.6 are visualized in Figure 4.6. It is directly visible that this mode shape is not representable using beam models for the tower description and that the frequency value (Table 4.6) is in a range that is significant for global dynamic WT analyses. Both is true for the 5th and the 6th mode shape as well (not shown here). Even with a RNA included it is not expected that these frequencies are shifted a lot, as the mode shapes are mainly concerning the tower shell. The mode shapes shown here are not realistic for the following reason: In reality or in more detailed models, these shapes are prevented by the flanges being part of a tubular tower of this size. The tower model is based on the model description for the OC3 project. In this project, aeroelastic tools are benchmarked that use tower models set up with beam elements in the most sophisticated models available. Therefore it was not necessary (for this project) to define the tower model in great detail. Using beam models, the tower definition as it is described in Table C.3 in Appendix C is completely sufficient, the tower shell deformation modes shown here and the respective
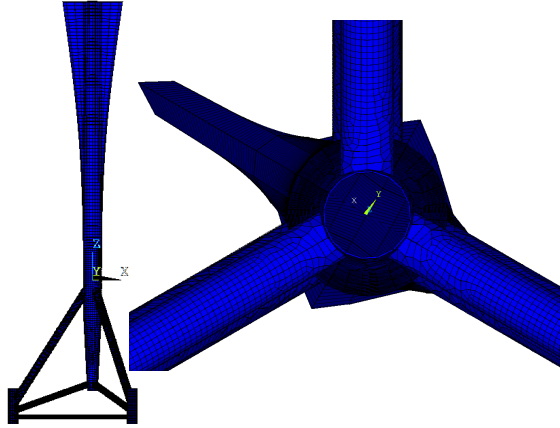
Figure 4.6: 4th shell tripod mode shape that mainly is a tower shell deformation at a frequency of $f_4 = 2.263\,\mathrm{Hz}$.

frequencies do not show up, the global OWT model leads to realistic eigenfrequencies.

In this work, a shell model of the structure is used and therefore, a realistic tower model is set up in a first step. A suitable discretization of this tower model is found in a brief parameter study refining the mesh in each step until convergence of the dead weight and all frequencies under a limit frequency of $f_l = 5\,\mathrm{Hz}$ is found (results not shown here). With the respective discretization, a model of the tower including three flanges (base, middle, top) is set up using values for the flange wall thickness and the flange height based on experience with OWT towers of this size. The resulting geometrical flange parameters are given in Table B.1 of Appendix C. At the tower top level, the DOFs of all nodes are rigidly connected because the yaw bearing is assumed to be very stiff compared to the tower shell.

Two requirements have to be fulfilled by the shell model: It has to be realistic referring to the model fidelity of a loads model and it has to allow for comparisons with the available simulation results from the OC3 project. The described flanges lead to a more realistic shell model. But the flange mass increases the total mass of the structure. To fulfil the second requirement, the flange masses are reduced to end up with the global dead weight of the support structure as defined for the OC3 project. This is realized with a respective decrease of the flanges' material densities ρ_{fl} as given in Table C.3. The dead weight difference of this modified model compared to a model including a realistic flange density is $\Delta m = 2.7\,\%$ of the tower mass ($\approx 8.7\,\mathrm{tons}$). The maximum difference of a tower eigenfrequency under a limit frequency of $f_l = 5\,\mathrm{Hz}$ due to this modification is $\Delta f_{max} = 0.5\,\%$. This means that the model is still a well justified tower model and therefore the model including flanges with reduced density is used in the following.

The lowest tower frequency calculated with this model including flanges which is related to a mode that can not be represented in a beam model is shown in Figure 4.7, the respective frequency lies at $f_{low} = 3.3\,\mathrm{Hz}$.

This means, that higher natural frequencies and their respective mode shapes in models that do not include a detailed shell tower (all models in coupled tools) should be treated with caution.

To assure that the complete tripod model that is used in this work is adequate, a parameter study varying the discretization is performed. The mesh size for the tripod model is modified with a parameter that gives the number of shell elements per circumference of the respective member. With this meshing, leading to the same number of finite ele-
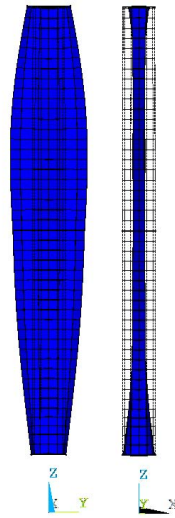
Figure 4.7: Tower mode not representable in beam model at a frequency of $f_{low} = 3.3\,\text{Hz}$.
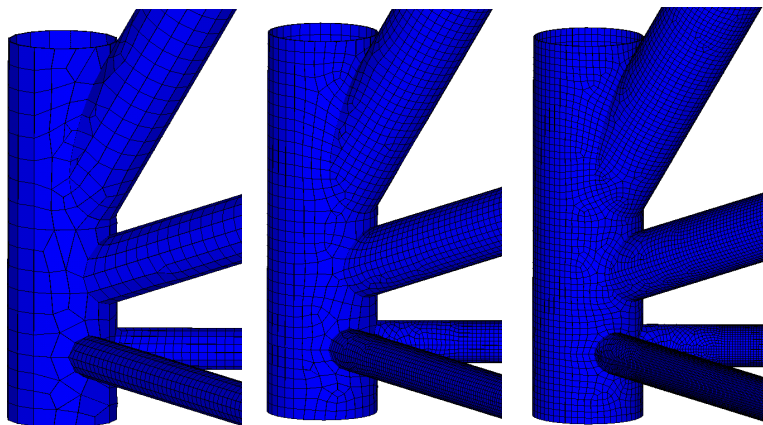
Figure 4.8: Tripod pile sleeve joint modeled with different discretizations.

ments around each tube, independent of the tube's absolute size, a relatively good mesh at the joints is obtained with an acceptable effort. Figure 4.8 shows a detail of a tripod joint with different discretizations in Ansys.

The mesh is not refined locally around the intersections of the tripod members at the joints (including the weldseams in case of a welded joint) as it is common when modeling such steel structures for the following reason: When comparing a locally refined model to a model which has the same (very fine) mesh for the whole structure, the main difference is the computational effort when simulating the models. Simulation results are very similar in both cases. Herein, the computational effort when simulating is not very critical, because only few and simple load cases are run with the shell reference model. The basic parameters dead weight and first eigenfrequencies are compared because a good convergence of those parameters implies that an accurate mass and stiffness distribution and finally a good coincidence of dynamic properties from the structural side is achieved. Models with four to 56 elements per circumference of each tubular tripod member are compared.

The convergence of the masses is very good in the shell model. Neglecting only the two
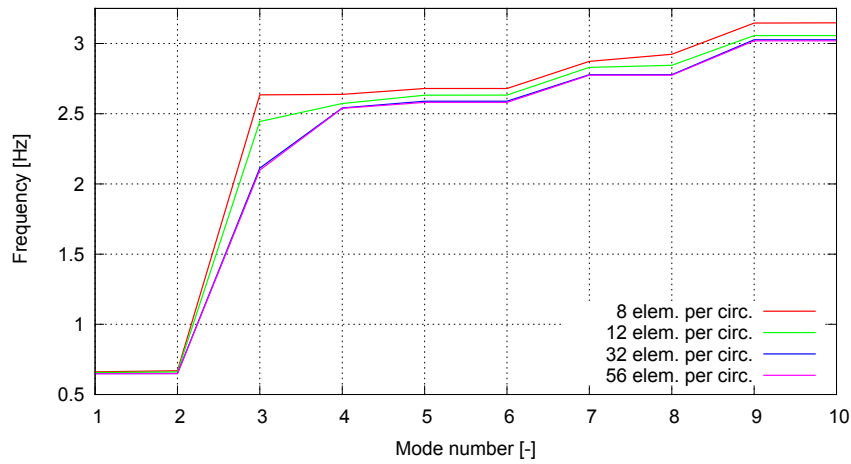
Figure 4.9: Eigenfrequencies and mode numbers for tripod shell models with varying discretization. The legend gives the number of elements per circumference of each member for the respective tripod model.

coarsest discretizations (four, respectively six elements per circumference), the maximum dead weight difference is $\Delta m = 0.03\,\%$. ($\approx 300\,\mathrm{kg}$) which is obviously negligible.

Figure 4.9 shows natural frequency versus mode number for the first ten eigenmodes of the tripod for different discretizations. The legend gives the number of elements per circumference of each member of the respective tripod model. The eigenfrequency results differ visibly between the models with the coarse discretizations. Between 32 and 56 elements per circumference, the differences are very small. For the first two frequencies, the differences are small for all discretizations, for the 3rd, the differences are highest. The higher frequencies (4th to 10th eigenfrequency), differ for the smaller discretizations only.

In Figure 4.10, differences are shown percentagewise and related to the model with the highest discretization (56 elements per circumference) for a larger set of models.

A good convergence is directly visible and – apart from the 3rd eigenfrequency for 52 elements per circumference – the discrepancies are positive, i.e., the lower fidelity models are stiffer. As already shown in Figure 4.9, the 3rd eigenfrequency shows the largest differences. For models with 12 or more elements per circumference, all differences lie under $\Delta f_{\mathrm{max}} = 2.5\,\%$ except for the 3rd eigenfrequency (upper figure). For higher discretizations, the differences for the 3rd eigenfrequency decrease significantly as well. For models with 32 or more elements per circumference, all differences are under $\Delta f_{\mathrm{max}} = 0.75\,\%$ (lower figure)

In general, the approach of relating the results to the highest fidelity model should be treated with caution because it must be assured, that these are the most realistic. However, in a case with a clear convergence as shown here, this is not that critical.

Different discretizations may lead to slightly different stiffness distributions, i.e. there are general differences between two models, and the differences may be larger for certain components. As an example, joint stiffnesses may be sensitive to the differing discretization, because the joints have complicated geometries, that cannot be modeled accurately with only a few shell elements. Usually, joint stiffness decreases with an increasing number of elements in a certain range of discretizations. But the global stiffness
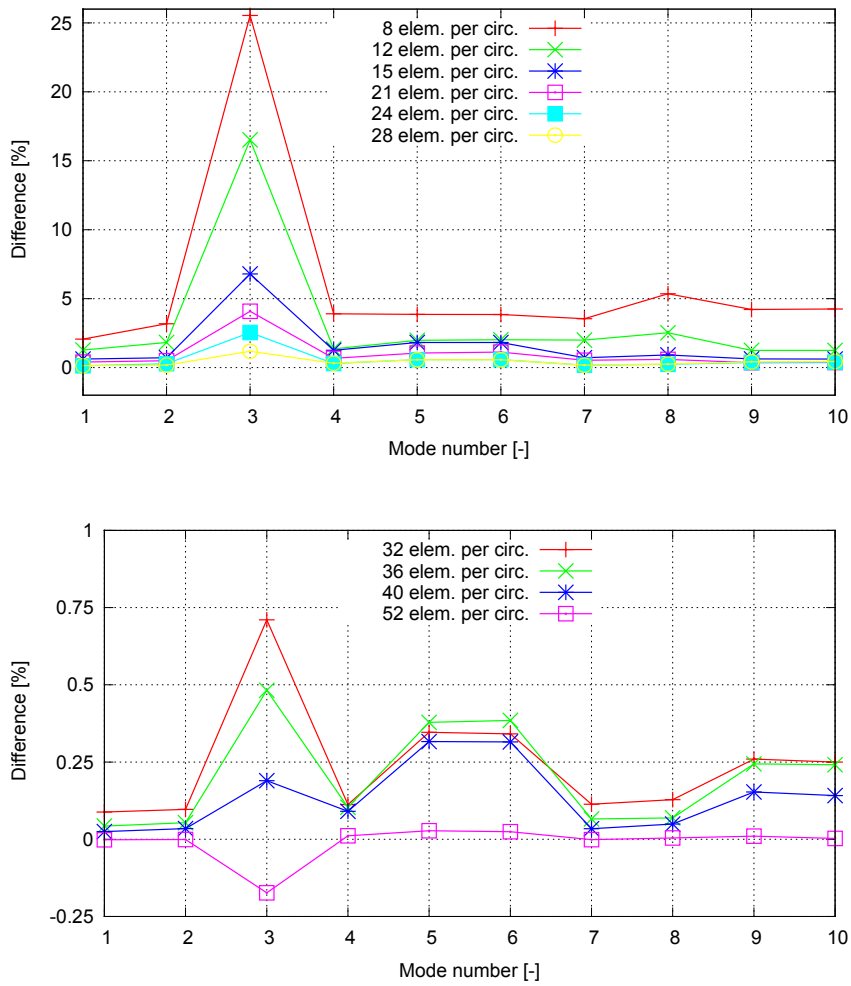
Figure 4.10: Eigenfrequency differences and mode numbers for tripod shell models with varying discretizations relative to the model with the highest discretization (56 elements per circumference of each member). The legend gives the elements per circumference of each member in the respective model.

of a tripod (i.e. the eigenfrequencies associated with global modes) may be described accurately even using a small number of members.

Due to this kind of stiffness changes, local modes can change positions when being listed by increasing frequency in comparisons between models with different discretizations. As the model modification influences the various eigenstates differently, other eigenvalues become associated with frequencies lying close together. This results in combined modes in one model, that are not described using the other model and vice versa. Additionally, one model may lead to modes that combine the same, or nearly the same, single modes, but in other relative portions than described in the second model. The results of a brief study on the mode shapes are not shown here, however, for coarser discretizations, the 1st global torsion or the 2nd global bending mode shapes *change places* with different bending mode shapes of the mudbraces and combine with these in different configurations.

The model with 12 elements per circumference of each members is selected for the following description of the mode shapes because, starting with this discretization, the ordering of the mode shapes no more changes for higher fidelity models. The mode shapes corresponding to the respective frequencies are briefly described in Table 4.7.

Table 4.7: Tripod frequencies and description of mode shapes for the tripod shell model with 12 elements per circumference of each member.

Frequency [Hz]	Description
0.657	1st global bending
0.660	1st global bending
2.445	1st global torsion
2.573	Local bending of mudbraces
2.631	Local bending of mudbraces
2.633	Local bending of mudbraces
2.830	2nd global bending combined with mudbrace bending mode
2.845	2nd global bending combined with mudbrace bending mode
3.056	Local bending of mudbraces
3.057	Local bending of mudbraces

Figure 4.11 shows the 3rd mode shape described in Table 4.7, because for this mode, the largest frequency differences (visible in Figure 4.9 and Figure 4.10.) are described.

It is directly visible, that for the calculation of the mode shape, a proper description of different parts of the relatively complicated tripod structure is necessary. The torsional mode does not only include the tripod legs and the tower, but the central joint and all pile sleeve joints in a complicated deformation. Modeling of the tube intersections at the joints and e.g. local indentations in these areas become important here. This explains the difficulties finding a frequency convergence for this mode even for discretizations finer than with 12 elements per circumference, i.e. discretizations at which the mode shape positions do no more change positions (cf. above). However, as shown in Figure 4.10 (bottom) the frequencies converge for finer discretized models.

As a further plausibility check, a model including the RNA defined as a mass point is set up and a modal analysis is performed. Figure 4.12 shows the resulting frequencies, for the first ten mode shapes again (blue line) for a model with 32 elements per circumference for each member. Additionally, the averaged results from the OC3 project (clear outliers are not taken into account) are included (red dots) for the 1st, 2nd, 4th and 5th mode shape. These are 1st and 2nd global bending modes. Other support structure mode shapes found here are not published in OC3, as the support structure is not investigated in that detail (see Vorpahl et al. (2013), p. 534, Figure 18 for the frequencies shown here).
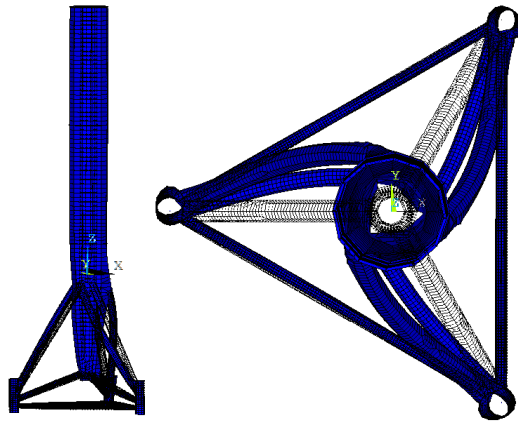
Figure 4.11: Side view and top view of the tripod's first global torsional mode at $f_3 =$ $2.445\,\mathrm{Hz}$ (3$^{\mathrm{rd}}$ mode) as described in Table 4.7.

As expected, the frequencies are shifted to lower values due to the large tower top mass and inertia when comparing these results to the results shown in Figure 4.9. Mode one and mode two are the 1$^{\mathrm{st}}$ global bending modes, mode three is the 1$^{\mathrm{st}}$ global torsion. The 2$^{\mathrm{nd}}$ global support structure bending modes are found here as mode number four and five (Instead of seven and eight in Figure 4.9 and Table 4.7). Mode six to ten are local brace bending modes and modes. As expected, frequencies associated with global modes are shifted more significant than those referring to local modes.

Three more points must be stated: First, the calculated frequencies lie in an expected range, the first two eigenfrequencies are even very close to the OC3 results. Second, there is a relatively large difference for the 2$^{\mathrm{nd}}$ global support structure bending modes between the OC3 results and the results found herein. This is due to the complex combined modes, that cannot be described accurately in the OC3 models, that are beam models or comparable to beam models. The higher fidelity models used here are expected to be more realistic. The mode shape includes a *flattening* of the tower base shell close to the central joint, that cannot be described with beam models (not shown here). Furthermore, as described above, even the shell models tend to become more compliant for finer discretizations. Therefore a stiffer representation in the lower fidelity models in OC3 is expected. Third, the differences between the shell models used here are very small compared to the difference to the OC3 average and compared to the differences between the single models benchmarked in OC3 (not shown here).

The investigations presented in this section lead to the following conclusions:

- The tower in a shell reference model for comparisons with results from coupled tools must be defined including flanges. If this is not the case, the mode with the lowest eigenfrequency including a large portion of an unrealistic tower deformation mode is found at $f_4 = 2.263\,\mathrm{Hz}$ for the structure used herein.

- Even with a realistic tower model, the lowest tower eigenfrequency, that can only be described with shell models (or even more detailed models) is found at $f_{\mathrm{low}} =$ $3.3\,\mathrm{Hz}$ for this structure. Therefore, eigenfrequencies over this value should be treated with caution in coupled tools where these tower frequencies are not modeled.

- For tripod models with different discretizations, a convergence of the dead weight of the structure is found directly for a relatively low number of members.
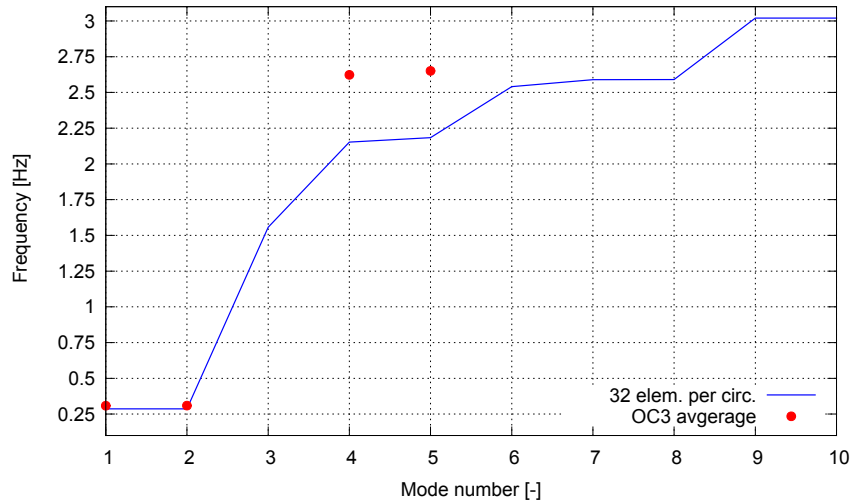
Figure 4.12: Eigenfrequencies and mode numbers for tripod shell model with 32 elements per circumference of each member including RNA as a point mass (blue line). Averaged results from OC3 project are displayed additionally (red dots).

- The ordering of mode shapes converges fast.

- A clear convergence of the 3rd eigenfrequency, which is related to the 1st global torsional mode of the structure is found for relatively fine discretiztions only, this is due to the complex mode shape.

- Frequency differences compared to the results found in the OC3 project can be traced back to the lower fidelity models in this project, and to the complexity of the mode shapes that is not fully representable in those models.

- The eigenfrequencies that are of interest herein clearly converge using the presented model set up.

- The frequency differences between the models investigated are under $\Delta f_{\mathrm{max}}=0.75\,\%$ for models with more than 32 elements per circumference of each member.

Based on the findings described in this section, a shell model with 32 elements per circumference of each member members leading to a number of DOFs of $n_{\mathrm{shell}}{=}586,488$ DOFs is used as a reference model.

4.3.4   Shell-joint model

As a basis for the superelement model, a shell-joint model is defined. Compared to the beam model, the beam elements representing all joints are replaced by shell elements. The master nodes defined to connect the shell joints to the residual structure are located in the centerlines of the tubular chord and brace members and are rigidly connected to the outgoing beam element and rigidly connected to the respective shell joint. Figure 4.13 shows a tripod model with shell joints and the central joint in detail. The model described herein has a number of DOFs of approximately $n_{\mathrm{shj}} = 50,000$ DOFs.
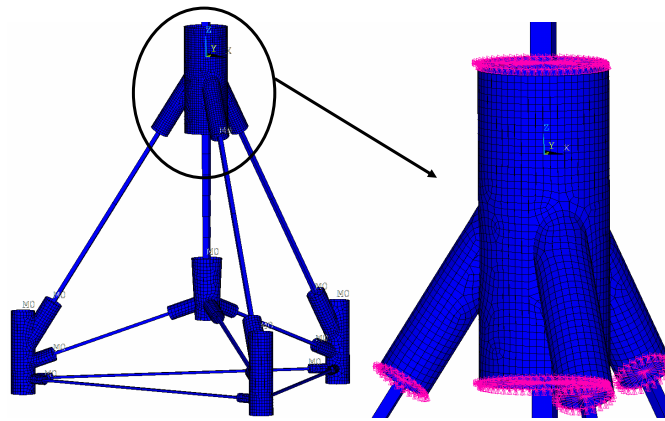
Figure 4.13: Tripod modeled with shells and beams (left) and shell central joint (right).
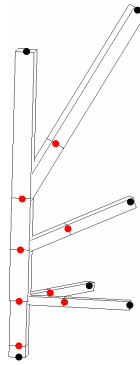
Figure 4.14: Tripod pile sleeve joint modeled with beam elements with fourteen nodes (black and red dots) and modeled as a superelement with six nodes (black dots only).

4.3.5 Superelement model

The superelement model is based on the shell-joint model with the shell joints being replaced by superelements using a Guyan reduction procedure (cf. Section 2.3.7). The residual beam structure remains unchanged compared to the other models.

The number of DOFs of this structure is $n_{\mathrm{super}} = 474$ DOFs, a value even significantly below its counterpart for the basic beam model. The reason for this is as follows: The DOFs of each superelement are only the DOFs of its master nodes. As mentioned in Section 4.3.2, several supplementary members have to be included in the basic beam model to allow for more realistic load simulation, i.e. to avoid overlapping members, at the joints. Furthermore, changing properties of the tubes such as diameters D_i or thicknesses t_i are modeled with several beam elements and at the intersection points, a node has to be defined which leads to more elements as well. The parts of the structure modeled with those supplementary beam elements become part of the superelements and therefore those DOFs are condensed when preparing the superelement model. Figure 4.14 shows the beam model of a pile sleeve joint with fourteen nodes (black and red dots) and a resulting number of DOFs of $n_{\mathrm{beam,psj}} = 84$ DOFs. The six master nodes of the corresponding superelement are shown as black dots; the number of DOFs of the superelement is $n_{\mathrm{super,psj}} = 36$ DOFs.
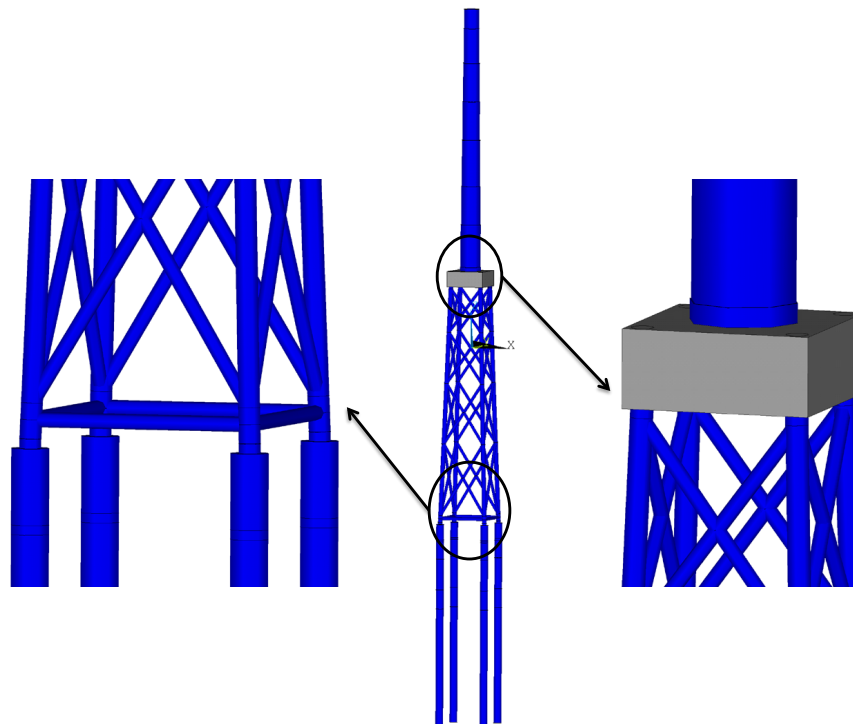
Figure 4.15: Jacket with tower and piles (middle), detail of concrete TP (right) and lowest bay including pile heads (left).

4.4 Jacket support structure

The jacket support structure models that are used in this study are based on the structure – consisting of jacket substructure and tubular tower – as described in Vorpahl et al. (2011) for OC4 that was based on a jacket design given in Vemula et al. (2010). See also Tu (2013) and Tu and Vorpahl (2014) on jacket modeling. Section 4.4.1 gives the structural properties i.e. the physical properties of the jacket as implemented in numerical models. The following sections describe the models that are used in this study. Section 4.4.2 introduces the development of the beam model. The reference shell model is defined in Section 4.4.3. Section 4.4.4 provides the description of a shell-joint model and based on that, a superelement model is derived as delineated in Section 4.4.5.

4.4.1 Structural properties and general modeling assumptions

The support structure was designed for a water depth of 50 m. The four-legged jacket substructure features four levels of X-braces and joints (X1 to X4, top-down), three levels of double-K-Joints (K1 to K3, top-down) double-Y-joints at the top of the structure and combined double-Y- and double-T-joints at the bottom. Jacket stabs are used and the penetration depth of the piles is 45 m. Mudbraces and a grouted concrete TP are used. The total jacket height from mudline excluding the tower is 70.15 m, including the conical tower of 68 m in length this leads to a hub height of 90.55 m with the RNA as described in Section 4.2 atop. Figure 4.15 shows the structure. Figure 4.16 shows the jacket primary steel without TP and piles (cut at mudline) with its members colored based on the respective properties that are given in Table 4.8. The table gives the description of each component, its color in Figure 4.16 and the properties outer diameter D and wall thick-
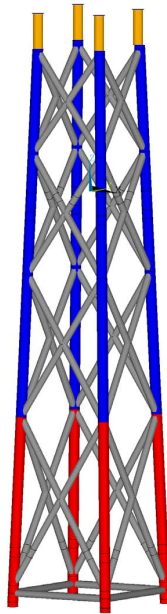
Figure 4.16: Jacket with member properties (cf. Table 4.8) indicated with colors.

ness t.

Table 4.8: Properties of jacket members.

Component	Color in Figure 4.16	D [m]	t [mm]
X- and mudbraces	Grey	0.8	20
Leg at lowest bay	Red	1.2	50
Leg 2nd to 4th bay	Blue	1.2	35
Leg crossing TP	Orange	1.2	40
Pile	Not shown	2.082	60

Mean wind and wave directions are aligned and the jacket is positioned with its sides (top view) parallel to the x- and y-axis respectively. Table 4.9 gives definitions to clearly identify to jacket legs and sides in global coordinates.

The legs of the jacket structure are free flooded, the braces are not. Marine growth (thickness t_{grow} and mass ρ_{grow}) is assumed as recommended by the respective guidelines (cf. e.g. DNV-OS-J101 (2014)) and given by Fischer and Kühn (2009). This is mainly to make sure that local vibration phenomena of single members are not falsified due to the missing growth mass. Table D.4 gives the parameters for marine growth definition. It is not accounted for any appurtenances and the models defined in the following are cantilevered at mudline, i.e. piles are not defined. Appendix D gives nodes (see Table D.1) and node connectivities (see Table D.2) of the jacket. Furthermore, the tower is defined in terms of cross sectional properties in this appendix (see Table D.3). Using the masses given in this table, flanges are defined based on the findings given in Section 4.3.3. The flange properties are provided in Table B.1.

Table 4.9: Description for identification of jacket joints, members and positions.

Description	Name	Position
Jacket leg 1	L1	$x > 0; y > 0$
Jacket leg 2	L2	$x < 0; y > 0$
Jacket leg 3	L3	$x < 0; y < 0$
Jacket leg 4	L4	$x > 0; y < 0$
Jacket side 1	S1	Leg 1 to leg 2
Jacket side 2	S2	Leg 2 to leg 3
Jacket side 3	S3	Leg 3 to leg 4
Jacket side 4	S4	Leg 4 to leg 1

4.4.2 Beam model

In Section 4.3.2 it is already described, that the development of the beam model (herein, EB Beams are used) requires a certain effort. It needs to be assured, that the model is suitable for this type of structure and that limitations that are found are due to the type of model (beams) itself and not due to insufficiency in the modeling (e.g. discretization).

Prior to the definition of the jacket model for the OC4 project (cf. Vorpahl et al. (2011)) the influence of different modeling strategies is investigated in Kaufer et al. (2010). The influence of overlapping members (cf. Figure 4.3) on dead weight, eigenfrequencies and DEL is relatively small and therefore the use of a basic model is recommended.

The original jacket design includes joint cans to meet the stress requirements in the respective standards. Therefore the necessity of joint can modeling in the context of global dynamics is investigated. For this purpose a basic model of the OWT without joint cans and a model including joint cans are defined. The basic model is verified via comparison of masses and first natural frequencies to Flex-Poseidon and GH-Bladed (cf. Table 2.3.3 for the tool descriptions). The model including joint cans is verified in terms of the extra masses compared to a spreadsheet calculation. The mass difference for the two models is $\Delta m \approx 32\,\mathrm{tons}$. A frequency comparison is shown in Figure 4.10 for frequencies up to 3 Hz. Differences are based on the model without joint cans, i.e. negative percentages stand for higher values calculated with the model without joint cans.

Table 4.10: Frequency comparison for OWT models of jacket with and without joint cans. Differences are related to the model without joint cans.

Mode number [-]	Diff. [%]	Mode number [-]	Diff. [%]
1	-0.67	9	-0.14
2	-0.68	10	-0.18
3	-0.18	11	-0.26
4	-0.04	12	0
5	-0.03	13	0
6	-0.14	14	-0.02
7	-0.32	15	0.13
8	-0.15	16	0.48

The Frequency difference is under $\Delta f_{\mathrm{max}} = 0.75\,\%$, which is negligible. Even with a mass difference of $\Delta m \approx 32\,\mathrm{tons}$, the basic model is further used because the mass difference is not expected to be important when it comes to dynamic OWT simulation and the definition of joint cans requires a significant modeling and computational effort. This is in
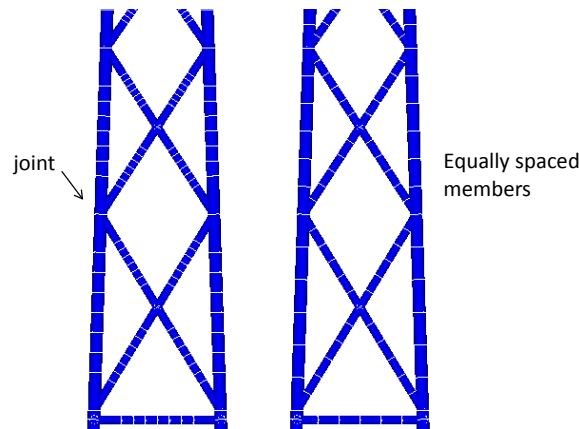
Figure 4.17: Parts of jacket models including separate joints (left) and without separate joints (right).

accordance with the decision that was made in OC4[13]. The resulting basic model is used in OC4 and serves as a starting point for this work.

The wave load calculation – concerning its accuracy close to MSL – is realized as described in Section 4.3.2, the wave load calculation therefore is independent of the structural discretization.

In the next step, discretization checks are conducted. This is realized more deeply than for the tripod for the following reason: The tripods mudbraces are very slender and therefore prone to be sensitive to discretization (cf. Section 4.3.2 where these members are checked). In the case of the jacket, different brace and chord members have a comparable slenderness and therefore the structure is investigated as a whole.

Three groups of models are set up and the respective parameter studies are realized. In the first group of jacket models, the number of finite elements per member is varied from one to 80, every single member is treated in the same way, i.e. the number of elements for a chord and a brace are the same in one model and elements are equally spaced. Figure 4.17 (right) shows a model of this type with six elements per member.

The second group of models has a fixed joint size and the number of elements between the joints is modified again from one to 80 to allow for a better comparisons to the models including shell elements (cf. Section 4.4.4) and superelements (cf. Section 4.4.5). Figure 4.17, left shows a model of this type with six elements per member between the joints.

Finally, the joint size is modified (cf. joint size in Figure 4.17, left). For this purpose, a reference joint size is used based on the findings in Dubois et al. (2013). The length to diameter ratios for this reference size are as shown in Equation 4.9 and Equation 4.10. The chord length L measures from (1) the connection of the joint to the residual structure to (2) the intersection points of centerlines of brace and chord members (continuous chords). The brace length l is measured from (1) the connection of the joint to the residual structure to (2) the chord radius (brace welded to the outer chord area).

$$\alpha_{\mathrm{ch}} = L/D_j = 3 \tag{4.9}$$

$$\alpha_{\mathrm{br}} = l/d_j = 2.5 \tag{4.10}$$

---

[13]OC4 Project, 2nd Full Committee Meeting, October 29, 2010, 9:00 – 17:00, Germanischer Lloyd Group – Head Office, Hamburg, Germany, Meeting Minutes.
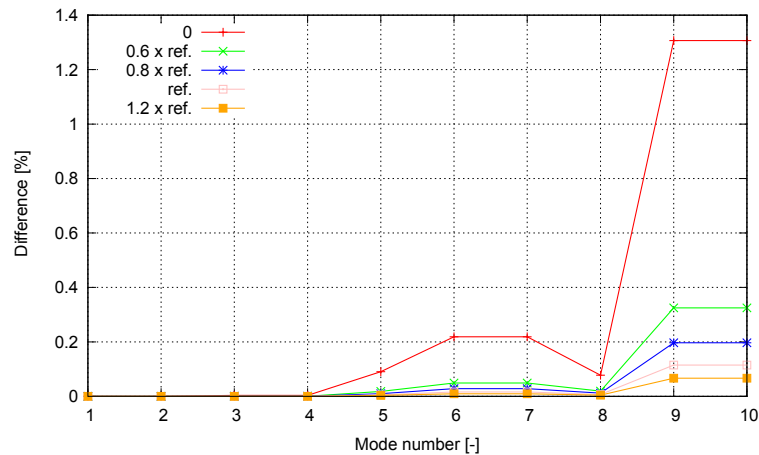
Figure 4.18: Differences in eigenfrequencies relative to the reference beam model for jacket models with one beam element per member and different joint sizes. Joint sizes are based on the reference joint size (cf. Equation 4.9 and Equation 4.10).

The masses remain approximately the same for all models. Figure 4.18 shows the differences of the eigenfrequencies for the first ten modes relative to a reference beam model with 80 elements per member as exemplary eigenfrequency results. Results are shown for models with different joint sizes. All models have only one element per member (least accurate models of the respective group of models).

It is directly visible, that the differences are very small. Apart from the model without separate joints, the differences for all investigated frequencies are under $\Delta f_{\mathrm{max}} = 0.4\,\%$. As expected, the results are converging with increasing joint size, which means a change of parameters towards a model with two elements per member with equal spacing.

The results of the discretization studies are summarized as follows:

- For accurate mass representation, the simplest beam models are sufficient.

- For sufficient eigenfrequency description, one element per member is adequate if the joints are modeled.

- The joint size influence on frequencies is also small.

Based on these findings, a beam model with one element per member including separate elements to represent the joints – leading to $n_{\mathrm{beam}} = 1,428$ DOFs – is further used in this study. This model is based on the findings of the OC4 project and further discretization studies were carried out to assure its usability as a beam model representing the state of the art jacket modeling in loads simulation.

4.4.3 Shell model

A model consisting of Shell elements is defined using the geometrical parameters of the jacket as defined in Section 4.4.1. The TP and the grouted parts of the foundation piles and jacket legs are kept as beam members for simplicity. This is possible due to two reasons. Firstly, these elements are very stiff (concrete blocks) and therefore do not have a large influence on the dynamic model properties that are investigated herein. Secondly, the grouted connections are not in the focus of this study.
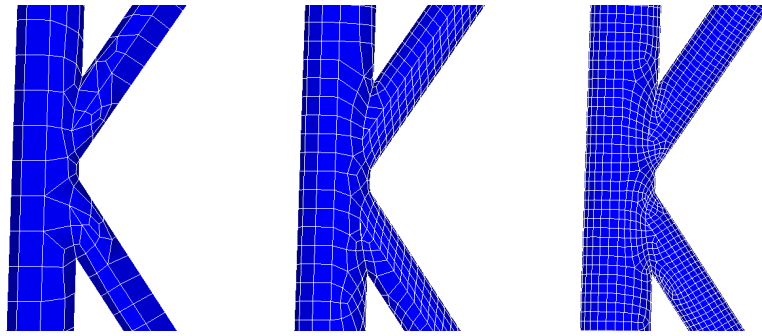
Figure 4.19: Two dimensional view of K-Joint modeled with different discretizations.

As described for the tripod shell model (Section 4.3.3), flanges are modeled to avoid unrealistically low tower shell deformation frequencies. The flange masses are given for the tower to be used with the jacket (cf. Table D.3). The geometric properties of the flanges are defined in Table B.1. In order to meet the given mass and geometric properties, the density of the flanges is modified compared to the residual structure. The resulting flange densities $\rho_{\mathrm{fl.}}$ are given in Table B.1.

The shell elements setting up the structure are defined on their center areas. Therefore, small gaps in the model are allocated at the thickness steps in the structure (See for example Table 4.8, between the leg in the lowest jacket bay and the residual leg). The nodes at these positions are merged to assure a smooth connection and to avoid supplementary stiffness that would be implemented with the use of contact elements[14].

A parameter study with increasing number of elements is conducted to find a suitable mesh. As described in Section 4.3.3 for the tripod model, the number of elements per circumference is changed with one parameter for all members which leads to a good mesh quality with an acceptable effort. The number of elements per circumference is increased stepwise from four to 56. Figure 4.19 shows one of the jacket's K-Joints modeled with different discretizations. The mesh quality increase with decreasing element size is directly visible.

The structural mass convergence of the models is clear and relatively fast. With 12 elements per circumference, the mass difference is under Δm=0.5 % (relative to the mass of the support structure as a whole). The first 15 eigenfrequencies and the corresponding mode shapes are investigated. As for the tripod model (cf. Section 4.3.3) the stiffness changes due to the modified discretization have different magnitudes and influences in the different parts of the structure and therefore, the ordering of the mode shapes changes for coarse discretizations. It is found, that the ordering of the mode shapes remains constant for models with 16 elements per circumference or more. Table 4.11 gives the frequencies and a description of the mode shape for the first 15 modes for a model with 16 elements per circumference. The selection of frequencies and associated mode shapes nicely shows the different types of modes – Global modes, local modes and shell deformation modes – and the respective ordering. The 3rd global bending mode is found at a higher frequency than the lowest modes representing shell deformations (Number six and seven).

The following is important concerning this result: Mode shapes six and seven as well as eleven and twelve are mainly shell deformation mode shapes. The lowest frequency including a large portion of shell deformation (that is by definition not included in a beam model (see also Section 4.3.3) lies at f_{low}=5 Hz, meaning that higher frequencies resulting from a system simulation not including detailed shell models should be treated with

---

[14]The use of contact elements would be the second possibility to deal with the gaps.

Table 4.11: First 15 eigenfrequencies and mode shape descriptions for the jacket shell model.

Frequency [Hz]	Description
0.70	1st global bending
0.70	1st global bending
1.54	2nd nd global bending
1.54	2nd nd global bending
3.16	1st global torsion
5.00	Mainly tower shell deformation
5.00	Mainly tower shell deformation
5.16	3rd global bending
5.16	3rd global bending
6.23	*Stretching* of the jacket
6.64	Mainly tower shell deformation
6.64	Mainly tower shell deformation
6.70	4th global bending with local bending
6.71	4th global bending with local bending
7.27	*Flattening* of the jacket

caution. Figure 4.20 and Figure 4.21 give the first 15 modes, frequencies and respective differences (related to the highest fidelity model with 56 elements per circumference).

Both figures show that the differences due to the discretization are relatively small in general. The largest differences occur for mode numbers six and seven, smaller, but still remarkable differences occur for modes 11, 12 and five. Mode six, seven, 11 and 12 are not too interesting for the purpose of this study, these are shell deformation modes as mentioned above that are not suitable for further comparisons. However, if this would be of deeper interest, an earlier convergence for the model as a whole could be achieved when increasing the tower discretization only. This evident assumption is assured with a brief parameter study (results not shown here). Mode number five is the first global torsional mode which is more complex and therefore needs a finer discretization for acceptable modeling accuracy. See Section 4.3.3 and Figure 4.11 for the description of this topic in conjunction with the tripod structure. Excluding the shell deformation modes, the differences for the first 15 frequencies are under $\Delta f_{max} = 0.5\,\%$ for a model with 28 elements per circumference or more.

A further plausibility check is conducted as follows: The frequencies obtained with the shell model with 28 elements per circumference including a RNA (modeled as a point mass) are compared to results of the OC4 project. The OC4 results are obtained from the raw data for the eigenanalysis called OC4 load case 1.0a (see Vorpahl and Popko (2011) for the load case description). Comparable results are published in Popko et al. (2014). The results are shown in Figure 4.22, where the frequencies for the shell model (green line) and the average of the respective OC4-results (red dots) are shown.

Only modes one to five (1st global bending, 2nd global bending, global torsion) are obtained in OC4, because the support structure is not investigated in such detail in this project. All frequencies are shifted to lower values due to the RNA mass and inertia. The results obtained with the shell model herein fit very well to the OC4 results. The differences are negligible when taking the spread in the OC4 results into account.

Based on extensive parametric studies as described in this section, the following is concluded:

- With a realistic tower model including flanges, the lowest frequency that can not be described with a beam model (deformation of the tower shell) lies at $f_{low} = 5\,\mathrm{Hz}$ for this structure.
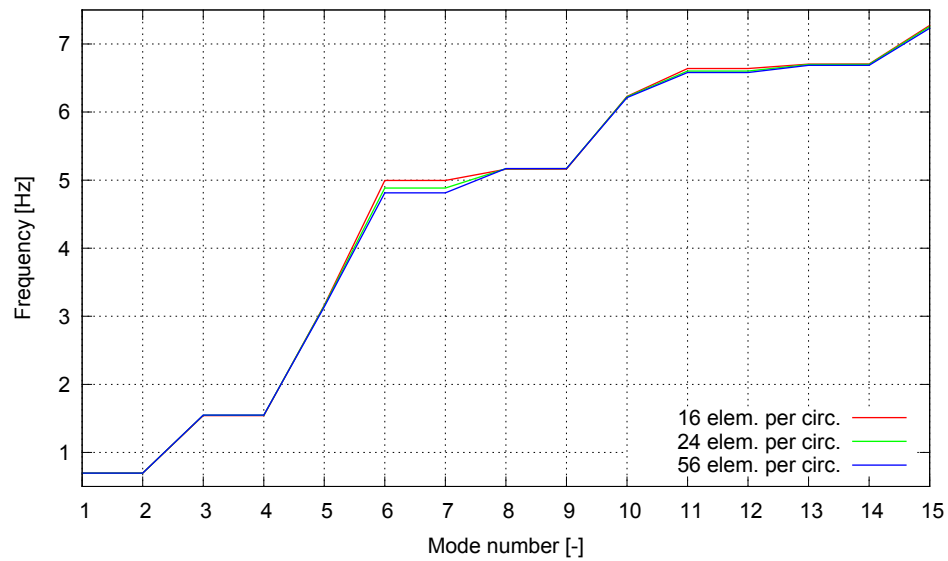
Figure 4.20: Jacket eigenfrequencies and mode shapes for different discretizations. The number of elements per circumference for each member (for the respective model) is given in the legend.
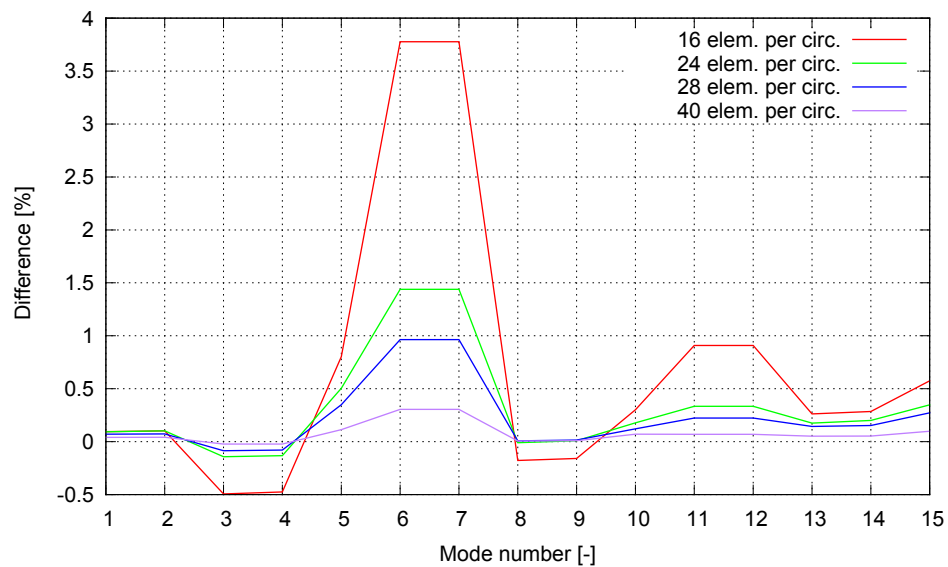
Figure 4.21: Differences of jacket eigenfrequencies and mode shapes for different discretizations related to the highest fidelity jacket model (56 elements per circumference for each member). The number of elements per circumference for each member (for the respective model) is given in the legend.
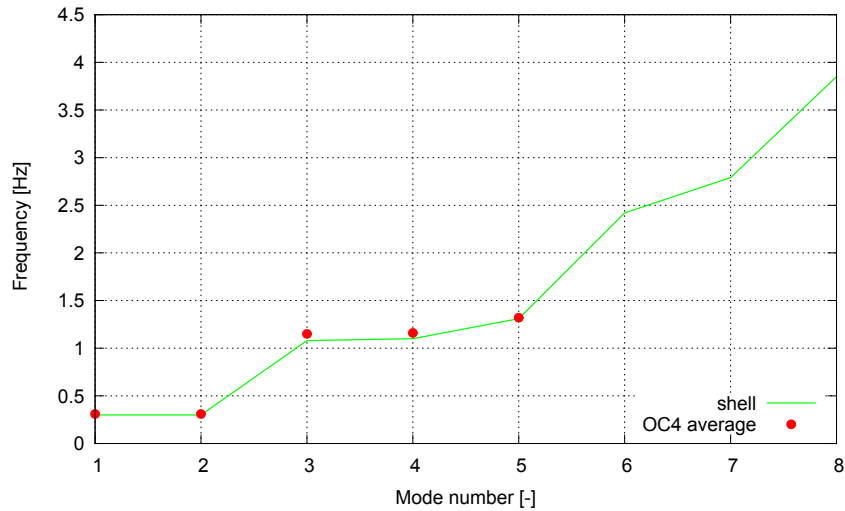
Figure 4.22: Eigenfrequencies and mode numbers for jacket shell model with 28 elements per circumference of each member (green line). The RNA is included as a point mass in the model. Results from the OC4 project are displayed additionally (average values as red dots).

- The dead weight of the structure converges very fast with decreasing element size.

- The ordering of the mode shapes converges relatively fast too.

- In general, frequencies clearly converge.

- Frequencies related to shell deformation modes and to the global torsional mode converge slower than others.

- The maximum frequency differences fall under $\Delta f_{\max} = 0.5\,\%$ for models with 28 elements per circumference or more (shell deformations excluded).

- For the model with 28 elements per circumference, the frequency results including the RNA are plausible when comparing to the results from the OC4 project.

Based on these findings, a shell model of the jacket support structure with 28 elements per circumference of each member is defined as a reference model for the comparisons with lower fidelity models in the context of this study. The model has $n_{\mathrm{shell}} = 1,346,496$ DOFs.

4.4.4 Shell-joint model

A shell-joint model is defined being the starting point for the reduction procedure leading to the superelement model for dynamic simulation of the OWT. The model is based on the beam model, only the beam element joints are replaced by joints modeled with shell elements. Master nodes are defined in the centerlines of the outgoing members to connect the shell joints to the residual beam structure. The master nodes are rigidly connected to all shell model nodes at the circumference of the respective cross section. Figure 4.23 shows the jacket model as a whole (right) and a K-Joint (left) including master node positions (black), rigid connections (magenta) and outgoing beams (black).

The model has one beam element per member as a result of the findings in Section 4.4.2. The joints have 28 shell elements per circumference (cf. Section 4.4.3). A supplementary
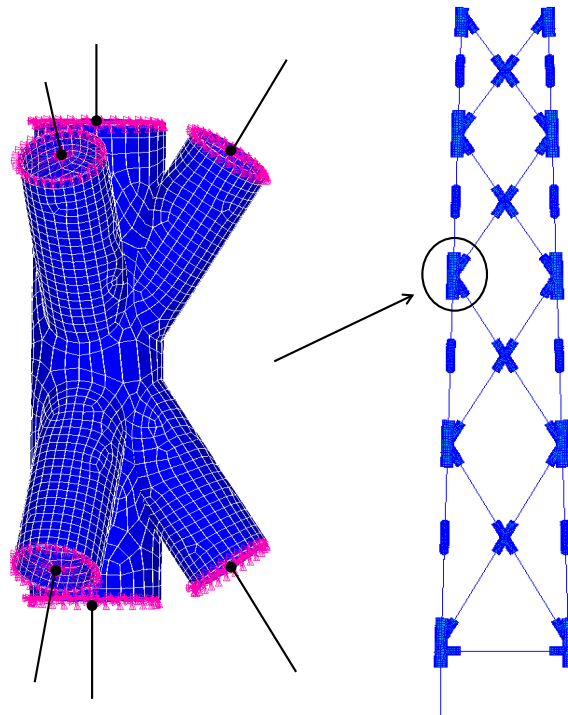
Figure 4.23: K-Joint in detail (left) and Shell-joint model of the jacket (right).

check of the global mass and the lowest eigenfrequencies is conducted against the shell reference model (Section 4.4.3) that leads to good results, i.e. similar masses and frequencies. Furthermore, a parametric study with varying size of the joints is realized. The shell parts in the model should be large enough to minimize the influence of the ovalization suppression (rigid connection of the shell joints to the residual beam members) on the joint model properties on the one hand. On the other hand, the wave loads in the dynamic analyses are applied on the master nodes only (cf. Section 5.2) and larger joints therefore increase a possible error source concerning the wave loads application. Based on this trade-off, the joint size is reduced to 0.6 times the reference joint size (See Equation 4.9 and Equation 4.9 for the reference joint size) and it is assured that the resulting error in frequencies and masses is acceptable (results not shown here). The resulting model has n_{shj}=436, 068 DOFs.

4.4.5   Superelement model

Using a Guyan reduction procedure (cf. Section 2.3.7), the superelement model is derived from the shell-joint model. The parts of the structure that are modeled with beam elements remain the same. The internal nodes of the shell joints are condensed, the master nodes are kept. Mass and natural frequencies are the same as for the shell-joint model by definition. The number of DOFs of this model is even lower than for the beam model. Figure 4.24 visualizes the reason for this reduction. As an example, the superelement model of the X-joint (right) features four nodes and $n_{\mathrm{super,xj}}=24$ DOFs, the same joint modeled with beams has five nodes and $n_{\mathrm{beam,xj}}=30$ DOFs. The jacket support structure superelement model as a whole has $n_{\mathrm{super}}=1,164$ DOFs.
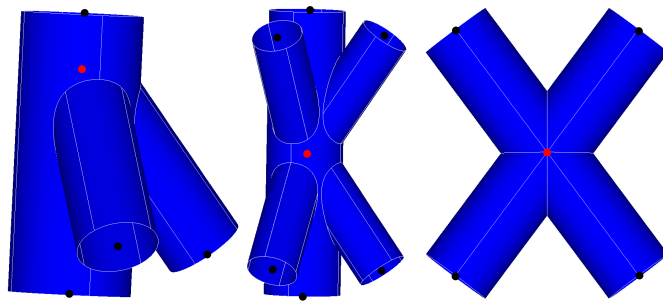
Figure 4.24: Jacket Y-joint, K-joint and X-joint with master node positions (black) and beam model node positions (black and red).

Chapter 5

Verification of ADCoS-Offshore

The onshore version of ADCoS is not verified in this work because this has been realized before (cf. Kleinhansl et al. (2004)). After the development of ADCoS, the tool was validated and extensively used for loads simulations by ADC. This work was not published due to confidentiality resons. In this section, ADCoS-Offshore is verified as part of the development process. Other tools for verification of ADCoS-Offshore including superelements in a coupled environment are not available to the author. Therefore, the verification is realized as follows: In a first step, presented in Section 5.1, results from ADCoS-Offshore are compared to results from other coupled tools using a beam model of the support structure in ADCoS-Offshore. This was realized as part of the aforementioned OC3 project, where a large set of calculated outputs was compared. Only a small subset of results is presented herein – namely those focused on the support structure's behavior under wave loading, because the wave load input is new to the former onshore version of ADCoS. More results of the OC3 project – including results calculated in ADCoS-Offshore are shown in the respective literature (see Nichols et al. (2009); Vorpahl et al. (2009, 2013)). In a second step, the implementation of the superelements is verified using a stepwise approach and simplified models in a comparison with results obtained with the general purpose FE tool Ansys in Section 5.2.

5.1 ADCoS-Offshore without superelements

In this section, the OWT (cf. Section 4.2) on top of the tripod support structure (cf. Section 4.3.1) set up as a basic beam model (cf. Section 4.3.2) is used. All results that were calculated with ADCoS-Offshore are shown in red[1], results provided by the other contributors to OC3 phase III[2] are shown in grey. This presentation allows for a direct overview on the ADCoS-Offshore results.

Figure 5.1 shows the first 13 full-system natural frequencies for the stationary but fully flexible OWT in the absence of water and gives a brief description of the corresponding modes. The *pitch* and *yaw* in the first and second blade modes describes the coupling of the blade mode with a nacelle pitch and yaw rotation respectively.

The drivetrain torsional natural frequency is not predicted in ADCoS-Offshore because the respective DOF is not implemented in the modal analysis here. This is of no further importance as ADCoS-Offshore uses a direct integration method for the time domain

---

[1]In Figure 5.5 (top and middle), the results from ADCoS-Offshore are hardly visible due to the very good agreement with the results from other partners.

[2]Partners that delivered results in OC3 Phase III: NREL, SWE, LUH, Risø DTU, GL, CENER.
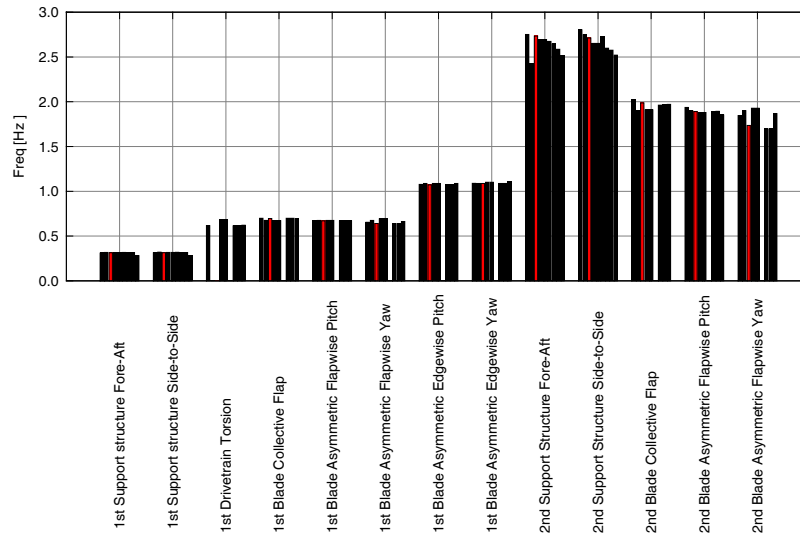
Figure 5.1: Full-system natural frequencies of the OWT on top of the tripod support structure including a short description of the corresponding modes. ADCoS-Offshore results are shown in red.

simulation (cf. Chapter 2.3.6). The eigenanalysis is only a supplementary feature and the lacking DOF in the modal analysis does not influence the time domain results. In the time domain simulations all valid DOFs are implemented. For the remaining natural frequencies, the accordance between the results from ADCoS-Offshore and the results from the remaining OC3 participants is very good. As the natural frequencies and mode shapes are coherent, a correct stiffness and mass representation of the OWT in ADCoS-Offshore is assumed and a similar dynamic behavior of the implemented turbine models can be expected.

Figure 5.2 shows the positions for comparison of load effects and their numbering. In Figure 5.3 and in Figure 5.4, the fore-aft bending moments calculated with the different tools for positions one to six are shown for a load case without wind, but with the rigid turbine structure loaded with the regular stream-function wave according to Dean
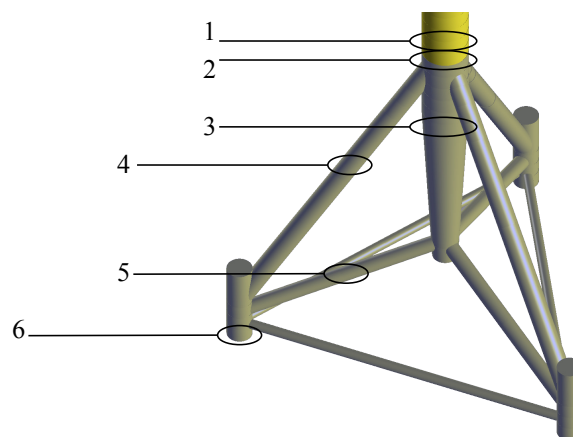
Figure 5.2: Tripod load effects output positions used in this section.

($H_{\mathrm{sf}} = 8\,\mathrm{m}$, $T_{\mathrm{sf}} = 10\,\mathrm{s}$) that is used in Section 4.3.2 as well. Figure 5.5 and Figure 5.6 give the fore-aft shear forces for the same load case.

The bending moment results in general agree well. A certain spread is visible for the lower brace and pile (locations five and six) which is mainly due to the beam formulation used in the different tools. This is not further evaluated herein, it is explained in detail in Vorpahl et al. (2013). All results from ADCoS-Offshore are in the range of results for the other tools.

The fore-aft shear forces do not agree as good as the bending moments (Figure 5.5 and Figure 5.6). The widest variation is seen in the central member (location three). There are several complications for the calculations of this force: the member is tapered; it is not inside a tree-like structure, so there are many paths that the loads can be distributed along; and it is at the height where the wave loads are strongest (see Vorpahl et al. (2013) again for details). The results calculated in ADCoS-Offshore agree very well with the results from most of the codes and in case of outliers (see locations two, three and four), predictions from ADCoS-Offshore are close to the values, that the majority of the codes predict.

Figure 5.7 and Figure 5.8 depict the periodic response of the now flexible OWT under excitation by the regular wave as described above. Figure 5.7 shows that the tower-top displacement is relatively similar in character between the codes. Most of the codes predict a similar phase of the motion as well but there are some outliers. The excitation described in two of the codes is visibly smaller than in the other codes. Most of the codes show an increasing excitation of different degrees. This means that a stationary response to the constant amplitude wave is not reached in the simulations. Both, the phase shift and the increasing amplitudes could be due to the initial conditions that are used for the simulation that have not yet died out. This is not investigated in detail herein, but more discussion of this issue is provided in Vorpahl et al. (2009). The results from ADCoS-Offshore compare well to the majority of the results. The support structure displacements at MSL (see Figure 5.8) show very good agreement, including the ADCoS-Offshore results. In this case, most of the motion is dominated by the action of the waves and not the dynamics of the structure. Summing up, the results shown here underline that the calculation of wave loads and the dynamics representation in ADCoS-Offshore in its basic version is accurate.

5.2   Stepwise verification of the superelement feature

The ADCoS-Offshore superelement feature is verified with a check of the stiffness matrix, the mass matrix and the load vector – i.e. the superelement – and the wave load redistribution scheme. The whole chain from model set-up in Ansys to the time domain simulation in ADCoS-Offshore (as shown in Section 3.2) is checked using simplified models. The global CS (cf. Appendix E) is used.

The model for the stiffness matrix testing is shown in Figure 5.9 (left). It consists of the tripod central joint superelement (see Figure 4.13), that is cantilevered at all of its downward master nodes (tripod leg members and central column member, black dots) and one short beam element for load application on top of the joint.

Three static force components (F_x=F_y= $30\,\mathrm{MN}$, F_z= $80\,\mathrm{MN}$) and a torsional moment (M_z= $1\,\mathrm{GNm}$) are applied at the load application node of the structure (red dot). All resulting deflections at this node are exactly the same except for the vertical deflection. However, the difference is only ΔF_z= $0.17\,\%$, it may even result from rounding errors in the different FE systems and is therefore not evaluated further.
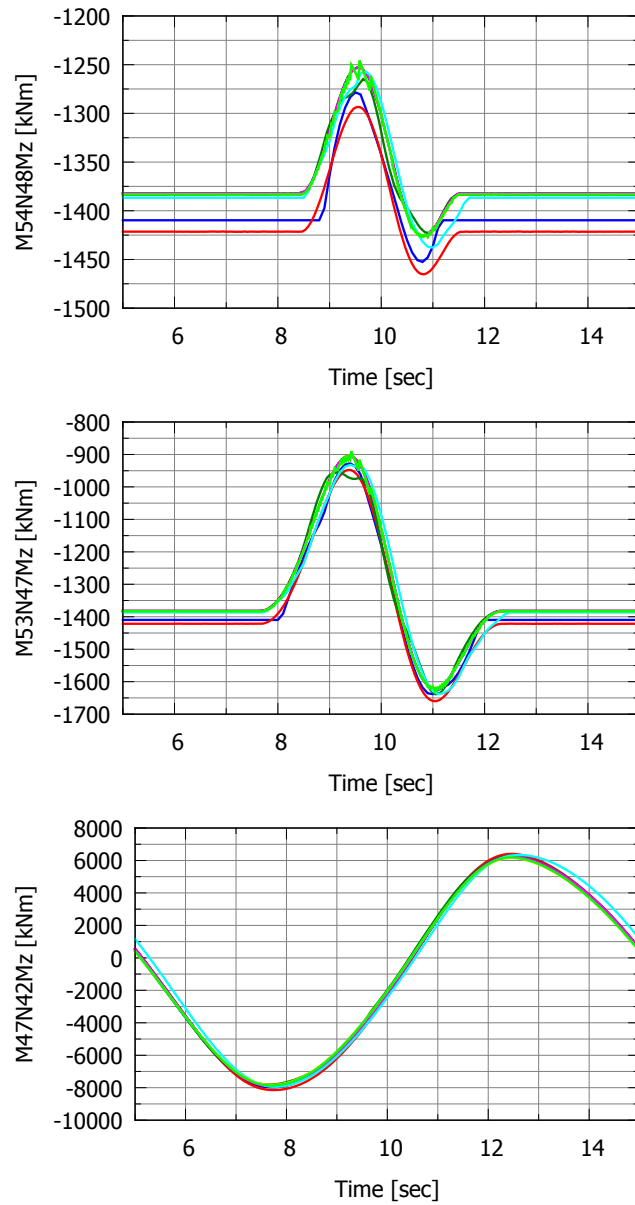
Figure 5.3: Fore-aft bending moment at locations one to three (cf. Figure 5.2) for a rigid OWT under periodic wave loading (top to bottom). ADCoS-Offshore results are shown in red.
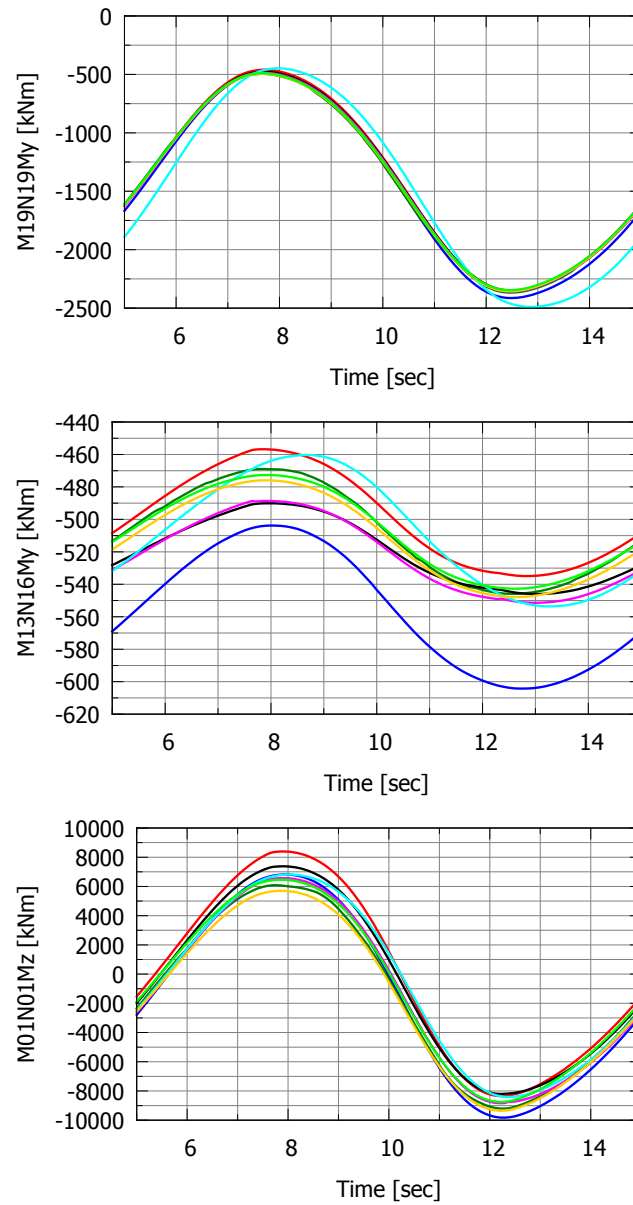
Figure 5.4: Fore-aft bending moment at locations four to six (cf. Figure 5.2) for a rigid OWT under periodic wave loading (top to bottom). ADCoS-Offshore results are shown in red.
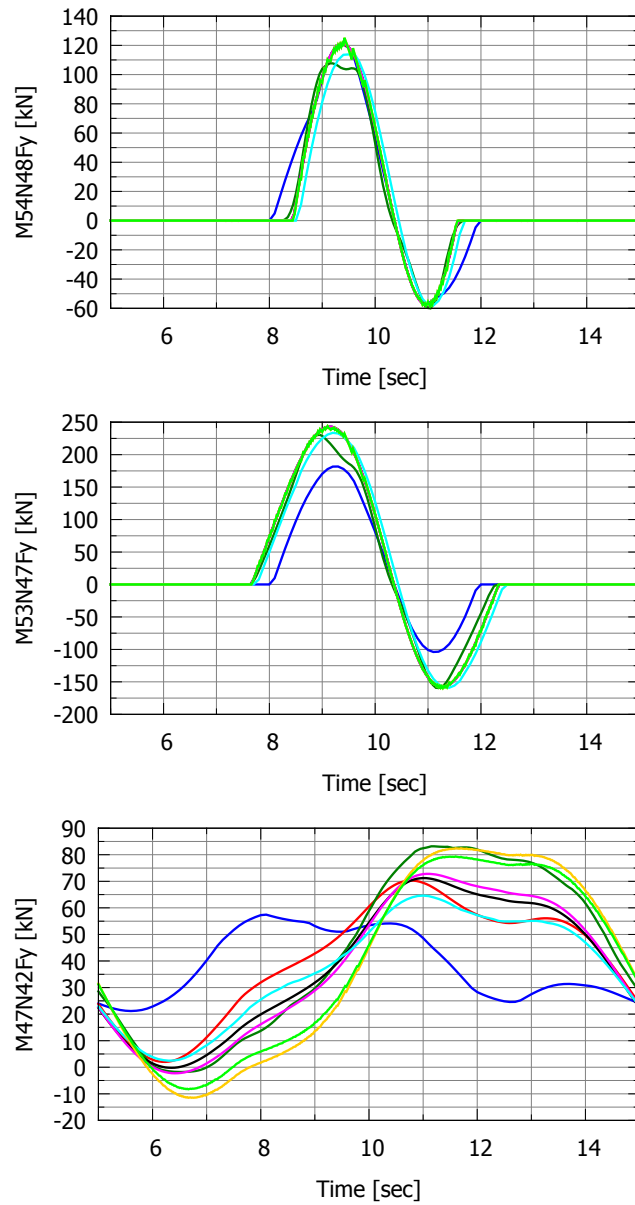
Figure 5.5: Fore-aft shear force at locations one to three (cf. Figure 5.2) for the rigid OWT under periodic wave loading (top to bottom). ADCoS-Offshore results are shown in red.
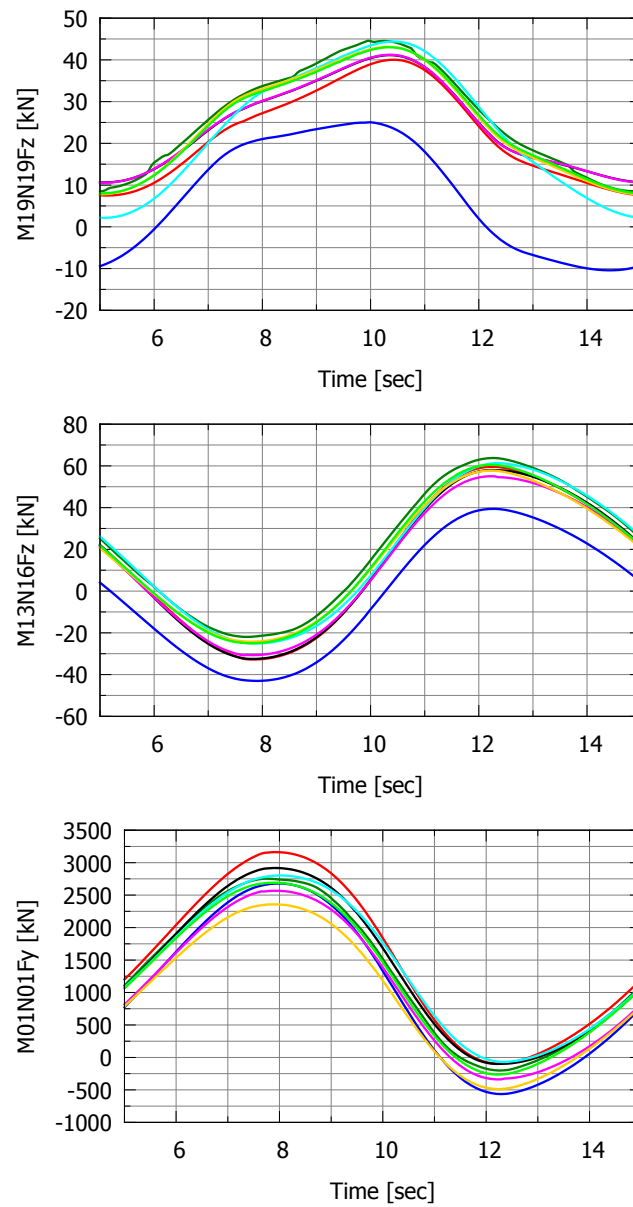
Figure 5.6: Fore-aft shear force at locations three to six (cf. Figure 5.2) for the rigid OWT under periodic wave loading (top to bottom). ADCoS-Offshore results are shown in red.
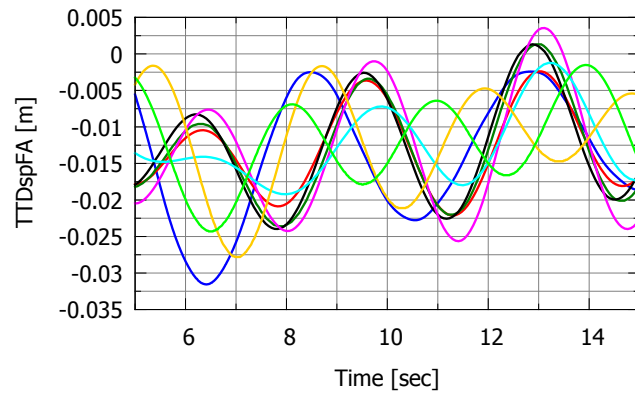
Figure 5.7: Tower-top fore-aft displacement for the flexible OWT under wave loads. ADCoS-Offshore results are shown in red.
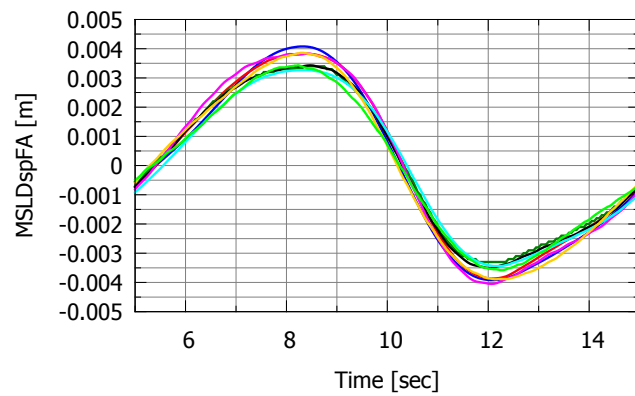
Figure 5.8: MSL fore-aft support structure displacement for the flexible OWT under wave loads. ADCoS-Offshore results are shown in red.
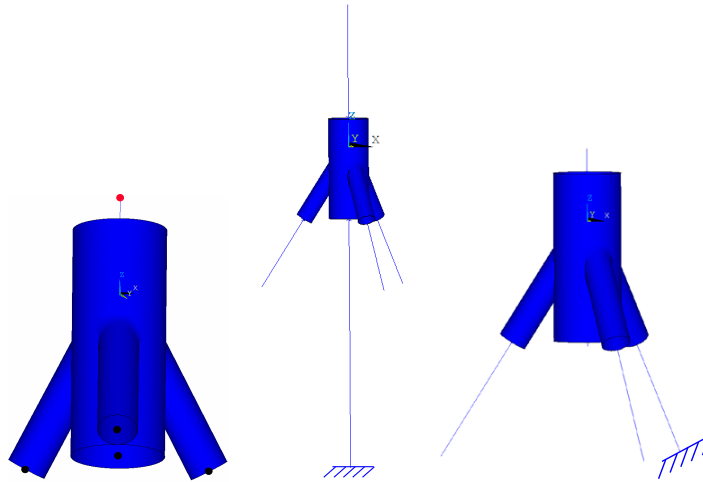
Figure 5.9: Tripod central joint models that are used for superelement stiffness matrix, mass matrix and load vector verification (from left to right). All three models are set up in ADCoS-Offshore and Ansys and the calculated results are compared.

The model is slightly modified for the mass matrix check (see Figure 5.9, middle). Supplementary beam elements with the tripod central column, tower and leg stiffnesses but with negligible masses are included. The model is cantilevered only at the lowest beam element node. The mass matrix is verified in terms of eigenfrequency results. The frequency values are the direct consequence of the stiffness distribution (already verified) and the mass distribution and are therefore suitable for this purpose. Furthermore, with the simplified model used here, it is confirmed, that the superelement has a large influence on the frequencies. The first ten eigenfrequencies are calculated and compared. All differences are very small and below $\Delta f_{\mathsf{max}} = 0.05\,\permil$.

The load vector verification is conducted as follows. The model as shown in Figure 5.9 (right) is defined with the central tripod joint, beam elements with the tripod member properties and an asymmetrically clamped support. External loading is not applied, but self weight is included in the simulation. Reaction forces and moments at the support are compared and the results are practically identical. The maximum difference has the same order of magnitude as for the frequencies.

The correctness of the wave loads on the superelement is firstly verified by comparing summarized force and moment results before and after the redistribution in simple spreadsheet calculations. In addition, a comparison of exemplary internal forces in the tripod in wave direction for the whole turbine under wave loads only is realized. The results time series are very close. This shows that the load application in ADCoS-Offshore is correct as well. To sum up, the simulation procedure including superelements in ADCoS-Offshore leads to the expected results and can be used for further investigations.

Chapter 6

Simulation results comparison for beam- and superelement models

In this chapter, simulation results for the tripod (Section 6.1) and the jacket (Section 6.2) are compared and interpreted. The outputs are called *sensors* in this chapter. The different structure types may lead to different approaches when it comes to details of the investigations such as for the positions where load effects are compared. Some supplementary tests are shown for one of the structures only and the results are transferred. As an example, the crosscheck of basic turbine functions is shown for the jacket only (cf. Section 6.2.3). All eigenfrequency analyses presented in this chapter are realized with damping and dead weight effects excluded.

6.1 Results for the tripod support structure

This section deals with the tripod structure. Basically, the beam model (see Section 4.3.2) and the superelement model (see Section 4.3.5) are compared, because these models represent the development in the aeroelastic modeling. The shell model (see Section 4.3.3) is used whenever it is reasonable to verify the results with a higher fidelity reference model (cf. Section 1.2) of the structure. See also Vorpahl et al. (2010) and Vorpahl and Reuter (2011) for investigations on tripod models.

6.1.1 Masses and frequencies

In a first step, the dead weights and the first 15 natural frequencies of the superelement model are compared with results for the shell-joint model as a plausibility check. The results are identical as described in theory (results not shown). The dead weights and eigenstates of the beam-, the superelement- and the shell support structure models are then compared, whereas the shell model serves as a reference. It is the model with the highest fidelity (cf. Section 1.2), and it has been verified extensively (cf. Section 4.3.3). Table 6.1 shows the total masses of the structures and the mass differences between the beam model and the shell model and between the superelement model and the shell model respectively.

The difference between the beam model and the shell model is Δm=2.6 %. This is due

Table 6.1: Dead weight of tripod support structure models and comparisons. The superelement model is compared with the shell model (3rd column) and with the beam model (4th column).

Beam [tons]	Super [tons]	Shell [tons]	Diff. beam – shell [%]	Diff. super – shell [%]
1113.3	1081.9	1084.6	2.6	-0.25
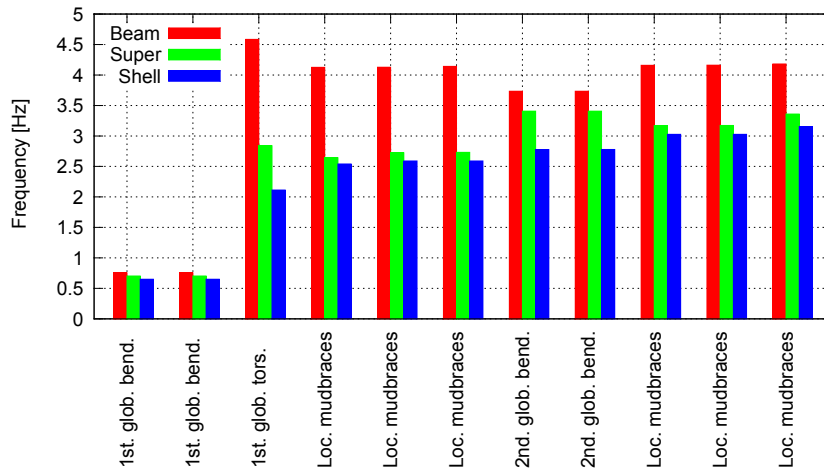
Figure 6.1: Eleven eigenfrequencies and mode shapes for the beam-, the superelement- and the shell tripod model.

to the calculation of the steel volumes at the joints, where the tripod members intersect and due to the conical parts of the joints. These are modeled with continuous changes in case of the shell joints and stepped in case of the beam joints. More detailed investigations on the mass difference show that the shell joints are approximately 10 % lighter than the beam joints, except the lower central joint, which is only 6 % lighter. The difference between the calculated masses using the superelement- and the shell model is very small ($\Delta m = -0.25\,\%$). It might result from modeling of the conical parts (stepped or continuously changing over member length) of the tripod structure (central column and tower) but this is not further investigated herein (see Section 4.3.2, Section 4.3.5 and Section 4.3.3 for the detailed modeling in all three cases).

Figure 6.1 shows eleven eigenfrequencies for the three support structure models and the respective mode shapes (global bending modes, a global torsional mode and local bending modes of a subset of members). For the shell reference model, the mode shapes are given in ascending order of the associated frequencies. The 12th mode shape calculated with the shell model cannot be described in the other models as it is a shell flattening mode (comparable to the mode shown in Figure 4.6 for a tower deformation mainly), therefore the highest mode compared here is the 11th mode. Some of the modes calculated with the superelement and the beam model, that are connected to frequencies lying very close together, *change places* (see Section 4.3.5 for an explanation of this subject.). For a better comparability of the frequencies of the respective mode shapes, the modes are assorted in the figure based on the mode shapes, not the frequencies. Figure 6.2 gives the frequency differences for the same mode shapes for the beam model and the superelement model, with respect to the shell model.

It is directly visible that the shell model leads to the lowest natural frequencies. The frequencies obtained with the superelement model are slightly higher, those obtained with
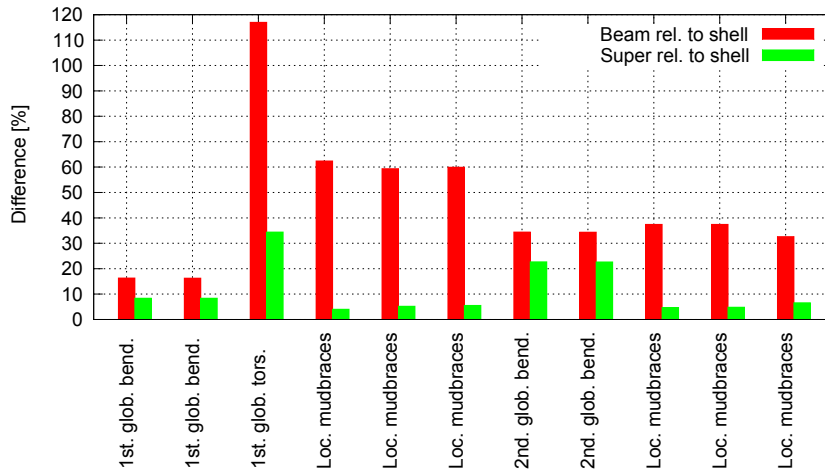
Figure 6.2: Frequency differences between tripod beam and shell model and between superelement and shell model.

the beam model are the highest. In general, significant differences occur especially for the beam model compared to the reference. The 1st global torsional frequency is more than doubled when comparing the beam model to the shell model (Figure 6.1, 1st global torsion). The differences are significantly reduced for all the modes, when moving from a beam to a superelement model. The superelement results for the bending modes are relatively close to the reference, expect for the two 2nd global bending modes shapes. For those mode shapes, the difference is reduced by about one third, when using a superelement model instead of a beam model (Figure 6.2, 2nd global bending). The differences for the, very important, first global bending modes are approximately halved (Figure 6.2, 1st global bending). The difference for the global torsion is reduced by about two thirds (Figure 6.2, 1st global torsion). But still, the remaining difference between the first global torsional frequencies for the beam- and the superelement model is $\Delta f_3 = 40\,\%$. All frequency differences associated with local bending modes of the mudbraces are strongly reduced.

Summing up, the mass difference between shell model and superelement model is negligible and therefore not further investigated. Comparing the masses of the beam model and the superelement model, differences were expected, as the beam model does not represent the steel surfaces at the intersection of members at the joints correctly as previously mentioned. The relatively small difference shows the good quality of the beam model with its massless members included at those intersections.

The eigenfrequencies are shifted towards lower values for the higher fidelity models, as expected. The differences between the beam model and the more sophisticated models are significant and the lowest eigenfrequencies shown here are important OWT design parameters. Compared to the beam model, the use of superelements moves all frequencies closer to the reference. The differences between the beam model results and the superelement model results are considerable, i.e. the enhancement when using superelements pays off. The shell model leads to an increase of computational effort that is not suitable for aeroelastic analyses.
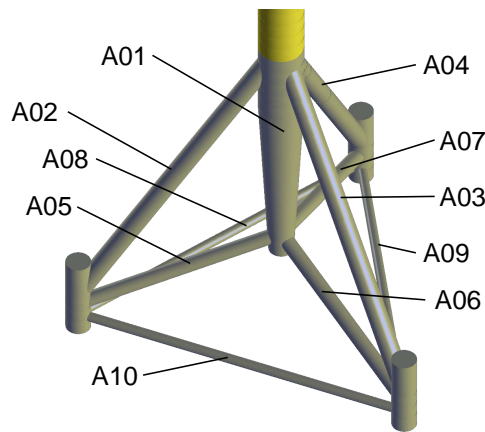
Figure 6.3: Positions for axial force comparisons in the tripod.

6.1.2 Static load distribution

The load bearing behavior of the beam- and the superelement model is compared using a static analysis based on the following outputs:

- Global tower top deflections.

- Summed reactions at mudline.

- Individual reactions at mudline (for the three legs).

- Axial forces in the tripod members.

The output positions and the respective naming convention are given in Figure 6.3. In comparisons, all results are related to the higher fidelity model, i.e. the superelement model.

As a further simplification, the models are not loaded externally in a first step (results not shown), which means that gravity, leading to a symmetric vertical load (F_z not resulting in moment components M_x and M_y), is the only load source. In this case, the only global deflection component at the tower top is u_z and the value of this deflection is very small. Therefore global deflections are not compared. As expected, the summed reaction forces at mudline are the same for both models except for F_z, where the mass difference described in Section 6.1.1 is visible. The summed moments are not equal and nonzero in both models, which is initially surprising. But the absolute values are small and this is explainable even in this *symmetric* loading situation. A nonzero value for M_x, for example, results from imbalances of $F_{y,i}$ and $F_{z,i}$ in the structure with the respective lever arms. The $F_{z,i}$ force components are large due to gravity and the lever arms for $F_{z,i}$ might be slightly different due to the number of digits used in the calculation to describe the nodal positions of the structure. The large $F_{z,i}$ values lead to nonzero moments when being multiplied even with very small lever arm differences in the respective models.

For the individual reactions for each leg at mudline, significant differences occur. For most of the forces and moments, the values are higher in the case of the beam model. This is the case for the horizontal reactions ($F_{x,i}$ and $F_{y,i}$) for which large differences are plausible: Pressure loads resulting from gravity (F_z) are transferred down the load path as axial forces in legs and braces to the pile sleeve joints. In the joints, a resulting force is pushing horizontally outwards (radially out of the tripod center). This component is

counteracted by tension in the mudbraces. Here, it becomes apparent, that the reaction at mudline depends directly on the (modeled) stiffness of the member. A more compliant mudbrace leads to reduced tension in the mudbrace, but to larger horizontal reactions at mudline. Furthermore, the modeling of the joint, i.e. the stiffness of the connection between pile sleeve and mudbrace becomes important.

Several of the axial forces $F_{x,A01}$ to $F_{x,A10}$ show large differences including changes of signs for the beam- and the superelement model. The beam model leads to pressure in the central column, the superelement model leads to a large tension ($F_{x,A01}$). The beam model tripod legs ($F_{x,A02}$ to $F_{x,A04}$) experience slightly higher tension than the legs in the superelement model. The braces ($F_{x,A05}$ to $F_{x,A07}$) show tension forces for the beam model (large values) and pressure for the superelement model (small values), for the mudbraces ($F_{x,A08}$ to $F_{x,A10}$) it is vice versa (beam model: moderate compression, superelement model: strong tension). This confirms the conclusions explained above, the load distribution differs strongly due to a changed local stiffness modeling.

The static turbine loads as described in Table 4.1 are applied on the two models in the next step and the outputs as described above are analyzed. The global tower top deflections in the relevant directions are given in Table 6.2.

Table 6.2: Tower top deflection and rotation components for tripod beam- and superelement model for the static load case in global coordinates.

Sensor	Beam [m] [°]	Super [m] [°]	Diff. [%]
u_x	0.411	0.455	-10
u_y	0.039	0.0416	-6.3
φ_y	0.392	0.419	-6.4

The absolute values are plausible, the fore-aft tower top deflection for example is $u_x \approx 0.5\,\mathrm{m}$, a realistic value for this turbine, structure and loading condition. The deflections for the beam models have lower values, the difference is approximately 10 % for the fore-aft deflection u_x and approximately 6 % for the side-to-dide deflection u_y and the fore-aft rotation φ_y. As expected, this means that the superelement model is globally more compliant.

Obviously, in the global (summed) reactions at mudline, the mass difference is found again; these results are as expected and not shown. Table 6.3 presents the mudline forces for the individual legs (upwind, downwind left and downwind right as described in Section 4.3.1).

Table 6.3: Mudline reaction forces for each tripod leg in the global CS.

Sensor	Beam [kN]	Super [kN]	Diff. [%]
$F_{x,L1}$	2286	1335	71
$F_{x,L2}$	-1510	-1034	46
$F_{x,L3}$	-1515	-1041	46
$F_{y,L1}$	-2.971	-3.230	-8.0
$F_{y,L3}$	-2667	-1816	47
$F_{y,L3}$	2670	1819	47
$F_{z,L1}$	2280	2201	3.6
$F_{z,L2}$	5973	5860	1.9
$F_{z,L3}$	6169	6053	1.9

All horizontal forces show large differences (between 46 % and 71 %) exept $F_{y,L1}$. However, the absolute value of $F_{y,L1}$ is small. All significant absolute values are higher for

the beam model. The values for the vertical forces are relatively close, the summed difference is the vertical force difference due to the different masses. As discussed above, the results indicate the global change of the load distribution in the tripod structure. The reaction moments show comparable results, i.e. partly large differences and larger load effects for the beam models for all components with a significant load magnitude (results not shown).

Table 6.4 gives the axial forces in the tripod members following the naming convention defined in Figure 6.3. Negative values are compressive forces here.

Table 6.4: Axial forces in tripod members.

Sensor	Beam [kN]	Super [kN]
$F_{x,A01}$	-460.9	101.1
$F_{x,A02}$	-262.8	-308.1
$F_{x,A03}$	-5311	-5268
$F_{x,A04}$	-5598	-5549
$F_{x,A05}$	-2461	426.7
$F_{x,A06}$	-613.8	444.2
$F_{x,A07}$	-467.9	422
$F_{x,A08}$	104.6	-1812
$F_{x,A09}$	161.2	29.09
$F_{x,A10}$	106.8	175.1

As expected, based on the results described above, the results calculated with the two models are very different. With the beam model, a large compressive force in the central column is obtained whereas the superelement model leads to a tension force with a much smaller value. Both models yield compressive forces in the legs, the value in the upwind leg is smaller for the beam model, while for the downwind legs, the values are slightly higher. The beam model leads to pressure in the braces ($F_{x,A05}$ to $F_{x,A07}$), the superelement model leads to tension at these positions. At $F_{x,A08}$, in the mudbrace, the beam model leads to pressure, the superelement model to a large tension. Relatively small pressures are calculated in both models for the remaining mudbraces. ($F_{x,A09}$ and $F_{x,A10}$).

In this section, the load bearing behavior of the beam- and superelement tripod models is investigated based on results from a static load case. For a better understanding of the system, an even simpler analysis with loads from dead weight only is performed in advance. Differences are large and therefore the use of the more accurate superelement model is reasonable. Conclusions are drawn in more detail as follows:

- The superelement model is – as expected – globally more compliant than the beam model, the difference in the relevant deflections is up to 10 %.

- For internal forces and moments with small absolute values, even very small modeling differences, or even the number of digits that are used internally in a software tool might lead to differences. These can be neglected, especially as the small loadings do not always lead to a better understanding of the structural behavior and more important, because they are not relevant for a design.

- Even for very simple loading conditions, i.e. only structural mass, internal forces and moments might differ significantly. The horizontal reactions at mudline for example are significantly higher for the beam model. This is a plausible result, even if it is not intuitively understandable.

- For the axial forces in the tripod members, similar load distribution patterns are visible in the load case with structural mass only and the load case including the
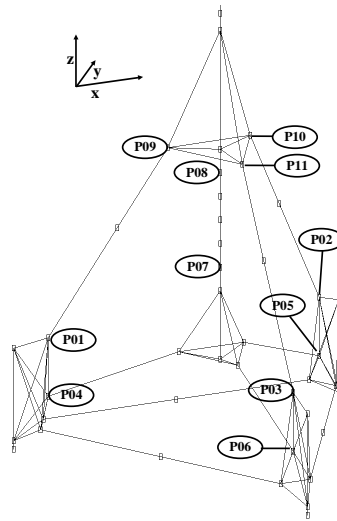
Figure 6.4: Tripod output positions for DEL comparisons.

tower top loads. The load bearing behavior of the beam- and the superelement model, however, are totally different. This results from the different stiffnesses of the joints that significantly influence the load path through the structure. The differences due to this effect are surprisingly high.

6.1.3 Fatigue and extreme results

Extreme and fatigue loads simulation results are presented in this section[1]. To perform the simulations, the turbine and two tripod models (beam- and superelement models) are defined in ADCoS-Offshore. The load case set is defined in Section 4.1.3. Herein, a set of DEL in the tubular members of the structure in proximity to the joints are compared. DEL results are important at these positions because these DEL are in general used in joint design. Therefore the output positions are selected as shown in Figure 6.4. (And that is why these outputs are different to the axial force outputs that were used in Section 6.1.2 to describe the global static load bearing behavior.) Tower top, tower base outputs and outputs at positions $P07$ and $P08$ are given in global coordinates. The local (element) CS is used for $P01$ to $P06$ and $P09$ to $P11$. The x-axis points away from the closest joint for all outputs in local coordinates.

Table 6.5 shows the tower top displacement extremes for the beam- and the superelement models for all simulated load cases. Values close to zero are not shown.

All deflection extremes are larger for the superelement model, the differences are between $\Delta u_{\text{min}} = 5.6\,\%$ and $\Delta u_{\text{max}} = 51.4\,\%$. Differences are significant for deflection directions with large absolute values like $\Delta u_{\text{x, max}} = 10.2\,\%$ in mean wind direction or $\Delta \varphi_{\text{x, max}} = 14.1\,\%$ around the axis where the structure counteracts the mean rotor moment. The largest differences are found for the rotation around the vertical axis. Larger deflections for the more compliant (see e.g. Section 6.1.2) superelement model were to be expected. The rotation around the vertical exhibiting the largest differences fits to the former finding of the difficulty in capturing the torsional behavior of the tripod structure in the simpler beam model (see e.g. Figure 6.2).

---

[1]The extreme loads are obtained under operational conditions, because extreme load cases in the sense of extreme DLCs are not simulated as described in Section 4.1.

Table 6.5: Global extreme values for tripod tower top deflections from beam- and superelement model in global coordinates. Outputs with small absolute values are not shown.

Sensor	Beam [m]	Super [m]	Diff. [%]
$u_{x, max}$	0.503	0.560	-10.2
$u_{y, min}$	-0.262	-0.323	-18.9
$u_{y, max}$	0.121	0.166	-27.1
$u_{z, min}$	-0.012	-0.022	-44.9
$u_{z, max}$	-0.011	-0.020	-46.0

Sensor	Beam [°]	Super [°]	Diff. [%]
$\varphi_{x, min}$	-0.094	-0.129	-27.1
$\varphi_{y, max}$	0.474	0.502	-5.6
$\varphi_{z, min}$	-0.228	-0.458	-50.2
$\varphi_{z, max}$	0.228	0.469	-51.4

The following Table 6.6 gives extreme load effects at the tower base. Again, only significant values are shown.

Table 6.6: Extreme values of tower base load effects for the tripod beam- and superelement model in the global CS.

Sensor	Beam [kN]	Super [kN]	Diff. [%]
$F_{x,max}$	866	876	-1.14
$F_{y, min}$	-417	-484	-13.84
$F_{y, max}$	315	351	-10.26
$F_{z, min}$	-7,078	-7,081	-0.04
$F_{z, max}$	-6,741	-6,719	0.33

Sensor	Beam [kNm]	Super [kNm]	Diff. [%]
$M_{x, min}$	-19,893	-23,274	-14.53
$M_{x, max}$	36,867	41,132	-10.37
$M_{y, max}$	72,506	71,988	0.72
$M_{z, min}$	-8,341	-8,026	3.92
$M_{z, max}$	8,541	7,774	9.87

$F_{x, max}$, $F_{z, min}$, $F_{z, max}$ and $M_{y,max}$ show relatively small differences. The forces in y-direction and the associated bending moment around the x-axis are higher for the superelement model. Torsional load effects in the tower are reduced when the superelement model is used which is reasonable due to the decreased rotational stiffness.

In the following, DELs are compared. The shear forces for all output positions ($P01$ to $P11$) are found to be very small in general compared to the other values and are not shown here. In Table 6.7 results for $P01$ to $P06$ are shown. These are the positions in the tubular members close to the pile sleeve joints.

The table shows large differences for some of the sensors. For $M_{y,P05}$, the difference is close to a factor of four. The sensors that exhibit reduced load effects for the superelement model are numerous and these are the sensors that show the largest differences. This is the case for $M_{x,P01}$, $M_{x,P02}$, $M_{x,P03}$, $M_{z,P04}$, $M_{y,P05}$ and $M_{y,P06}$. Some of the sensors show an increase, and the respective values might have significant absolute values (see $M_{y,P01}$, $M_{z,P03}$, $M_{x,P04}$ and $M_{x,P06}$).

Table 6.8 presents results for $P07$ and $P08$ in the central column of the tripod. The results for these sensors show a smaller spread than the results of Table 6.7. The largest dif-

Table 6.7: DEL results for tripod output positions $P01$ to $P06$ in the respective local (element) CS.

Sensor	DEL Beam [kN] [kNm]	DEL Super [kN] [kNm]	Diff. [%]
$F_{x,P01}$	244.64	212.78	15
$M_{x,P01}$	89.389	49.135	81.9
$M_{y,P01}$	312.45	396.04	-21.1
$M_{z,P01}$	307.4	210.99	45.7
$F_{x,P02}$	200.97	173.68	15.7
$M_{x,P02}$	91.846	51.948	76.8
$M_{y,P02}$	274.61	196.16	40
$M_{z,P02}$	346.99	393.23	-11.8
$F_{x,P03}$	173.19	164.59	5.2
$M_{x,P03}$	103.21	51.175	101.7
$M_{y,P03}$	180.76	194.78	-7.2
$M_{z,P03}$	261.7	358.98	-27.1
$F_{x,P04}$	87.673	76.141	15.1
$M_{x,P04}$	56.321	101.77	-44.7
$M_{y,P04}$	37.966	35.284	7.6
$M_{z,P04}$	191.6	86.494	121.5
$F_{x,P05}$	75.869	61.41	23.5
$M_{x,P05}$	52.897	105.31	-49.8
$M_{y,P05}$	210.03	63.495	230.8
$M_{z,P05}$	46.961	39.377	19.3
$F_{x,P06}$	61.272	57.283	7
$M_{x,P06}$	50.541	99.14	-49
$M_{y,P06}$	96.974	54.178	79
$M_{z,P06}$	43.816	36.342	20.6

Table 6.8: DEL results for tripod output positions $P07$ to $P08$ in the global CS.

Sensor	DEL Beam [kN] [kNm]	DEL Super [kN] [kNm]	Diff. [%]
$F_{x,P07}$	108.83	101.48	7.2
$M_{x,P07}$	347.18	394.34	-12
$M_{y,P07}$	504.42	538.33	-6.3
$M_{z,P07}$	643.04	641.06	0.3
$F_{x,P08}$	99.513	96.261	3.4
$M_{x,P08}$	1160.7	1216.5	-4.6
$M_{y,P08}$	1660.9	1636.5	1.5
$M_{z,P08}$	614.23	585.63	4.9

ference is found for the torsional moment $M_{x,P07}$ where the superelement model leads to a higher DEL.

Results for the sensors in the tripod legs close to the central joint ($P09$ to $P11$) are provided in Table 6.9. These are comparable to the results for sensors $P01$ to $P06$.

Table 6.9: DEL results for tripod output positions $P09$ to $P11$ in the respective local (element) CS.

Sensor	DEL Beam [kN] [kNm]	DEL Super [kN] [kNm]	Diff. [%]
$F_{x,P09}$	242.93	212.33	14.4
$M_{x,P09}$	88.94	52.008	71
$M_{y,P09}$	324.03	481.61	-32.7
$M_{z,P09}$	189.97	137.9	37.8
$F_{x,P10}$	199.02	173.35	14.8
$M_{x,P10}$	91.339	54.914	66.3
$M_{y,P10}$	173.88	197.13	-11.8
$M_{z,P10}$	323.25	463.86	-30.3
$F_{x,P11}$	172.48	164.35	4.9
$M_{x,P11}$	102.75	53.675	91.4
$M_{y,P11}$	143.65	198.09	-27.5
$M_{z,P11}$	270.46	429.69	-37.1

Here as well, the differences are large, in most of the cases the load effects decrease with the superelements, but not in all the cases. The largest differences occur for $M_{x,P09}$, $M_{x,P10}$ and $M_{x,P11}$, the torsional moments. Important bending moment values ($M_{y,P09}$, $M_{z,P10}$, $M_{y,P11}$ and $M_{z,P11}$) show significant increases of the load effects when superelements are used.

In summary, the following is stated: Using superelements, the DEL near the joints may be reduced because the joints are modeled more compliant. However, in Section 6.1.2 it is shown for static load cases, that the load bearing behavior of the two tripod models is different, i.e. the global load distribution pattern changes when superelements are used. This is confirmed here and leads to the fact of DELs (especially those of the bending moments) being shifted towards larger values, too.

This implies that the global load distribution pattern in the tripod is sensitive to relatively small stiffness changes in single members (or joints), a conclusion that is coherent to the results given in Vorpahl et al. (2013). In this paper, the sensitivity of the tripod's load bearing behavior is described as well. Although the stiffness differences are due to the beam formulation (EB beam elements vs. Timoshenko-like beam elements) and not due to the joint definition, the resulting load effects are comparable. In Klausmann et al. (2012) it is shown that the beam model with Timoshenko beams even leads to results close to a shell model for the investigated combination of load cases and structure.

Due to the large differences between the results obtained with beam- and superelement models, the use of superelements when performing loads analyses of tripods is strongly recommended.

6.2   Results for the jacket support structure

In this section, results for the jacket models are compared and conclusions are drawn. The beam model (see Section 4.4.2) and the superelement model (see Section 4.4.5) represent the current development in aeroelastic modeling and therefore these two are mainly compared. The shell model (see Section 4.4.3) is used as a reference, whenever is is possible and useful to verify the results with a higher fidelity model of the structure.
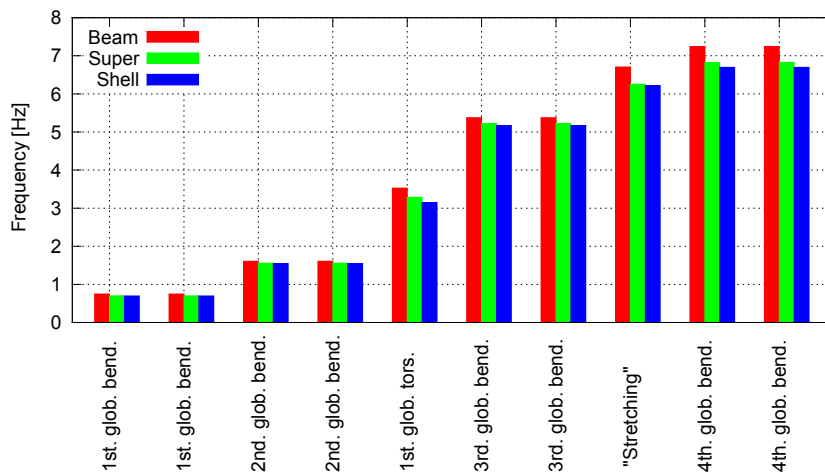
Figure 6.5: Eigenfrequencies and mode shapes for the beam-, the superelement- and the shell jacket model.

See also Tu (2013) and Tu and Vorpahl (2014) for more investigations on the jacket structure.

6.2.1 Masses and frequencies

The shell-joint model (Section 4.4.4) and the superelement model (Section 4.4.5) by definition lead to the same results in terms of masses and stiffnesses, and therefore also eigenfrequencies. This is verified successfully as a first plausibility check (results not shown). Table 6.10 gives the steel masses for the beam model, the superelement model and the shell model and comparisons between the superelement model and the two other models.

Table 6.10: Dead weight of jacket support structure models and comparisons (beam model vs. shell model and superelement model vs. shell model)

Beam [tons]	Super [tons]	Shell [tons]	Diff. beam – shell [%]	Diff. super – shell [%]
1489.3	1438.8	1438.5	3.53	0.02

The mass difference between the superelement model and the shell model is very small and not further investigated. The overestimation of the mass in the beam model compared to the shell model ($\Delta m = 3.53\,\%$) is mainly due to the overlapping at the joints. This is a result of the use of the simple beam model including overlapping parts as described in Section 4.4.2.

In Figure 6.5, eigenfrequencies for the three support structure models and the respective mode shapes are shown. These are global bending modes, the first global torsional mode and a vertical stretching of the structure.

The ordering of the mode shapes differs for the different models (cf. Section 4.4.1 for a description of this phenomenon). Hence, the modes corresponding to the first ten mode shapes of the beam model and the superelement model need to be selected amongst the first 15 modes of the shell structure. In general, the higher fidelity models show lower eigenfrequency values. The results for the superelement model are closer to the reference, some results of the beam model are far off. In Figure 6.6 this is pointed out in more
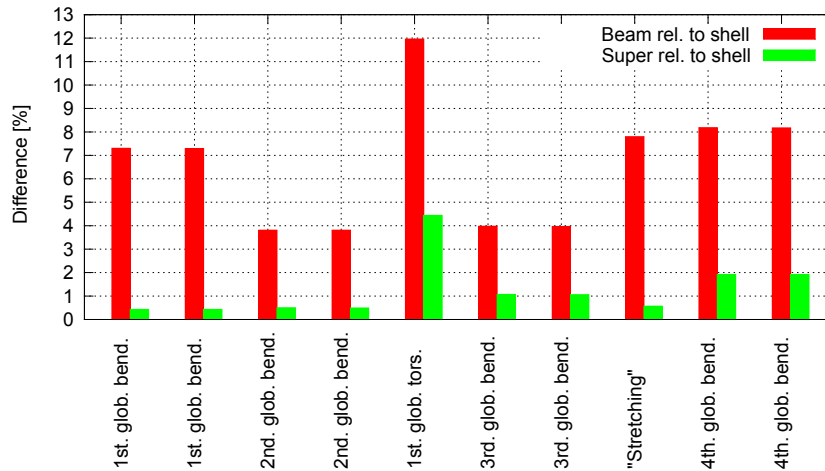
Figure 6.6: Frequency differences between jacket models. Beam and shell model as well as superelement and shell model are compared.

detail via comparison of the frequency differences instead of the absolute values.

Here, the proximity of the superelement results to the reference results becomes even more obvious. For the first four modes – the 1st and 2nd global bending modes of the structure – the differences between superelement and shell element results are below Δf=0.5 %, and therefore almost negligible. For the last five modes shown here, the augmentation of the results due to the superelements is very clear. The 5th mode shape is the 1st global torsional mode. To predict the torsional frequencies accurately, higher fidelity models than for the bending modes are necessary (cf. Section 4.3.3 and Section 4.4.3 also). However, for this frequency, the difference to the reference is still more than halved when using superelements.

In summary, the superelement model is a very good approximation of the shell reference for both, mass and eigenfrequencies, keeping the computational effort for aeroelastic simulation at a reasonable level. In terms of dead weight, the small mass differences between the beam model and the shell model can be traced back to the modeling of the structure (doubled members at joints). The higher fidelity superelement and shell models are generally more compliant, which is reflected in the eigenfrequencies. The differences between the superelement model and the shell reference model are very small for the important 1st and 2nd global bending modes. For higher modes (5th to 10th), the reduction of the error with respect to the reference is significant for the superelement model. Even for the torsional mode – that is harder to predict accurately – the error reduction is more than 50 %. The differences are smaller than for the tripod (see Section 6.1.1), but still, the use of the superelement is reasonable. The frequencies are shifted towards more realistic values, and the differences are significant for a subset of frequencies.

6.2.2   Static load distribution

For a better understanding of the load bearing behavior of the jacket structure, static analyses are conducted. In this respect, the following outputs are compared: The global displacement pattern, tower top deflections, summed as well as individual reactions at mudline and axial forces in a set of individual jacket members.

The static loads that are used herein – superimposed or single load components, depending on the respective investigation – are given in Section 4.1.2. In all comparisons, the results are related to the superelement model that is the higher fidelity model.

The first step is a comparison of the global displacement pattern under external static load for the beam- and superelement jacket models (results not shown). This is realized for the different combinations of load components and the resulting displacement components are evaluated based on visual checks. Similar displacement patterns are generally found. As an example, a vertical loading at the tower top leads to an outward deflection of the jacket legs due to the compressive loads. The horizontal deflection is increasing from the TP down to the K3 level and then decreasing from the K3-level to mudline. The displacement pattern is the same for both models. The maximum values are higher for the beam model and have absolute values of $u_{\text{x,max}} \approx 0.5\,\text{mm}$.

This displacement pattern is plausible due to the following: The load direction in combination with the inclined jacket legs – that are carrying the main load – lead to the outside bending of the structure over K3 on the one hand. The constrained DOFs at the legs at mudline level on the other hand impose a decreasing deflection below K3 ending up with zero deflection at mudline. The zero deflection at mudline is a modeling constraint in both models that might be discussed. However, for the purpose of model comparison it is reasonable. The absolute deflection values are plausible for this type of structure and load. In terms of model comparison, it is stated, that the beam model is suitable for jacket representation in terms of global deflections under static loads. It leads to results that compare well to the results obtained with the higher fidelity superelement model.

In a second step, the tower top deflections are compared. Here as well, the loads are applied consecutively and superimposed. It is verified, that the general structural behavior is both, similar (beam and superelement modeling results lead to comparable results) and reasonable (based on simple static considerations for a jacket structure). As an example, Table 6.11 shows the tower top deflections in global coordinates for both models loaded with all six static load components – and the respective differences.

Table 6.11: Tower top deflections under static loading for the jacket beam- and superelement model in global coordinates.

Sensor	Beam [m]	Super [m]	Diff. [%]
u_x	0.442	0.478	-8
u_y	-0.048	-0.050	-4
u_z	-0.0112	-0.0126	-11

The superelement model is more compliant than the beam model, all deflections for the superelement model are larger (negative percentages in Table 6.11). The differences are not excessive. However, the maximum difference is $\Delta u_z = 11\,\%$ which is not negligible.

A comparison of summed reactions at mudline (three constrained translational DOFs) leads to the expected results: The sums for each component are equal to the applied loads including the gravity load. Due to the latter, the summed vertical component F_z is 3 % higher for the beam model which is due to the extra weight of the overlapping members as described in Section 4.4.2 (results not shown).

Table 6.12 shows the reaction forces for the jacket legs at mudline with six load components applied at the tower top. The leg numbering is defined in Table 4.9.

It is obvious that there are large differences in the results. The load effects along the x-axis resulting from the simulations with the beam model show similar results for all the legs. This type of symmetry in the results does not exists for the superelement model. In the case of the superelement model, the absolute values for leg two and leg three

Table 6.12: Reaction forces at mudline in global coordinates for jacket legs with static load components applied at the tower top (six load components). In case of a direction change (d.c.) of the load effect, no percentage is given.

Sensor	Beam [kN]	Super [kN]	Diff. [%]
$F_{x,L1}$	-191	-150	27
$F_{y,L1}$	0.88	82	-99
$F_{z,L1}$	8610	8486	1
$F_{x,L2}$	-181	-222	-18
$F_{y,L2}$	-8.94	-4.67	91
$F_{z,L2}$	75.7	-48.5	d.c.
$F_{x,L3}$	-180	-225	-20
$F_{y,L3}$	7.9	3.6	118
$F_{z,L3}$	444.7	320.4	39
$F_{x,L4}$	-188	-144	31
$F_{y,L4}$	1.7	-79	d.c.
$F_{z,L4}$	8979	8855	1

($F_{x,L2}= -222\,\mathrm{kN}$, $F_{x,L3}=-225\,\mathrm{kN}$) are higher than for the leg with the highest reaction obtained with beam models ($F_{x,L1}=-191\,\mathrm{kN}$). A clear pattern in all the reaction components is not visible immediately, conclusions cannot be drawn directly. Additional results, obtained by applying the load components consecutively (results not shown here), show at least a pattern that fits to the geometry of the jacket and its symmetries.

Axial forces in the jacket structure (center of each leg and brace member) are compared in the same way with all load components applied consecutively. The loads being transferred down the structure are distributed to the legs and braces. As expected, the legs carry the main load. In cases of a larger axial force in a leg for the beam model in comparison to the superelement model, the respective force in the corresponding brace members is smaller and vice versa. Percentagewise, the differences are larger for the braces but these show smaller absolute values. These differences are not surprising when taking into account that the loads are shared between legs and braces (cf. above) and a difference in the load distribution leads to a small percentagewise difference for the large force in the leg and a high relative difference in the small force in the brace.

To get a clearer picture of the structural behavior and the differences due to modeling, the load path through the structure is analyzed. As an example, load effects close to mudline and reactions at mudline under the vertical tower top pressure component F_z are discussed. The vertical load leads to pressure in the jacket legs. Due to the inclination of the legs, this leads to a horizontal force component pushing the legs outwards with respect to the vertical centerline of the jacket at the level of the double-T-Joint at the jacket bottom. This deformation is counteracted by the mudbraces, resulting in tension in the mudbraces. The supporting effect of the mudbrace combined with the applied vertical load pushes the leg towards the jacket centerline. With the constrained DOFs at mudline, this leads to an outward reaction force at the bearing points.

One horizontal reaction at mudline and the axial tension in the respective mudbrace are shown in table 6.13 (only a vertical load is applied, therefore the loading is symmetric, i.e. the values shown here are the same for each pair of reaction and brace). Both values are higher for the more compliant superelement structure. Large differences for the load effects in braces and leg members are found for other joints too (results not shown here).

Summing up, the beam and the superelement model show the same global displacement behavior. As expected and as already shown earlier by the eigenfrequency analyses in Section 6.2.1, the superelement model is more compliant. For the tower top displacement under realistic static loading this leads to a maximum difference of $\Delta u_x = 11\,\%$.

Table 6.13: Horizontal reaction and axial force in a mudbrace for beam and superelement models.

Sensor	Beam [kN]	Super [kN]
Horizontal reaction	13	97
Axial force mudbrace	467	532
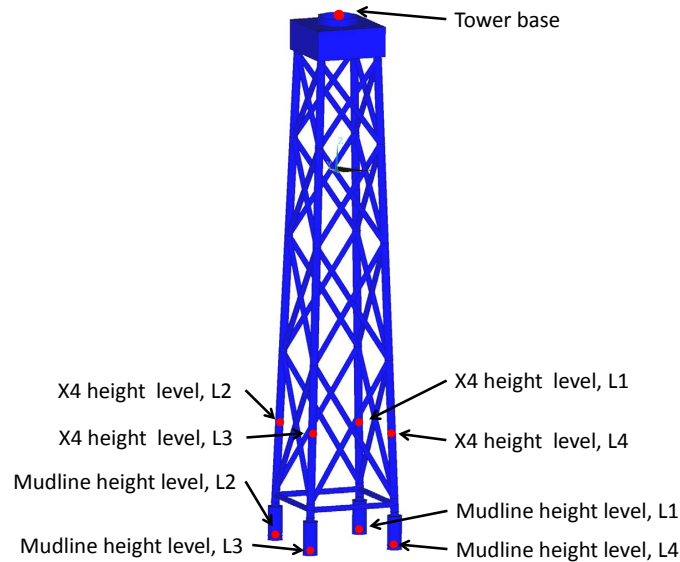
Figure 6.7: Jacket positions where outputs are compared. The supplementary output positions tower top and blade root are not shown.

Despite these relatively small differences in the global behavior, the load distribution in the jacket, i.e. the load shares in the individual members differ strongly. This can lead to higher load effects for important outputs such as the maximum horizontal reaction in mean wind direction at mudline (see Table 6.12). The results are plausible and coherent with the general behavior of a jacket and basic static considerations. However, the differences are large, the load bearing behavior is changed, even if this is not obvious when global effects only are investigated. Therefore, the use of superelements is a reasonable approach.

6.2.3 Fatigue and extreme results

In this section, extreme and fatigue loads simulation results for the turbine atop the jacket support structure simulated in ADCoS-Offshore are presented[2]. These are compared and the respective conclusions are drawn. The jacket structure is modeled with beam- and superelements respectively. See Section 4.1.3 for the detailed definition of the load case set. Further output positions are the tower top and the blade root as well as the jacket sensors given in Figure 6.7.

In a first step, the general turbine behavior is crosschecked and a preliminary plausibility check is conducted based on time series and basic turbine outputs. Figure 6.8, Figure 6.9 and Figure 6.10 show exemplary results.

---

[2]The extreme loads are obtained under operational conditions, because extreme load cases in the sense of extreme DLCs are not simulated as described in Section 4.1.
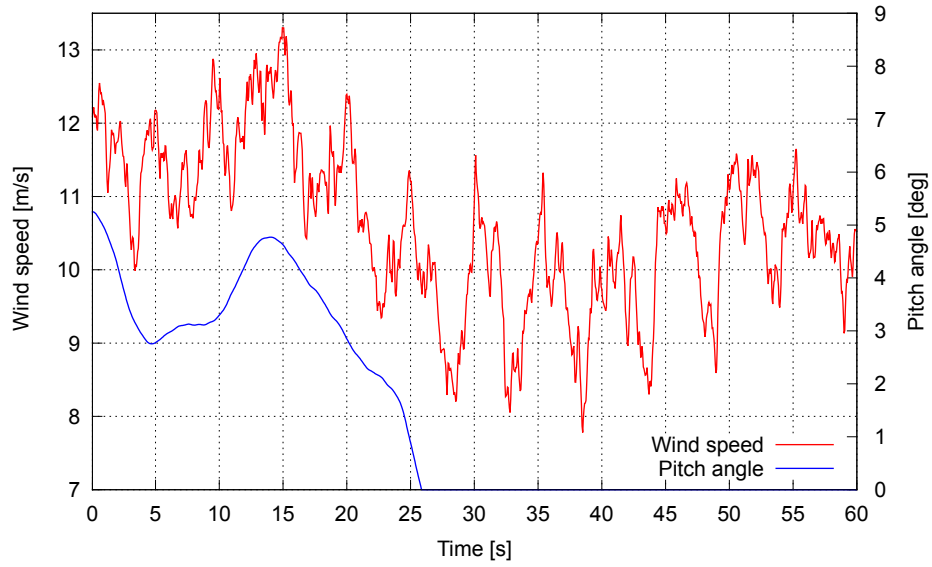
Figure 6.8: Wind speed at the blade and pitch angle over time for the jacket beam model.
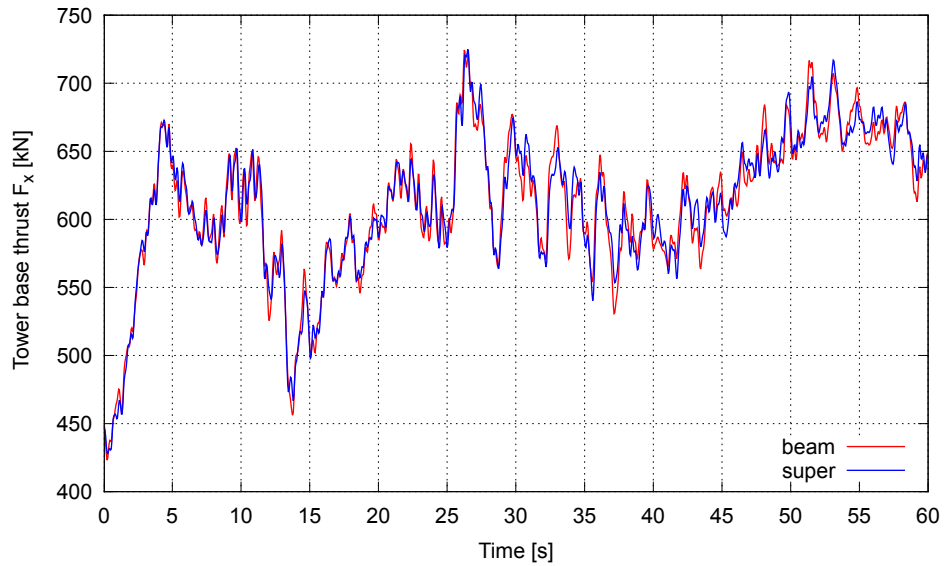
Figure 6.9: Tower base thrust forces over time for the jacket beam- and the superelement model.
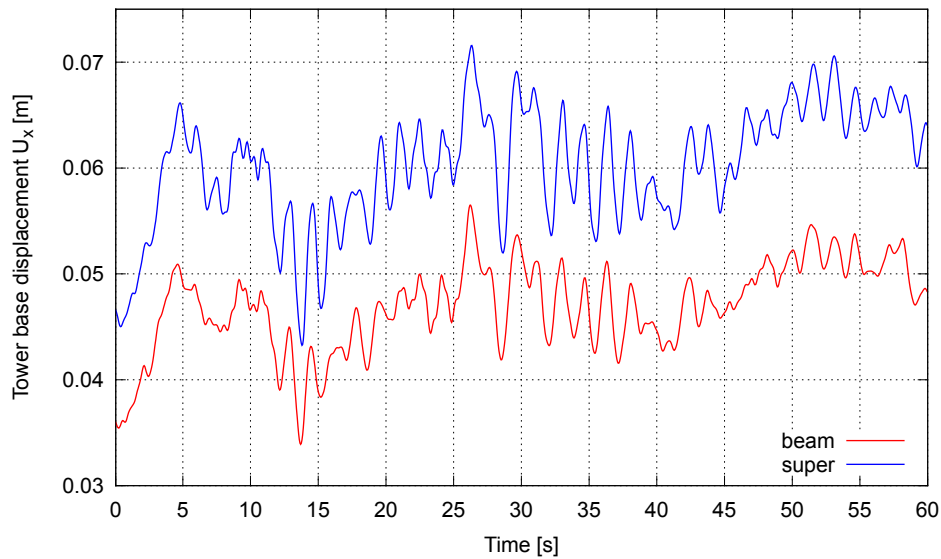
Figure 6.10: Tower base deflections over time for the jacket beam- and the superelement model in the global CS.

These results are a subset of a load case with an average wind speed close to rated speed ($V_w = 12\,\mathrm{m/s}$) with yaw misalignment ($\beta = -8\,^\circ$). See Table 4.2 and Table 4.3 for the load case description. This is a random sample from a load cases at the turbine's rated wind speed where the maximum of the rotor thrust force (being a function of the wind speed) is activated and where the pitch control becomes active. Figure 6.8 shows the wind speed at one of the blades and the pitch angle over 60 seconds for the beam model only. The wind speed is slightly over the rated wind speed for the first 25 seconds in short time average, therefore the pitch angle is set to positive values between zero and 9.25 $^\circ$. For the remaining time period the pitch angle is set to zero because of the short term average wind speed being lower then the turbine's rated wind speed. The turbine is operating as expected. In Figure 6.9, tower base thrust forces along the global x-axis for the beam- and the superelement model are presented. The general evolution of the curve is in accordance with the results shown in Figure 6.8, i.e. the thrust force increases with decreasing pitch angle in the non-zero pitch region and the thrust force increases with increasing wind speed in the zero-pitch region. Moreover and as expected, the beam and the superelement models show very similar results, because the external load is identical and the load effects differ slightly due to the small differences in the dynamic behavior of the two models. This effect has a minor influence on the total results at this output position only.

Figure 6.10 shows the tower base deflections for the beam- and the superelement model for the same time period. The global evolution of the curve is obviously similar. There are two differences: First, the high frequency oscillations somewhat differ due to the differences in the dynamic behavior of the two models. See for example the time period between 15 and 20 s. Second, and more important in terms of the visible results difference, the deflections for the superelement model are larger because it is generally more compliant. The difference is approximately $\Delta u_x = 20\,\%$.

Time series of vertical reactions at mudline and axial forces at the X4 level show a reasonable pattern for the given loading and only small differences for the beam- and the superelement model. These differences can be traced back to the modeling (mass difference). Tower top loads effects and blade root bending moments are compared in
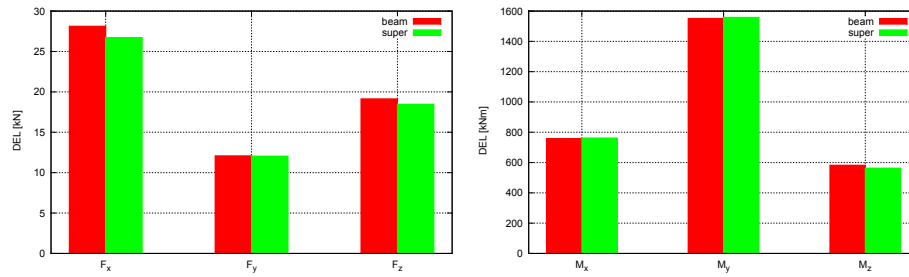
Figure 6.11: Tower base DEL for the jacket beam- and the superelement model for all DOFs in global coordinates.

terms of time series, mean values and DEL. As expected, the differences obtained with the beam- and the superelement model are very small (results not shown).

Summing up, the turbine is operating as expected, the external loads are similar, selected load effects at the tower top and the blades are nearly the same and the tower base deflection time series slightly differ due to different dynamic behavior of the models. The most important difference are the larger deflections due to the globally more compliant superelement model. These results substantiate the proper turbine definition and confirm former findings concerning the influence of the beam- and superelement models.

In the next step, post processed results from all simulated load cases (cf. Section 4.1.3) are considered. The global mean values of the tower base load effects (all DOFs) show only minor differences (results not shown). In Figure 6.11, tower base DEL are presented.

The DEL are similar as well and there is no clear tendency as to the influence of the modeling: the DEL of the forces are slightly decreased for the superelement model (for F_y the difference is very small). The DEL of the moments are increased except the torsional moment M_z. Results of a brief investigation of the tower base deflections (in terms of means and standard deviations) show again that the superelement model is more compliant (results not shown).

Table 6.14 and Table 6.15 show the mean values of reaction forces in the main load direction (F_x) at mudline and the respective DEL. The tower base thrust values (average and DEL) are verified to be almost the same in both models to make sure that occuring differences only result from the jacket modeling and not from differences in the applied external wind loading (not shown here).

Table 6.14: Mean values of the reactions in x direction (global CS) at mudline for jacket leg 1 to leg 4.

Sensor	Mean Beam [kN]	Mean Super [kN]	Diff. [%]
$F_{x,L1}$	-118.5	-78.8	50
$F_{x,L2}$	-116.6	-158.3	-26
$F_{x,L3}$	-86.5	-129.5	-33
$F_{x,L4}$	-87.1	-42.5	105

The mean values differ strongly while the DEL show smaller differences, i.e. the vibration patterns seem comparable, but the load effects fluctuate around different mean values.

The mean values (cf. Table 6.14) resulting from the simulations with the beam model show very similar results for the legs one and two (positive y coordinate) and for the legs three and four (negative y coordinate) respectively. This symmetry in the results does not

Table 6.15: DEL of the reactions in x direction at mudline for jacket leg 1 to leg 4 in global coordinates.

Sensor	DEL Beam [kN]	DEL Super [kN]	Diff. [%]
$F_{x,L1}$	30.5	33.8	-10
$F_{x,L2}$	30.5	33.6	-9
$F_{x,L3}$	28.6	32	-10
$F_{x,L4}$	28.6	32	-10

exists for the superelement model. This finding is also confirmed with time series control samples (results not shown here). For the superelement model, the average value for leg two ($F_{x,L2}$=$-158.3\,\mathrm{kN}$) is significantly higher than for the highest loaded leg from the beam model ($F_{x,L1}$=$-118.5\,\mathrm{kN}$).

All DEL are larger for the superelement model, i.e. the more compliant model leads to larger DEL at the constrained bottom of the structure. However, the differences are much smaller here than for the mean values. The maximum difference is ΔF_{max}=$10\,\%$. Similar axial force patterns are found in the jacket members at higher levels as well as for the z component at mudline.

In Table 6.16, extreme values of tower top deflections from all fatigue load cases are shown (results with very small absolute values and rotational deflections are not compared).

Table 6.16: Global extreme values for tower top deflections. Results from the beam- and superelement jacket models are compared. (All values shown in global coordinates, outputs with small absolute values not shown).

Sensor	Beam [m] [°]	Super [m] [°]	Diff. [%]
$u_{\mathrm{x,\,max}}$	0.49	0.53	-8
$u_{\mathrm{y,\,min}}$	-0.19	-0.17	7
$u_{\mathrm{y,\,max}}$	0.12	0.11	12

The table shows differences up to $\Delta u_{\mathrm{y,\,max}}$=$12\,\%$. Some of the deflections are larger for the beam model, others for the superelement model. The latter is interesting, because globally, larger deflections might be expected for the more compliant superelement model. When looking closer at the results (and when looking into more results than shown here), it is found that in case of larger deflections resulting from the beam model, the extreme values result from different time domain simulations and also from different points in time for each model. For the expected results (larger deflections for the superelement model, e.g. $u_{\mathrm{x,\,max}}$), the values originate from the same simulation at time steps being very close. Based on this observation, the following is stated. The globally more compliant superelement model does not lead to larger tower top deflections in all DOFs for the investigated set of load cases. The differences in the deflections are not very large. In case of larger deflections for the more compliant superelement structure, this corresponds to the expected results. In case of larger deflections for the stiffer structure, this might be a result of the different dynamic behavior, i.e. the combination of stochastic external loading with a highly dynamic system. These effects are not further investigated herein.

Globally, the use of superelements for the investigation of the jacket load effects is reasonable, because the results differences between superelement and the formerly used beam models are significant. The following is stated in more detail:

- The internal forces and moments at positions higher than the tower base level are

similar. This is as expected, there is only a small influence on the levels of internal loading over the modified part of the models (the jacket). This is shown here for the tower base as an example in Figures 6.9 and 6.11.

- The superelement modeling changes the global load bearing behavior of the jacket. This leads to large differences of mean load effects. A symmetry in the loading disappears for the reaction forces at mudline in mean wind direction and a maximum is found at one of the legs instead (Table 6.14). This is in accordance with what was found for the jacket under static load only (see Table 6.12).

- DEL at the constrained bottom of the structure are generally larger for the superelement model. For the mean load direction, the difference is $\Delta F_x \approx 10\,\%$ as shown in Table 6.15.

- The superelement model is more compliant. This leads to generally larger deflections and it can be found when time domain simulations are directly compared (see e.g. Figure 6.10). However, the differences in the deflections are not very significant. Therefore, it is possible that slightly different dynamics of the systems in combination with the stochastic loading lead to larger deflections for the stiffer structure in special cases. This becomes obvious when results are compared as shown in Table 6.16.

Chapter 7

Conclusions

It is of vital importance for the successive development of the Offshore wind sector that (1) the LCoE is further reduced and (2) aside from being cost effective, offshore wind farms are reliable. One driver of the cost of energy reduction is innovation in the OWT systems. The development of innovative components or turbine systems as a whole is closely tied to the capabilities of the tools that are used for simulation of the systems, for the prediction of inherent loads and load effects. Developments like the branched support structures that are currently installed and further developed can only be reliable and cost effective when their dynamic behavior with a WT atop is understood in detail. That is where this work contributes with the use of improved structural simulation capabilities in an aeroelastic tool with two common structure types and the respective conclusions.

Section 7.1 gives the contributions to the state of the art. In Section 7.2 practical recommendations on the application of the results of this work depending on the respective possibilities – mainly in terms of available tools – are given. Finally, Section 7.3 describes research work that is already ongoing, planned or that is now possible based on the findings described herein.

7.1 Contribution to the state of the art

Thanks to its superelement feature, ADCoS-Offshore enables the user to tackle one of the research needs associated with aeroelastic tools: The necessary improvement of joint representation in loads simulation of OWTs with branched support structures. The superelement models are more accurate than the formerly used beam models[1]. Enhanced beam models including LJF via parametric formulae are less accurate[2] as well and have a restricted parameter range over which they can be properly applied.

Model development and especially shell reference model development for the tripod and the jacket support structure have to be realized with caution, but then, the higher

---

[1]The shell models – that are used as a reference herein – lead to an increase of simulation effort that is not suitable for aeroelastic analyses.

[2]This work does not give a direct comparison of results from models including Buitrago's approach and superelement models, but the superior accuracy of the superelement models results from the modeling theory directly. Furthermore, the implementation of Buitrago's approach in a coupled tool would be a challenge, because the application of the parametric formulae depends also from the load direction, and this load direction changes in every time step in the respective simulations (See also Section 2.3.7 for more background on these topics).

fidelity shell model can serve as a reference[3]. The superelement models, that are defined with the beam models as starting points have an even lower number of DOFs than the beam models and therefore do not lead to an increase of computational cost. For the Tripod the number of DOFs is reduced from n_{beam}=630 (DOFs) to n_{super}=474 (DOFs). The only drawback is the higher modeling effort. But the modeling only has to be done once and the number of load cases – simulated with the same model – does not influence this effort.

Studies of the shell models show that relatively low frequencies are associated with mode shapes that cannot be represented with beam models (shell deformations, like a *tower flattening mode*). This is especially the case for the tower on the the tripod structure with its lowest *shell only frequency* at $f_{\mathrm{low}}= 3.3\,\mathrm{Hz}$. For the jacket structure the problem occurs at higher frequencies because the tower bottom is stiffened by the concrete TP. However, current jacket designs use steel TPs, so this cannot be generalized. This finding puts in question whether it is reasonable to include higher order global mode shapes found with beam models in the design process.

ADCoS-Offshore is verified globally in its basic version – without superelements and shows very good results in comparison to the other tools benchmarked in OC3. On top of that, the superelement feature is verified in a carefully applied step by step approach to assure correct implementation.

For the OWT with tripod support structure and the OWT with jacket support structure, accurate mass calculations can be achieved with beam models given that a certain effort is invested in the modeling. All eigenfrequencies are lower for the more sophisticated superelement models than for the beam models, i.e. the models become more compliant. In any case, the frequency results for the superelement models are closer to the reference and therefore lead to an increase of accuracy. The differences are significant for a subset of frequencies for both structures. The largest differences occur for the torsional frequencies. For the tripod, the use of superelements reduces the first global torsional frequency by $\Delta f_3= 40\,\%$ compared to the formerly used beam models.

Static load cases with realistic loading lead to larger deflections – as an example $\Delta U_x\approx 10\,\%$ for the more compliant superelement models in mean rotor thrust direction for both, jacket and tripod models, a value that is in an expected range. When it comes to the load bearing behavior, i.e. the load path through the tripod models – it is completely changed[4] when superelements are used. The magnitude of the differences i.e. the sensitivity to the stiffness of the joits is surprising even if comparable results were found for the tripod when comparing results from EB beam models to results obtained with Timoshenko (or Timoshenko-like) beam models in Vorpahl et al. (2013). Results from the fatigue load cases confirm this finding. A subset of DELs is reduced in the proximity of the joints as expected due to more compliant joints. But this is not the case for all the DELs, it is not even a general tendency. The jacket models also, show differing member load effects in the static load cases. The differences are not as large as for the tripod, but still significant. The use of the more sophisticated model may even lead to a concentration of loading in one of the jacket legs instead of a more symmetric distribution to two of the legs.

The results comparisons further increase the confidence in the modeling, because they show consistent results. This is the case for comparisons between models and for comparisons between load cases[5].

---

[3]This topic is briefly elaborated at the beginning of Chapter 4.

[4]Dr.-Ing. Holger Huhn, Head of Research & Development at WindMW gmbH, formerly Head of Department for support structures at IWES: "Der Tripod das unbekannte Wesen" (German for: "The tripod, the unknown creature", 2011, private conversation)

[5]The conclusion, that modeling errors would be spotted because of conspicuous inconsistency of results is in line with experience from OC3 (see also Section 2.3.4).

The following should be noted: Usually, modal analyses are performed to assure that a loads model is appropriate. For both structures investigated herein, mode shapes are comparable, the eigenfrequencies are lower for the superelement models, the models are more compliant, deflections are larger, but the differences are manageable. Modal analysis results fit with deflection results, i.e. the modal analyses to some extent allow for a prediction of the deflections. An exception is the first global torsional frequency for the tripod which is reduced from $f_{t0, \text{beam}} = 4.6 \, \text{Hz}$ for the beam model to $f_{t0, \text{shell}} = 2.1 \, \text{Hz}$ for the shell model. This difference is large and the shell model frequency lies in a relevant range for dynamic analyses. In a frequency check for controller tuning and loads simulation (Campbell diagram) differences of a few percent are accounted for. Even if the lower torsional frequency does not lead to excessive vibrations in this study, in general, this problem may occur for other boundary conditions.

The above described straightforward interpretation of frequency results leading to deflection patterns cannot be performed for frequency results combined with load effects on member level. It is therefore not possible to derive valuable information on the load path to the legs and the resulting mudline level – or pile head – loads. The modal analyses results do not point out that there may be such large differences, there is not even the possibility to make a prediction of tendencies how single load effects are changed. For turbine loads, the beam model, crosschecked with a modal analysis might lead to good results. For member forces and moments in the support structure and for the pile loading, this is not the case, neither for the tripod, nor for the jacket.

Summing up, the superelement models increase accuracy of aeroelastic simulation for OWTs with tripod and jacket structures, lead to significantly differing load effects and structural deflections and therefore have the potential to lead to more reliable and cost effective structures. But it should be noted – when assessing the results differences – that many sources of uncertainty or even well-known errors exist in the context of loads simulation and that the quantification of uncertainty on the system level is challenging[6].

7.2   Recommendations

The use of superelements to include LJF in the support structure models for loads simulations increases the accuracy of the simulations without increasing the computational effort. Only the modeling effort is slightly increased. The more sophisticated loads models lead to large differences in calculated load effects compared to the formerly used beam models. Therefore, it is obviously recommended to use superelements in loads simulation as described in this work if the respective level of accuracy is required.

In case this is not possible – e.g. if an aeroelastic tool which does not include such a feature is used in daily engineering work – the following approach might be considered. The static load distribution proved to give a good comparability to the results later obtained in the dynamic load case set. Based on this, the following might be realized:

- Set up shell or superelement structure model in general FE tool.

- Set up beam model in aeroelastic tool.

- Apply the same static loads to both models.

- Tune properties of the beams representing the joints in the beam model to fit the static load distribution through the structure.

---

[6]Different sources of uncertainty are mentioned in Section 2.3.4 (results differences in aeroelastic tool verification, stochastic input variability, challenges during tool validation, difficulties when validating specific aspects of aeroelastic models) and Section 2.3.5 (different inaccuracies as reasons for tool developments).

- Run loads simulation with aeroelastic tool and tuned beam model.

This would be a solution that is comparable to the common use of parametric formulae from the modeling side (tuned beams at joint) but with another source for the fitted parameters (based on member load effects in a more detailed model of the whole structure, not based on local deflections derived from shell-joint models). The approach is not as straightforward as the use of superelements and adds some uncertainty when it comes to the tuning of the beam parameters – it is hard to assure that all relevant effects are captured[7]. But an unmodified aeroelastic tool in combination with a standard FE tool would be sufficient for the modeling and simulation. And the approach would increase the accuracy compared to the use of unmodified beam models and even compared to the use of a beam model that includes LJF based on parametric formulae.

Using Timoshenko-like beam elements (mentioned in Section 2.3.5 based on Klausmann et al. (2012) and Vorpahl et al. (2013)) was shown to reduce the error for a tripod structure as well. This approach includes shear deflections in the beam members but neglects LJF. In contrast to the above mentioned this is closer to the physics, but removes the error sources only partially (still no LJF included).

This work is dealing with an interdisciplinary topic: Usually, detailed support structure models are used in offshore structure departments while loads models including the OWT as a whole – but with simpler component models – are used by WT loads specialists. Interdisciplinary work or the combination of knowledge and experience from neighboring engineering fields can often lead to further developments. On top of that, this is especially the case for WTs, being coupled dynamic systems, that are simulated with respective system models. The system approach combined with a more detailed look into one component is often promising. This is explicitly reflected in Section 2.3.1, that describes the schematic of increasing the fidelity of one component model while keeping the residual model as it is during tool development. Nevertheless, the results described herein show that especially the combination of loads models with – slightly – more detailed support structure models is a reasonable approach when it comes to loads of OWTs with multi-member support structures[8].

7.3   Future work

Based on this work, the superelement feature in the aeroelastic tool ADCoS-Offshore can be further used to deepen the knowledge on load effects in branched OWT support structures applying full load case sets – as used in the certification of OWTs. This work focuses on the loads and load effects. The influence of the presented modeling feature on the lifetime of components[9] and the relevance of the differences in terms of typical design drivers is a logical next step.

Herein, the development and modification of ADCoS-Offshore is carefully verified step by step mainly by comparing results for single components of the models. A reasonable next step is the verification via results obtained with the complete model. This requires a tool with comparable capabilities such as the one currently being developed based on

---

[7]In fact, the methodology for the proper tuning of the beam properties would be the main challenge in such an approach, mainly because of the *size* and *complexity* of the models.

[8]OWTs on multi-member support structures are far from being a mature technology and the transfer of knowledge between two relatively developed engineering fields (Here: WTs on tubular towers on the one hand side and multi member offshore structures on the other hand side) is not a simple task. Therefore this is not surprising.

[9]Such a task would also include detailed investigations on the contribution of each DLC to the total damage and the changes of the respective distribution due to the use of superelements.

the work by Böker (2010). The verification via tool comparison is planned in the national German Research Project GIGAWIND life[10].

The next step after a verification via tool comparison is a validation with real life data. This is planned in general in the Offshore Code Comparison Collaboration Continuation with Correlation (OC5) project, the follow-on project to OC4 within the IEA wind frame-work[11]. Furthermore, in the above mentioned GIGAWIND life project, tool validation – including the superelement feature for a branched support structure – based on RAVE measurement data is planned.

In general, the limited possibilities for validation of aeroelastic tools in research projects – especially with a large number of research partners – are hampering tool develop-ment. Respective measurement campaigns, and making (turbine) data available for re-searchers, i.e. a reduced sensitivity concerning confidential data, would be beneficial not only for the research community, but in the mid term for the competitiveness of the offshore wind industry as a whole - and therefore for each single OWT manufacturer too.

---

[10]http://www.gigawind.de/gigawind_life.html?&L=1; September 09, 2014.
[11]https://www.ieawind.org/task_30/task30_Public.html; December 09, 2014. OC5 is not set up as a new IEA Wind Research task, but as an extension of the existing Task 30.

Bibliography

Airy, G. (1845). On tides and waves. In E. Smedley, H. Rose, and H. Rose (Eds.), *Encyclopædia Metropolitana (1817-1845), Mixed Sciences*, Volume 3. London, UK: Fenner, R.

API RP 2A-LRFD (1993). RP 2A-LRFD: Planning, designing and constructing fixed offshore platforms – load and resistance factor design. Standard, American Petroleum Institute, Washington DC, USA.

Argyris, J. and H.-P. Mlejnek (1997). *Computerdynamik der Tragwerke*. Braunschweig, Germany: Friedrich Vieweg & Sohn Verlagsgesellschaft. In German.

ASAS User Manual (2006). Asas (linear). User manual, Century Dynamics Limited, Horsham, UK.

Barker, A., G. Timco, H. Gravesen, and P. Volund (2005a). Ice loading on danish wind turbines part 1: Dynamic model tests. *Cold Regions Science and Technology 41*(1), 1 – 23.

Barker, A., G. Timco, H. Gravesen, and P. Volund (2005b). Ice loading on danish wind turbines part 2: Dynamic model test results. *Cold Regions Science and Technology 41*(1), 25 – 47.

Barthelmie, R., K. Hansen, T. Frandsen, O. Rathmann, J. Schepers, W. Schlez, J. Phillips, K. Rados, A. Zervos, E. Politis, and Chaviaropoulos (2009). Modelling and measuring flow and wind turbine wakes in large wind farms offshore. *Wind Energy 12*(5), 431 – 444.

Bathe, K.-J. (2001). *Finite-Elemente-Methoden* (Second ed.). Berlin, Germany: Springer. In German.

Beyer, F., M. Arnold, and P. Cheng (2013). Analysis of floating offshore wind turbine hydrodynamics using coupled CFD and multibody methods. In *Proceedings of the Twenty-third (2013) International Offshore and Polar Engineering Conference*, Volume 1, pp. 261 – 267.

Biehl, F. (2004). Rechnerische Bewertung von Fundamenten von Offshore Windenergieanlagen bei Kollisionen mit Schiffen. Technical report, Technische Universität Hamburg-Harburg, Hamburg, Germany. In German.

Bir, G. and J. Jonkman (2007). Aeroelastic instabilities of large offshore and onshore wind turbines. *Journal of Physics: Conference Series 75*(012069).

Boehm, B. (1981). *Software Engineering Economics*. Upper Saddle River NJ, USA: Prentice Hall.

Böker, C. (2010). *Load simulation and local dynamics of support structures for offshore wind turbines*. Dissertation thesis, Leibniz Universität Hannover, Institut für Stahlbau, Hannover, Germany.

Breton, S.-P. and G. Moe (2009). Status, plans and technologies for offshore wind turbines in Europe and North America. *Renewable Energy 14*(3), 646 – 654.

Buitrago, J. and B. E. Healy (1993). Local joint flexibility of tubular joints. In *Twelfth International Conference on Offshore Mechanics and Arctic Engineering*, Volume 1, Glasgow, UK, pp. 405 – 416.

Burton, T., D. Sharpe, N. Jenkins, and E. Bossanji (2011). *Wind Energy Handbook* (Second ed.). Hoboken NJ, USA: John Wiley & Sons.

Carbon Trust (2008). Offshore wind power: big challenge, big opportunity – maximising the environmental, economic and security benefits. Technical Report CTC743, Carbon Trust, London, UK.

Carcangiu, C., D. Schlipf, T. Fischer, E. Bossanji, and I. Pineda (2011). Facing extreme wind conditions with LIDAR assisted control. In *European Wind Energy Agency Conference Proceedings*, Brussels, Belgium.

Cellier, F. (1991). *Continuous System Modeling*. New York NY, USA: Springer.

Chakrabarti, S. (2005). *Handbook of offshore engineering*. London, UK: Elsevier.

Chaplin, J. (1980). Developments of stream function wave theory. *Coastal Engineering 3*, 179 – 205.

Christensen, C. F., L. W. Andersen, and P. H. Pedersen (2009). Ship collision risk for an offshore wind farm. Technical report, Rambøll Wind Energy, Copenhagen, Denmark.

Corson, D., D. Griffith, T. Ashwill, and F. Shakib (2012). Investigating aeroelastic performance of multi-megawatt wind turbine rotors using CFD. In *53rd AIAA/ASME/ASCE/ASC Structures, Structural Dynamics, and Materials Conference*, Number AIAA 2012-1827, Honolulu HA, USA.

Craig, R. R. and M. C. C. Bampton (1968). Coupling of substructures for dynamic analysis. *AIAA Journal 6*(7), 1313–1319.

De Vries, W. (2008). Soft-stiff bottom mounted support structures – analysis of monopile and multi-member support structures for offshore wind turbines. Upwind Deliverable D4.3.2, Delft University of Technology, Delft, The Netherlands. (Restricted to project members).

De Vries, W., N. K. Vemula, P. Passon, T. Fischer, D. Kaufer, D. Matha, B. Schmidt, and F. Vorpahl (2011). Support structure concepts for deep water sites. Upwind final report WP 4.2. Deliverable D4.2.8, Delft University of Technology, Delft, The Netherlands.

Dean, R. G. (1965). Stream function representation of nonlinear ocean waves. *Journal of Geophysical Research 70*(18), 4561 – 4572.

DNV-OS-J101 (2014). DNV-OS-J101: Design of offshore wind turbine structures. Offshore standard, Det Norske Veritas, Høvik, Norway.

DNV-RP-C205 (2007). DNV-RP-C205: Environmental conditions and environmental loads. Recommended practice, Det Norske Veritas, Høvik, Norway.

Dubois, J., P. Schaumann, and M. Muskulus (2013). Advanced representation of tubular joints in jacket models for offshore wind turbine simulation. *Energy Procedia 35*, 234 – 243.

Efthymiou, M. (1985). Local rotational stiffness of unstiffened tubular joints. Technical Report RKER 85.199, Kononklijke/Shell Exploratie en Produktie Laboratorium, Rijswijk, The Netherlands.

Faltinsen, O. (1990). *Sea Loads on Ships and Offshore Structures*. Cambridge, UK: Cambridge University Press.

Fessler, H., P. Mockford, and J. Webster (1986a). Parametric equations for the flexibility matrices of multi-brace tubular joints in offshore structures. *Proceedings – Institution of Civil Engineers 81*, 675 – 696. Paper 9124.

Fessler, H., P. Mockford, and J. Webster (1986b). Parametric equations for the flexibility matrices of single brace tubular joints in offshore structures. *Proceedings – Institution of Civil Engineers 81*, 659 – 673. Paper 9089.

Fischer, T. (2012). *Mitigation of Aerodynamic and Hydrodynamic Induced Loads of Offshore Wind Turbines*. Dissertation thesis, Endowed Chair of Wind Energy at the Institute of Aircraft Design, Universität Stuttgart, Stuttgart, Germany.

Fischer, T., W. de Vries, and B. Schmidt (2010). Upwind design basis. Upwind deliverable, Endowed Chair of Wind Energy at the Institute of Aircraft Design, Universität Stuttgart, Stuttgart, Germany.

Fischer, T. and M. Kühn (2009). Site sensitive support structure and machine design for offshore wind farms. In *European Wind Energy Conference*, Marseille, France.

Fischer, T. and M. Kühn (2010). Importance and mitigation of loading on offshore wind turbines on monopile support structures in cases of non-availability. In *Proceedings of the Twentieth International Offshore and Polar Engineering Conference*, Volume 1, Beijing, China, pp. 644 – 650.

Fischer, T., P. Rainey, E. Bossanji, and M. Kühn (2012). Study on control concepts suitable for mitigation of loads from misaligned wind and waves on offshore wind turbines supported on monopiles. *Wind Engineering 35*(5), 561 –574.

GL Offshore (2012). Guideline for the certification of offshore wind turbines. Guideline, Germanischer Lloyd Renewables Certification, Hamburg, Germany.

Glauert, H. (1926). A general theory of the autogyro. *Aeronautical Research Committee Reports and Memoranda* (1111), 558 – 593.

Glauert, H. (1935). Airplane propellers. In O. F. Durand (Ed.), *Aerodynamic Theory*, pp. 169 – 360. Berlin, Germany: Julius Springer.

Goda, Y. (2010). *Random Seas and Design of Maritime Structures* (Third ed.). Singapore, Republic of Singapore: World Scientific Publishing.

Grüne, J. and H. Oumeraci (2007). Untersuchungen zur Kolkbildung und zum Kolkschutz für Offshore-Monopile-Gründungen. Abschlussbericht, Forschungszentrum Küste Hannover, Hannover, Germany. In German.

Guyan, R. J. (1965). Reduction of stiffness and mass matrices. *AIAA Journal 3*(2), 380.

Hansen, M. and H. A. Madsen (2011). Review paper on wind turbine aerodynamics. *Journal of Fluids Engineering 133*(11), 1 – 12.

Hansen, M. H. (2007a). Aeroelastic instability problems for wind turbines. *Wind Energy 10*(6), 551 – 577.

Hansen, O. (2007b). *Aerodynamics of Wind Turbines* (Second ed.). London, UK: Routledge.

Hapel, K.-H. (1990). *Festigkeitsanalyse dynamisch beanspruchter Offshore-Konstruktionen*. Braunschweig, Germany: Friedrich Vieweg & Sohn Verlagsgesellschaft. In German.

Hasselmann, K., T. Barnett, E. Bouws, H. Carlson, D. Cartwright, K. Enke, J. Ewing, H. Gienapp, D. Hasselmann, P. Kruseman, A. Meerburg, P. Müller, D. Olbers, K. Richter, W. Sell, and H. Walden (1973). Measurements of wind-wave growth and swell decay during the joint north sea wave project (JONSWAP). *Ergänzungsheft zur deutschen hydrografischen Zeitschrift* (12).

Hauptmann, S., M. Bülk, L. Schön, S. Erbslöh, K. Boorsma, F. Grasso, and M. Kühn (2012). Impact of the lifting-line free vortex wake method on the simulated loads of multi-MW wind turbines. In *Proceedings of the Science of making torque from wind*, Oldenburg, Germany.

Hauptmann, S., S. Mulski, M. Kühn, and L. Mauer (2007). Advanced drive train modeling in a virtual wind turbine using the multibody simulation code Simpack. In *European Wind Energy Conference*, Milan, Italy.

Heinonen, J., S. Hetmanczyk, and M. Strobel (2011). Introduction of ice loads in overall simulation of offshore wind turbines. In *Proceedings of the Twenty-first International Conference on Port and Ocean Engineering under arctic conditions*, Number POAC11-024, Montréal, Canada.

Henderson, A. and D. Witcher (2010). Floating offshore wind energy – a review of the current status and an assessment of the prospects. *Wind Engineering 34*(1), 1 – 16.

HSE OTR (2002). The effects of local joint flexibility on the reliability of fatigue life estimates and inspection planning. Offshore Technology Report 2001/056, Health and Safety Executive, Caerphilly, UK.

IEC 61400-1 (2005). Wind turbines – part 1: Design requirements. International standard, International Electrotechnical Commission, Geneva, Switzerland.

IEC 61400-13 (2005). Wind turbine generator systems – part 13: Measurements of mechanical loads. International standard, International Electrotechnical Commission, Geneva, Switzerland.

IEC 61400-3 (2009). Wind turbines – part 3: Design requirements for offshore wind turbines. International standard, International Electrotechnical Commission, Geneva, Switzerland.

IEC TS 61400-23 (2005). Wind turbine generator systems – part 23: Full-scale structural testing of rotor blades. Technical specification, International Electrotechnical Commission, Geneva, Switzerland.

Jonkman, J. (2007). Dynamics modeling and loads analysis of an offshore floating wind turbine. Technical Report NREL/TP-500-41958, National Renewable Energy Laboratory, Golden CO, USA.

Jonkman, J., S. Butterfield, W. Musial, and G. Scott (2009). Definition of a 5-MW Reference Wind Turbine for Offshore System Development. Technical Report NREL/TP-500-38060, National Renewable Energy Laboratory, Golden CO, USA.

Jonkman, J. and A. Cordle (2011). State of the art in floating wind turbine design tools. In *Proceedings of the Twenty-first International Offshore and Polar Engineering Conference*, Volume 1, Maui HA, USA, pp. 367 – 374.

Jonkman, J. and D. Matha (2009). A quantitative comparison of the responses of three floating platforms. In *European Offshore Wind Conference*, Stockholm, Sweden.

Jonkman, J. and D. Matha (2011). Dynamics of offshore floating wind turbines – analysis of three concepts. *Wind Energy 14*(4), 557 – 569.

Kaimal, J., J. Wyngaard, Y. Izumi, and O. Coté (1972). Spectral characteristics of surface-layer turbulence. *Quarterly Journal of the Royal Meteorological Society 98*(7), 563 – 589.

Kaufer, D. and P. Cheng (2014). Validation of an integrated simulation method with high-resolution load measurements of the offshore wind turbine repower 5M at alpha ventus. *Journal of Ocean and Wind Energy 1*(1), 30 – 40.

Kaufer, D., T. Fischer, F. Vorpahl, W. Popko, and M. Kühn (2010). Different approaches to modeling jacket support structures and their impact on overall wind turbine dynamics. In *Deutsche Windenergie-Konferenz*, Bremen, Germany.

Kind, R. (2001). Ice accretion simulation evaluation test. Technical Report RTO-TR-038 AC/323(AVT-006)TP/26, North Atlantic treaty Organization Research and Technology Organization, Neuilly sur Seine, France.

Klausmann, P., S. Kleinhansl, S. Streiner, and F. Vorpahl (2012). Influence of shear deformation on the elastic behavior of large blades and support structures in offshore wind turbine simulations. In *Deutsche Windenergie-Konferenz*, Wilhelmshaven, Germany.

Kleinhansl, S., M. Mayer, and A. Mangold (2004). ADCoS - A Nonlinear Aeroelastic Code for the Complete Dynamic Simulation of Offshore- Structures and Lattice-Towers. In *Deutsche Windenergie-Konferenz*, Wilhelmshaven, Germany.

Krogstad, H. and Ø. Arntsen (2000). Linear wave theory - part A regular waves. Lecture notes, Norwegian University of Science and Technology, Trondheim, Norway.

Kühn, M. (2001). *Dynamics and Design Optimisation of Wind Energy Conversion Systems*. Ph. D. thesis, Delft University of Technology, Delft University Wind Energy Research Institute, Delft, The Netherlands.

Laakso, T., I. Baring-Guld, M. Durstewitz, R. Horbaty, A. Lacroix, E. Peltola, G. Ronsten, L. Tallhaug, and T. Wallenius (2010). State-of-the-art of wind energy in cold climates. VTT Working Paper 152, VTT Technical Research Centre of Finland, Espoo, Finland.

Larsen, T. J., H. A. Madsen, K. Thomsen, and F. Rasmussen (2007). Reduction of teeter angle excursions for a two-bladed downwind rotor using cyclic pitch control. In *European Wind Energy Conference*, Milan, Italy.

Leishman, J. and T. Beddoes (1989). A semi-empirical model for dynamic stall. *Journal of the American Helicopter Society 34*(3), 3–17.

MacCamy, R. and R. Fuchs (1954). Wave forces on piles: A diffraction theory. Technical Memo 69, US Army Corps of Engineers, Beach Erosion Board, Washington D.C., USA.

Makkonen, L. and T. Laakso (2001). Modelling and prevention of ice accretion on wind turbines. *Wind Engineering 25*(1), 3 – 21.

Mann, J. (1998). Wind field simulation. *Probabilistic Engineering Mechanics 13*(4), 269–282.

Matha, D., M. Schlipf, A. Cordle, R. Pereira, and J. Jonkman (2011). Challenges in simulation of aerodynamics, hydrodynamics, and mooring-line dynamics of floating offshore wind turbines. In *Proceedings of the Twenty-first International Offshore and Polar Engineering Conference*, Volume 1, Maui HA, USA, pp. 421 – 428.

Mittendorf, K. (2006). *Hydromechanical Design Parameters and Design Loads for Offshore Wind Energy Converters*. Dissertation thesis, Leibniz Universität Hannover, Institut für Strömungsmechanik und Elektronisches Rechnen im Bauwesen, Hannover, Germany.

Moriarty, P. J. and A. C. Hansen (2005). Aerodyn theory manual. Technical Report NREL/TP-500-36881, National Renewable Energy Laboratory, Golden CO, USA.

Morison, J., J. Johnson, and S. Schaaf (1950). The force exerted by surface waves on piles. *Journal of Petroleum Engineers 2*(5), 149 – 154.

Müller, G. and C. Groth (2007). *FEM für Praktiker – Band 1 Grundlagen* (Eighth ed.). Renningen, Germany: Expert Verlag. In German.

Muskulus, M. (2012). The full-height lattice tower concept. *Energy Procedia 24*, 371 – 377.

Nichols, J., T. Camp, J. Jonkman, S. Butterfield, T. J. Larsen, A. M. Hansen, J. Azcona, A. Martinez, X. Munduate, F. Vorpahl, S. Kleinhansl, M. Kohlmeier, T. Kossel, C. Böker, and D. Kaufer (2009). Offshore Code Comparison Collaboration within IEA Wind Annex XXIII: Phase III Results Regarding Tripod Support Structure Modeling. In *47th AIAA Aerospace Sciences Meeting*, Number AIAA 2009-1038, Orlando FL, USA.

NORSOK M-501 (2012). Surface preparation and protective coating. NORSOK Standard M-501, NORSOK, Lysaker, Norway.

NORSOK M-503 (2007). Cathodic protection. NORSOK Standard M-503, NORSOK, Lysaker, Norway.

Ottosen, N. and H. Petersson (1992). *Introduction to the Finite Element Method*. Harlow, UK: Prentice Hall.

Panofsky, H. A. and J. A. Dutton (1984). *Atmospheric Turbulence: models and methods for engineering applications*. Hoboken NJ, USA: John Wiley & Sons.

Paraschivoiu, I. and F. Saeed (2001). Ice accretion simulation code canice. In *International Aerospace Symposium*, Bucharest, Romania.

Peters, D. A. and C. J. He (1991). Correlation of measured induced velocities with a finite-state wake model. *Journal of the American Helicopter Society 36*(3), 59 – 70.

Petersen, C. (2010). *Dynamik der Baukonstruktion*. Braunschweig, Germany: Springer. In German.

Pierson, W. J. and L. Moskowitz (1964). A proposed spectral form for fully developed wind seas based on the similarity theory of S. A. Kitaigorodskii. *Journal of Geophysical Research 69*(24), 5181–5190.

Popko, W., J. Heinonen, S. Hetmanczyk, and F. Vorpahl (2012). State-of-the-art comparison of standards in terms of dominant sea ice loads for offshore wind turbine support structures in the Baltic Sea. In *Proceedings of the Twenty-second International Offshore and Polar Engineering Conference*, Volume 1, Rhodes, Greece, pp. 426 – 433.

Popko, W., F. Vorpahl, and P. Antonakas (2014). Investigation of local vibration phenomena of a jacket sub-structure caused by coupling with other components of an offshore wind turbine. *Journal of Ocean and Wind Energy 1*(2), 111 – 118.

Popko, W., F. Vorpahl, A. Zuga, M. Kohlmeier, J. Jonkman, A. Robertson, T. Larsen, A. Yde, K. Sætertrø, K. Okstad, J. Nichols, T. Nygaard, Z. Gao, D. Manolas, K. Kim, Q. Yu, W. Shi, H. Park, A. Vásquez-Rojas, J. Dubois, D. Kaufer, P. Thomassen, M. de Ruiter, T. Van der Zee, J. Peeringa, H. Zhiwen, and H. von Waaden (2014). Offshore code comparison collaboration continuation (OC4), phase I – results of coupled simulations of an offshore wind turbine with jacket support structure. *Journal of Ocean and Wind Energy 1*(1), 1 – 11.

Rainey, P. and T. Camp (2007). Constrained non-linear waves for offshore wind turbine design. *Journal of Physics: Conference Series 75*(012067).

Randrup-Thomsen, S., L. Andersen, and J. K. Gaarde (2009). Risk of oil pollution due to ship collision with offshore wind farms. Technical report, Rambøll Wind Energy, Copenhagen, Denmark.

Reese, L. C., W. R. Cox, and F. D. Koop (1974). Analysis of Laterally Loaded Piles in Sand. In *Offshore Technology Conference*, Number 2080, Dallas TX, USA.

Robertson, A.N., F. Wendt, J. Jonkman, W. Popko, F. Vorpahl, C. Stansberg, E. Bachynski, I. Bayati, F. Beyer, J. de Vaal, R. Harries, A. Yamaguchi, H. Shin, B. Kim, T. van der Zee, P. Bozonnet, B. Aguilo, R. Bergua, J. Qvist, W. Qijun, X. Chen, M. Guerinel, Y. Tu, H. Yutong, and R. Li (2015). OC5 project phase I: Validation of hydrodynamic loading on a fixed cylinder. In *Proceedings of the Twenty-fifth International Offshore and Polar Engineering Conference*, Kona HA, USA. (to be published).

Robertson, A., J. Jonkman, W. Musial, W. Popko, and F. Vorpahl (2014). IEA wind task 30 offshore code comparison collaboration continued. Final report, IEA Wind, Paris, France.

Rodríguez, A., C. Carcangiu, I. Pineda, T. Fischer, B. Kuhnle, M. Scheu, and M. Martin (2011). Wind turbine structural damping control for tower load reduction. In *International Modal Analysis Conference*, Jacksonville FL, USA, pp. 141 – 153.

Romeijn, A., R. Puthli, and J. Wardenier (1991). The flexibility of uniplanar and multiplanar joints made of circular hollow sections. In *Proceedings of the First International Offshore and Polar Engineering Conference*, Volume 4, Edinburgh, UK, pp. 67 – 76.

Sarpkaya, T. (2010). *Wave Forces on Offshore Structures*. New York NY, USA: Cambridge University Press.

Sarpkaya, T. and M. Isaacson (1981). *Mechanics of wave forces on offshore structures*. New York NY, USA: Van Nostrand Reinhold.

Savenije, F. and J. Peeringa (2009). Aero-elastic simulation of offshore wind turbines in the frequency domain. Technical Report ECN-E-09-060, Energy research Center of the Netherlands, Amsterdam, The Netherlands.

Schaumann, P. and C. Böker (2008). Numerical consideration of local joint flexibilities. In *Proceedings of the Eighteenth International Offshore and Polar Engineering Conference*, Volume 1, Vancouver, Canada, pp. 447 – 454.

Schlipf, D., T. Fischer, C. Carcangiu, M. Rosetti, and E. Bossanyi (2010). Load analysis of look-ahead collective pitch control using LIDAR. In *Deutsche Windenergie-Konferenz*, Bremen, Germany.

Schlipf, D., D. Trabuchi, O. Bischoff, M. Hofsäß, J. Mann, T. Mikkelsen, and A. Rettenmeier (2010). Testing of frozen turbulence hypothesis for wind turbine applications with a scanning lidar system. In *15th International Symposium for the Advancement of Boundary Layer Remote Sensing (ISARS)*, Paris, France.

Schmidt, B., U. Smolka, S. Hartmann, and P. Cheng (2013). Validation of the dynamic wake meander model with areva M5000 load measurements at alpha ventus. In *Proceedings of the European Wind Energy Association Offshore Conference*, Frankfurt, Germany.

Schmitz, G. (1955). Theorie und Entwurf von Windrädern optimaler Leistung. *Wissenschaftliche Zeitung der Universität Rostock. 5. Jahrgang 1955/1956*. In German.

Schreck, S. (2007). Rotationally augmented flow structures and time varying loads on turbine blades. In *45th AIAA Aerospace Sciences Meeting and Exhibit*, Number AIAA 2007-627, Reno NV, USA.

Seidel, M. (2007). Jacket substructures for the repower 5M wind turbine. In *European Offshore Wind Conference*, Berlin, Germany.

Seidel, M. (2010). Feasability of monopiles for large offshore wind turbines. In *Deutsche Windenergie-Konferenz*, Bremen, Germany.

Seidel, M. (2014a). Substructures for offshore wind turbines – current trends and developments. In *Festschrift Peter Schaumann*, Hannover, Germany.

Seidel, M. (2014b). Wave induced fatigue loads. *Stahlbau 83*(8), 535 – 541.

Seidel, M. and G. Foss (2006). Impact of different substructures on turbine loading and dynamic behavior for the DOWNVInD Project in 45m water depth. In *European Wind Energy Conference*, Athens, Greece.

Seidel, M. and T. Gosch (2006). Technical challenges and their solution for the beatrice windfarm demonstrator project in 45m water depth. In *Deutsche Windenergie-Konferenz*, Bremen, Germany.

Seidel, M. and F. Ostermann (2009). Validation of offshore load simulations using measurement data from the DOWNVInD project. In *European Offshore Wind Conference*, Stockholm, Sweden.

Seidel, M., M. von Mutius, P. Rix, and D. Steudel (2005). Integrated analysis of wind and wave loading for complex support structures of offshore wind turbines. In *European Offshore Wind Conference*, Copenhagen, Denmark.

Seidel, M., M. von Mutius, and D. Steudel (2004). Design and load calculations for offshore foundations of a 5MW turbine. In *Deutsche Windenergie-Konferenz*, Wilhelmshaven, Germany.

Snell, H. (2003). Review of aerodynamics for wind turbines. *Wind Energy 6*(3), 203 – 211.

Sobey, R. (1992). A local fourier approximation method for irregular wave kinematics. *Applied Ocean Research 14*, 93 – 105.

Söker, H., M. Damaschke, C. Illig, K. Kröning, and N. Cosack (2006). A guide to design load validation. In *Deutsche Windenergie-Konferenz*, Bremen, Germany.

Stelzmann, U., C. Groth, and G. Müller (2006). *FEM für Praktiker - Band 2: Strukturdynamik* (Fourth ed.). Renningen, Germany: Expert Verlag. In German.

Strach, M. and T. Quiroz (2012). Stand der Technik von Tragstrukturen für Offshore-Windenergieanlagen. Technical report, Fraunhofer Institute for Wind Energy and Energy System Technology IWES, Bremerhaven, Germany. In German.

Strach, M., F. Vorpahl, C. Hillmann, M. Strobel, and M. Brommundt (2012). Modeling offshore wind turbine substructures using engineer design data – a newly developed parametric approach. In *Proceedings of the Twenty-second (2012) International Offshore and Polar Engineering Conference*, Volume 1, pp. 17–22.

Strobel, M., C. Hillmann, U. Wihlfahrt, R. Samlaus, S. Hetmanczyk, A. Zuga, X. Gu, H. Schwarze, M. Strach, and F. Vorpahl (2012). Abschlussbericht Projekt OneWind (Phase 1). Technical report, Fraunhofer Institute for Wind Energy and Energy System Technology IWES, Bremerhaven, Germany. In German.

Strobel, M., F. Vorpahl, C. Hillmann, X. Gu, A. Zuga, and U. Wihlfahrt (2011). The onWind modelica library for offshore wind turbines – implementation and first results. In *Modelica Conference*, Dresden, Germany.

Tarp-Johansen, N. J., L. Andersen, E. D. Christensen, C. Mørch, B. Kallesøe, and S. Frandsen (2009). Comparing sources of damping of cross-wind motion. In *European Offshore Wind Conference*, Stockholm, Sweden.

Taubert, M., S. Clauss, H. Freudenberg, A. Keil, M. März, M. Moder, and H. Wulf (2011). Wind turbine design codes: Eine Validierung von alaska/Wind mit Bladed, FAST und FLEX5. Technical report, Institut für Mechatronik der Universität Chemnitz, Chemnitz, Germany. In German.

Taylor, G. I. (1938). The spectrum of turbulence. *Proceedings of the Royal Society A 164*(919), 476 – 490.

Thomsen, J. H., T. Forsberg, and R. Bittner (2007). Offshore wind foundations – the COWI experience. In *Proceedings of the 26th International Conference on Offshore Mechanics and Arctic Engineering*, Number OMAE2007-29567, San Diego CA, USA.

Tu, Y. (2013). Numerical investigation on the influence of support structure modeling strategies on the loads of a generic 5-MW turbine on a jacket support structure. Master's thesis, Delft University of Technology, Delft University Wind Energy Research Institute, Delft, The Netherlands.

Tu, Y. and F. Vorpahl (2014). Influence of superelement support structure modeling on the loads on an offshore wind turbine with a jacket support structure. *Journal of Ocean and Wind Energy 1*(3), 153 – 160.

Turner, M., R. Clough, H. Martin, and L. Topp (1956). Stiffness and deflection analysis of complex structures. *Journal of the Aeronautical Sciences 23*(9), 805 – 823.

Van der Hoven, I. (1957). Power spectrum of horizontal wind speed in the frequency range from 0.0007 to 900 cycles per hour. *Journal of Meteorology 14*(2), 160 – 164.

Van der Tempel, J. (2006). *Design of Support Structures for Offshore Wind Turbines*. Ph. D. thesis, Delft University of Technology, Delft University Wind Energy Research Institute, Delft, The Netherlands.

Van der Tempel, J. (2007). *Offshore-Wind. To mill or to be milled. Bluff your way in offshore wind.* Delft, The Netherlands: Delft University of Technology, Delft University Wind Energy Research Institute.

Vemula, N. K., W. De Vries, T. Fischer, A. Cordle, and B. Schmidt (2010). Design solution for the upwind reference offshore support structure. Upwind Deliverable D4.2.6, Rambøll Wind Energy, Copenhagen, Denmark.

Vorpahl, F. (2006). Dynamische Analyse der Tragstruktur einer 5 MW Offshore-Windenergieanlage unter kombinierter Wind- und Wellenanregung. Diploma thesis, Universität Karlsruhe (TH), Institut für Reaktorsicherheit, Karlsruhe, Germany. (in German).

Vorpahl, F., D. Kaufer, and W. Popko (2011). Description of a basic model of the "Upwind reference jacket" for code comparison in the OC4 project under IEA Wind Annex XXX. Technical report, Fraunhofer Institute for Wind Energy and Energy System Technology IWES, Bremerhaven, Germany.

Vorpahl, F., S. M., J. Jonkman, T. Larsen, P. Passon, and J. Nichols (2013). Verification of aero-elastic offshore wind turbine design codes under IEA Wind Task XXIII. *Wind Energy 17*(4), 519–547.

Vorpahl, F. and W. Popko (2011). Description of the load cases and output sensors to be simulated in the OC4 project under iea wind annex XXX. Technical report, Fraunhofer Institute for Wind Energy and Energy System Technology IWES, Bremerhaven, Germany.

Vorpahl, F. and A. Reuter (2011). Fully-coupled wind turbine simulation including substructuring of support structure components: Influence of newly developed modeling approach on fatigue loads for an offshore wind turbine on a tripod support structure. In *Proceedings of the Twenty-first International Offshore and Polar Engineering Conference*, Volume 1, Maui HA, USA, pp. 284 – 290.

Vorpahl, F., M. Strobel, H.-G. Busmann, and S. Kleinhansl (2010). Superelement approach in fully coupled offshore wind turbine simulation: Influence of the detailed support structure modelling on simulation results for a 5-MW turbine on a tripod substructure. In *Proceedings of the Twentieth International Offshore and Polar Engineering Conference*, Volume 1, Beijing, China, pp. 711 – 718.

Vorpahl, F., A. Van Wingerde, M. Blunk, H.-G. Busmann, S. Kleinhansl, T. Kossel, M. Kohlmeier, C. Böker, D. Kaufer, J. Azcona, A. Martinez, and X. Munduate (2009). Validation of a finite element based simulation approach for offshore wind turbines within IEA wind annex XXIII - simulation challenges and results for a 5-MW turbine on a tripod substructure. In *Proceedings of the Nineteenth International Offshore and Polar Engineering Conference*, Volume 1, Osaka, Japan, pp. 362–369.

Wheeler, J. (1970). Method for calculating forces produced by irregular waves. *Journal of Petroleum Technology 249*(3), 359 – 367.

Willecke, A. and T. Fischer (2013). Large monopiles for offshore wind farms in the German North Sea. In *Proceedings of the Conference on Maritime Energy*, Hamburg, Germany, pp. 199 – 209.

Wilson, J. F., B. J. Muga, and L. Reese (2003). *Dynamics of offshore structures* (Second ed.). Hoboken NJ, USA: John Wiley & Sons.

Wittenburg, J. (2008). *Dynamics of Multibody Systems*. Berlin, Germany: Springer.

Woernle, C. (2011). *Mehrkörpersysteme. Eine Einführung in die Kinematik und Dynamik von Systemen starrer Körper*. Berlin, Germany: Springer. In German.

Xiros, N. (2015). *Handbook of Offshore Engineering*. New York NY, USA: Springer. (to be published).

Zwick, D. and M. Muskulus (2014). The simulation error caused by input loading variability in offshore wind turbine structural analysis. *Wind Energy*. Early View.

Zwick, D., S. Schafhirt, M. Brommundt, M. Muskulus, S. Narasimhan, J. Mechineau, and P. Haugsøen (2015). Comparison of different approaches to load calculation for the OWEC quattropod jacket support structure. *Journal of Physics: Conference Series*. (to be published).

Appendix A

Support structures material definition

The parameters given in Table A.1 are basically applied in all support structure models used in this work. In case of modifications, this is explicitly stated.

Table A.1: Steel material definition.

Density	$\rho_s = 7800 \ \mathrm{kg/m^3}$
Young's modulus	$E = 2.1 \cdot 10^{11} \ \mathrm{N/m^2}$
Poisson's ratio	$\nu = 0.3$
Wöhler Material Exponent	$\mu = 3$

Appendix B

Flange definition for towers

Table B.1 gives the flange parameters for the towers used with the tripod- and the jacket substructure, respectively. The steel densities for the flange material $\rho_{\text{fl.}}$ are adapted to meet the global mass requirements for both structures. The coordinates are given in the global CS. At the top flange level, all nodes are rigidly connected. The geometric flange parameters are the same for the tripod- and the jacket support structure, only the flange positions and densities differ.

Table B.1: Flange parameters: Height over MSL (z) at lower end of flange, flange height, flange thickness and flange density.

Flange	Height $[mm]$	Thickness $[mm]$	z Tripod $[m]$	z Jacket $[m]$	$\rho_{\text{fl.}}$ Tripod $[kg/m^3]$	$\rho_{\text{fl.}}$ Jacket $[kg/m^3]$
Bottom	110	230	10	20.15	1707	5361
Middle	100	180	48.8	54.15	2181	6292
Top	240	150	87.6	88.15	1256	3780

Appendix C

Details on tripod structure and models

Table C.1: Tripod substructure nodes and coordinates in the global CS.

Node	x [m]	y [m]	z [m]
1	-24.802	0.0000	-45.000
2	12.400	21.479	-45.000
3	12.400	-21.479	-45.000
4	-24.802	0.0000	-42.979
5	12.400	21.479	-42.979
6	12.400	-21.479	-42.979
7	-24.802	0.0000	-41.143
8	12.400	21.479	-41.143
9	12.400	-21.479	-41.143
10	-24.802	0.0000	-39.306
11	12.400	21.479	-39.306
12	12.400	-21.479	-39.306
13	-24.802	0.0000	-34.071
14	12.400	21.479	-34.071
15	12.400	-21.479	-34.071
16	0.0000	0.0000	-34.713
17	0.0000	0.0000	-32.188
18	0.0000	0.0000	-10.000
19	0.0000	0.0000	0.0000
20	0.0000	0.0000	10.000

Table C.2: Tripod substructure members connecting the nodes given in Table C.1. See also Figure C.1.

Member	Node 1	Node 2
1	1	4
2	2	5
3	3	6
4	4	7
5	5	8
6	6	9
7	7	10
8	8	11
9	9	12
10	10	13
11	11	14
12	12	15
13	7	17
14	8	17
15	9	17
16	10	19
17	11	19
18	12	19
19	4	5
20	5	6
21	6	4
22	16	17
23	17	18
24	18	19
25	19	20
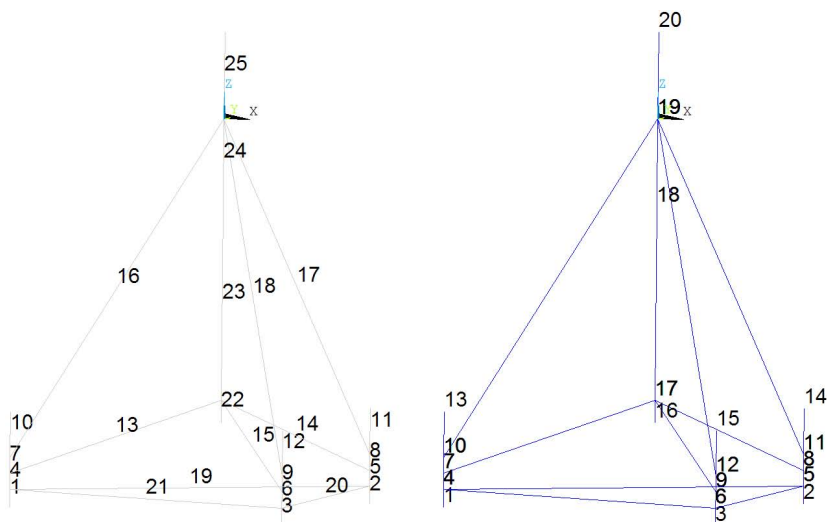
Figure C.1: Tripod substructure members (left) and nodes (right).

Table C.3: Cross sectional properties outer diameter D and wall thickness t of tower to be used with the tripod substructure.

Height w.r.t. MSL [m]	D [m]	t [mm]
10.0	5.700	50.0
13.5	5.700	50.0
18.0	5.700	32.0
22.5	5.687	31.5
27.5	5.673	30.9
32.5	5.658	30.3
37.5	5.644	29.6
42.5	5.629	29.2
47.5	5.615	28.6
52.5	5.601	28.0
57.5	5.586	27.5
62.5	5.572	26.9
67.5	5.558	26.3
72.5	5.543	25.7
77.5	5.529	25.2
82.5	5.514	24.6
87.6	5.500	24.0

Appendix D

Details on jacket structure and models

Table D.1: Jacket substructure nodes and coordinates in the global CS.

Node	x [m]	y [m]	z [m]	Node	x [m]	y [m]	z [m]
9	6	6	-45.5	35	4.82	-4.82	-8.922
10	-6	6	-45.5	36	-4.82	-4.82	-8.922
11	6	-6	-45.5	37	4.592	0	-1.958
12	-6	-6	-45.5	38	-4.592	0	-1.958
13	6	6	-45	39	0	4.592	-1.958
14	6	-6	-45	40	0	-4.592	-1.958
15	-6	6	-45	41	4.385	4.385	4.378
16	-6	-6	-45	42	-4.385	4.385	4.378
17	5.967	5.967	-44.001	43	4.385	-4.385	4.378
18	-5.967	5.967	-44.001	44	-4.385	-4.385	4.378
19	5.967	-5.967	-44.001	45	4.193	0	10.262
20	-5.967	-5.967	-44.001	46	-4.193	0	10.262
21	5.62	0	-33.373	47	0	4.193	10.262
22	-5.62	0	-33.373	48	0	-4.193	10.262
23	0	5.62	-33.373	49	4.016	4.016	15.651
24	0	-5.62	-33.373	50	-4.016	4.016	15.651
25	5.333	5.333	-24.614	51	4.016	-4.016	15.651
26	-5.333	5.333	-24.614	52	-4.016	-4.016	15.651
27	5.333	-5.333	-24.614	54	4	4	16.15
28	-5.333	-5.333	-24.614	55	4	-4	16.15
29	5.064	0	-16.371	56	-4	4	16.15
30	-5.064	0	-16.371	57	-4	-4	16.15
31	0	5.064	-16.371	58	4	4	20.15
32	0	-5.064	-16.371	59	-4	4	20.15
33	4.82	4.82	-8.922	60	4	-4	20.15
34	-4.82	4.82	-8.922	61	-4	-4	20.15

Table D.2: Jacket substructure members connecting the nodes given in Table D.1.

Member	Node 1	Node 2	Member	Node 1	Node 2
13	9	13	63	32	36
14	10	15	64	32	35
15	11	14	65	33	41
16	12	16	66	33	37
17	13	17	67	33	39
18	14	19	68	34	42
19	15	18	69	34	38
20	16	20	70	34	39
21	17	25	71	35	43
22	17	18	72	35	37
23	17	21	73	35	40
24	17	23	74	36	44
25	18	26	75	36	38
26	18	20	76	36	40
27	18	22	77	37	43
28	18	23	78	37	41
29	19	27	79	38	44
30	19	17	80	38	42
31	19	21	81	39	42
32	19	24	82	39	41
33	20	28	83	40	44
34	20	19	84	40	43
35	20	22	85	41	49
36	20	24	86	41	45
37	21	27	87	41	47
38	21	25	88	42	50
39	22	28	89	42	46
40	22	26	90	42	47
41	23	26	91	43	51
42	23	25	92	43	45
43	24	28	93	43	48
44	24	27	94	44	52
45	25	33	95	44	46
46	25	29	96	44	48
47	25	31	97	45	51
48	26	34	98	45	49
49	26	30	99	46	52
50	26	31	100	46	50
51	27	35	101	47	50
52	27	29	102	47	49
53	27	32	103	48	52
54	28	36	104	48	51
55	28	30	105	49	54
56	28	32	106	50	56
57	29	35	107	51	55
58	29	33	108	52	57
59	30	36	109	54	58
60	30	34	110	55	60
61	31	34	111	56	59
62	31	33	112	57	61

Table D.3: Cross sectional properties outer diameter D and wall thickness t of the tower to be used with the jacket substructure.

Height w.r.t. MSL [m]	D [m]	t [mm]	point mass [tons]
20.15	5.600	32	1.9
21.15	5.577	32	No
32.15	5.318	30	No
42.15	5.082	28	No
54.15	4.800	24	1.4
64.15	4.565	22	No
74.15	4.329	20	No
83.15	4.118	30	No
88.15	4.000	30	1.0

Table D.4: Marine growth parameters for the jacket model. Coordinates are given w.r.t. MSL.

Depth range:	$-40\,\text{m} \leq z \leq -2\,\text{m}$
Thickness:	$t_{\text{grow}} = 100\,\text{mm}$
Density:	$\rho_{\text{grow}} = 1100\,\text{kg/m}^3$

Appendix E

Coordinate systems and parts of an offshore wind turbine

The global CS is defined as follows: Its origin lies at MSL in the tower centerline. The global x-axis is pointing in the mean wind direction, the z-axis is pointing vertically upwards and the y-axis forms a right handed CS.

The local (element) CS is defined as follows: The x-axis is aligned with the member axis, the local z-axis is perpendicular to a plane formed by the global x-axis and the local x-axis. If the local- and the global x-axis are parallel, the local z-axis is parallel to the global y-axis. With the local y-axis, a right handed system is formed.

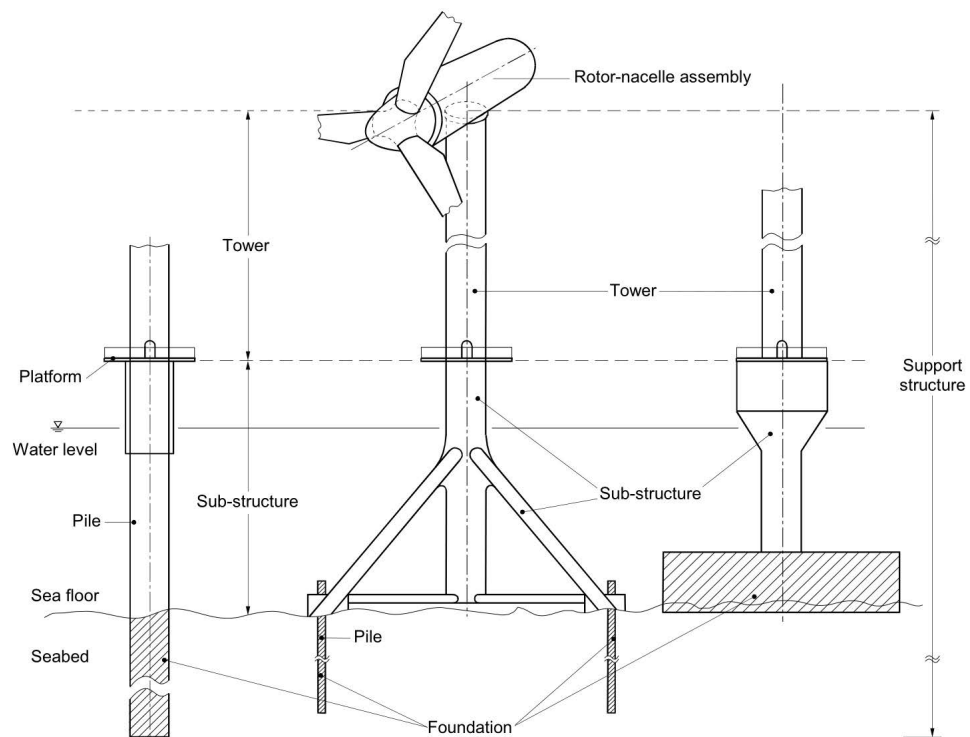IEC definitions as shown in Figure E.1 are used when it is referred to parts of an OWT.

Figure E.1: Parts of an offshore wind turbine according to IEC (Figure 1 of IEC 61400-3 (2009), licenced by VDE Verband der Elektrotechnik Elektronik Informationstechnik e.V. – Department DKE).

Curriculum Vitae

I studied mechanical engineering with specialization Energy at Universität Karlsruhe TH (today Karlsruhe Institute of Technology, KIT) and realized my diploma thesis at Stuttgart University dealing with offshore wind turbines.

In 2006, I joined IWES (formerly Fraunhofer Center for Wind Energy and Maritime Technology) as the first project engineer dealing with wind turbine loads and dynamics and developed and later (2010) led a research group in this field as a group manager. From 2012 to 2014, I headed the department turbine simulation, software development and aerodynamics with 3 groups and 25 research fellows / project managers and I was responsible for staff, budget and strategic development of the department. In light of organizational changes, I decided to refocus my work at IWES on scientific work, namely projects on the dynamics of OWTs with bottom mounted support structures in 2014. Since March 2015, I am working as an independent consultant in parallel.

During my time at IWES, I developed my expertise in global dynamics / structural dynamics / coupled simulation of wind turbines. I put a focus on the offshore wind application dealing with turbines with different types of support structures such as monopiles, tripods and jackets and the respective hydrodynamics simulation. Since 2009, I systematically developed my leadership skills in projects, as a group manager and heading the department.

I worked in, developed & led national and international research and industry projects, authored numerous publications e.g. articles in scientific journals and book chapters. As an internationally recognized expert in my field of expertise I am a reviewer for scientific journals such as Wind Energy and representing IWES in international committees (e.g. the Executive Committee of the International Energy Agency (IEA) Wind Implementing Agreement as Operating Agent for IEA Task 30 or the Scientific Committee of the Journal of Offshore and Wind Energy published by the International Society of Offshore and Polar Engineers).

Publications

Book Chapters

- Strach, M., Stammler, M., Wenske, J., Jonkman, J., Vorpahl, F., Chapter 55: Offshore Wind Energy, In: Handbook of Offshore Engineering, Ed: Prof. Dr. Nikolaos Xiros, Springer-Verlag (to be published).

- Huhn, H., Kupferschmidt, K., Strach, M., Vorpahl, F., Chapter 26: Offshore Wind Structures, In: Handbook of Technical Diagnostics – Fundamentals and application to structures and systems, Ed: Prof. Dr. Dr. Horst Czichos, Springer-Verlag, 2012.

Journal Articles

- Vorpahl, F., Strobel, M., Jonkman, J., Larsen, T., Passon, P. and Nichols, J., Verification of aero-elastic offshore wind turbine design codes under IEA Wind Task XXIII, Wind Energy, 2013, 17(4), 519 – 547.

- Vorpahl, F., Schwarze, H., Fischer, T., Seidel, M. and Jonkman, J., Offshore wind turbine environment, loads, simulation and design, WIREs Energy and Environment, 2013, 2(5), 548 – 570.

- Tu, Y. and Vorpahl, F., Influence of Superelement Support Structure Modeling on the Loads on an Offshore Wind Turbine with a Jacket Support Structure, Journal of Ocean and Wind Energy, 2014, 1(3), 153 – 160.

- Popko W., Antonakas P. and Vorpahl F., Investigation of local vibration phenomena of a jacket sub-structure caused by coupling with other components of an offshore wind turbine, Journal of Ocean and Wind Energy, 2014, 1(2), 111 – 118.

- Popko, W., Vorpahl, F., Zuga, A., Kohlmeier, M., Jonkman, J., Robertson, A., Larsen, T.J., Yde, A., Sætertrø, K., Okstad, K., Nichols, J., Nygaard, T.A., Gao, Z., Manolas, D., Kim, K., Yu, Q., Shi, W., Park, H., Vásquez-Rojas, A., Dubois, J., Kaufer, D., Thomassen, P., de Ruiter, M.J., von der Zee, T., Peeringa, J.M., Zhiwen, H. and von Waaden, H., Offshore Code Comparison Collaboration Continuation (OC4), Phase I – Results of coupled simulations of an offshore wind turbine with jacket support structure, Journal of Ocean and Wind Energy, 2014, 1(1), 1 – 11.

Peer reviewed Conference papers

- Vorpahl, F. and Reuter, A., Fully-coupled wind turbine simulation including substructuring of support structure components: Influence of newly developed modeling approach on fatigue loads for an offshore wind turbine on a tripod support structure, Proceedings of the Twenty-first International Offshore and Polar Engineering Conference, 2011, 284 – 290.

- Vorpahl, F., Strobel, M., Busmann, H. and Kleinhansl, S., Superelement approach in fully coupled offshore wind turbine simulation: Influence of the detailed support structure modelling on simulation results for a 5-MW turbine on a tripod substructure, Proceedings of the Twentieth International Offshore and Polar Engineering Conference, 2010, 711 – 718.

- Vorpahl, F., Wingerde, A., Blunk, M., Busmann, H., Kleinhansl, S., Kossel, T., Kohlmeier, M., Böker, C., Kaufer, D., Azcona, J., Martinez, A. and Munduate, X., Validation of a Finite Element Based Simulation Approach for Offshore Wind Turbines within IEA Wind Annex XXIII – Simulation Challenges and Results for a 5-MW Turbine on a Tripod Substructure, Proceedings of the Nineteenth International Offshore and Polar Engineering Conference, 2009, 362 – 369.

- Robertson A., Wendt, F., Jonkman, J., Popko, W., Vorpahl, F., Stansberg, C., Bachynski, E., Bayati, I., Beyer, F., de Vaal, J., Harries, R., Yamaguchi, A., Shin, H., Kim, B., van der Zee, T., Bozonnet, P., Aguilo, B., Bergua, R., Qvist, J., Qijun, W., Chen, X., Guerinel, M., Tu, Y., Yutong, H. and Li, R., OC5 Project Phase I: Validation of Hydrodynamic Loading on a Fixed Cylinder, Proceedings of the Twenty-fifth International Offshore and Polar Engineering Conference, 2015 (to be published).

- Popko, W., Georgiadou, S., Loukogeorgaki, E. and Vorpahl, F., Verification of different Modeling Techniques of Local Joint Flexibility and their Influence on Local Dynamics of a Jacket Support Structure for Offshore Wind Turbines. In Proceedings of the twenty-fifth International Offshore and Polar Engineering Conference, 2015 (to be published).

- Tu, Y. and Vorpahl, F., Influence of Superelement Support Structure Modeling on the Loads on an Offshore Wind Turbine with a Jacket Support Structure. In Proceedings of the twenty-fourth International Offshore and Polar Engineering Conference, 2014, 342 – 349.

- Robertson, A., Jonkman J., Vorpahl F., Popko W., Qvist J., Frøyd L., Chen, X., Azcona, J., Uzunoglu, E., Guedes Soares, C., Luan, C., Yutong, H. , Pengcheng, F., Yde, A., Larsen, T.A., Nichols, J., Buils, R., Lei, L., Nygaard, T.A., Manolas, D., Heege, A., Vatne, S.R., Ormberg, H., Duarte, T., Godreau, C., Hansen, H.F., Nielsen, A.W., Riber, H., Le Cunff, C., Beyer, F., Yamagushi, A., Jung, K.J., Shin, H., Shi, W., Park, H., Alves, M. and Guérinel, M., Offshore Code Comparison Collaboration Continuation within IEA Wind Task 30: Phase II results regarding a floating semisubmersible wind system, Proceedings of the 33rd International Conference on Ocean, Offshore and Arctic Engineering, 2014.

- Popko, W., Antonakas, P. and Vorpahl, F., Investigation of Local Vibration Phenomena of a Jacket Sub-structure Caused by Coupling with other Components of an Offshore Wind Turbine in a Coupled Simulation Environment, Proceedings of the twenty-third International Offshore and Polar Engineering Conference, 2013, 336 – 344.

- Popko, W., Heinonen, J., Hetmanczyk, S. and Vorpahl, F., State-of-the-art comparison of standards in terms of dominant sea ice loads for offshore wind turbine support structures in the Baltic Sea. Proceedings of the twenty-second International Offshore and Polar Engineering Conference, 2012, 426 – 433.

- Meng, F., Schwarze, H., Vorpahl, F. and Strobel, M., A free wake vortex lattice model for vertical axis wind turbine: Modeling, verification and validation. Proceedings of the Science of making torque from wind, 2012.

- Strach, M. and Vorpahl, F., Modeling offshore wind turbine substructures using a parametric approach. Proceedings of the twenty-second International Offshore and Polar Engineering Conference, 2012, 196 – 201.

- Popko, W., Vorpahl, F., Zuga, A., Kohlmeier, M., Jonkman, J., Robertson, A., Larsen, T., Yde, A., Sætertrø, K., Okstad, K.M., Nichols, J., Nygaard, T.A., Gao, Z., Manolas, D., Kim, K., Yu, Q., Shi, W., Park, H., Vásquez-Rojas, A., Dubois, J., Kaufer, D., Thomassen, P., de Ruiter, M.J., Peeringa, J.M., Zhiwen, H. and von Waaden, H., Offshore code comparison collaboration continuation (OC4), Phase I – Results of coupled simulation of offshore wind turbine with jacket support structure. Proceedings of the twenty-second International Offshore and Polar Engineering Conference, 2012, 337 – 346.

- Brommundt, M., Vorpahl, F., Strach, M., Muskulus, M., Experiences with object-oriented and equation based modeling of a floating support structure for wind turbines in Modelica, Winter Simulation Conference, 2012.

- Strobel, M., Vorpahl, F., Hillmann, C., Gu, X., Zuga, A. and Wihlfahrt, U., The OnWind Modelica Library for Offshore Wind Turbines – Implementation and first results, Modelica Conference, 2011.

- Quesnel, L., Vorpahl, F., Strobel, M. and Busmann, H.-G., Hydrodynamics meet wind turbines: specification and development of a simulation tool for floating wind turbines with Modelica, Proceedings of the Twentieth International Offshore and Polar Engineering Conference, 2010, 704 – 710.

- Nichols, J., Camp, T., Jonkman, J., Butterfield, S., Larsen, T., Hansen, A., Azcona, J., Martinez, A., Munduate, X., Vorpahl, F., Kleinhansl, S., Kohlmeier, M., Kossel, T., Böker, C. and Kaufer, D., Offshore Code Comparison Collaboration within IEA Wind Annex XXIII: Phase III Results Regarding Tripod Support Structure Modeling, 47th AIAA Aerospace Sciences Meeting, 2009.

Other Conference papers

- Vorpahl, F., Blunk, M., Wingerde, A., Busmann, H. and Kleinhansl, S., Implementation of a superelement approach in a design tool for offshore wind turbines with arbitrary support structures, European Offshore Wind Conference, 2009.

- Vorpahl, F., Huhn, H., Busmann, H. and Kleinhansl, S., A Flexible Aero-elastic Simulation Approach for Offshore Wind Turbines, European Offshore Wind Conference, 2007.

- Robertson, A., Jonkman, J., Musial, W., Vorpahl, F., and Popko, W. Offshore Code Comparison Collaboration, Continuation: Phase II Results of a Floating Semisubmersible Wind System, Proceedings of the European Wind Energy Agency Offshore Conference, 2013.

- Schwarze, H., Popko, W., Vorpahl, F., Simulation von Windenergieanlagen als schwingende Systeme. In VDI-Berichte 2200 Schwingungen von Windenergieanlagen 2013, 187 – 199, 2013 (in German).

- Klausmann, P., Vorpahl, F., Kleinhansl, S. and Lieser, O., Influence of shear deformation on the elastic behavior of a tripod support structure in coupled wind turbine simulation. Deutsche Windenergie-Konferenz, 2012.

- Popko, W., Vorpahl, F., Jonkman, J. and Robertson, A., OC3 and OC4 Projects: Verification of simulation tools for offshore wind turbines, Invited paper for the 7th European Seminar on Offshore Wind and other marine renewable Energies in Mediterranean and European Seas, 499 – 503, 2012.

- Kaufer, D., Fischer, T., Vorpahl, F., Popko, W. and Kühn, M., Different approaches to modeling jacket support structures and their impact on overall wind turbine dynamics, Deutsche Windenergie-Konferenz, 2010.

- Moll, H.G., Vorpahl, F., Busmann, H.-G., Dynamics of support structures for offshore wind turbines in fully-coupled simulations – Influence of water added mass on jacket mode shapes, natural frequencies and loads, European Wind Energy Conference, 2010.

Invited Talks (exemplary)

- Vorpahl, F. (Focus Session leader), Popko, W., An Overview of Current Aeroelastic Design Tools: Benefits and Limitations, 4th Annual Future Offshore Foundations Forum, Windpower Monthly, Hamburg, 2014.

- Vorpahl, F., Wind Turbine Simulation and Loads Analysis, IQPC International Conference on Wind Turbine Simulation, Testing and Validation, Bremen, 2014.

- Vorpahl, F., Offshore wind turbine environment, loads and simulation. TEKNA Course in Offshore wind turbine technology and structures, Trondheim, 2012.

- Lasten, Dynamik und Schwingungsaspekte bei der Entwicklung von Offshore-Windenergieanlagen, VDI Wissensforum: VDI-Fachkonferenz Offshore-Windenergieanlagen, Bremerhaven, 2010 (in German).